

**Numerical Modeling of Random 2D and 3D Structural Foams Using Voronoi Diagrams:
A Study of Cell Regularity and Compression Response**

by

Oscar Efraín Sotomayor Gálvez

A thesis submitted to the Graduate Faculty of
Auburn University
in partial fulfillment of the
requirements for the Degree of
Master of Science

Auburn, Alabama
August 03, 2013

Keywords: structural foams, Voronoi diagrams, solid modeling, compression behavior, syntactic
foam, finite element analysis

Copyright 2013 by Oscar Efraín Sotomayor Gálvez

Approved by

Hareesh V. Tippur, Chair, McWane Professor of Mechanical Engineering
Jeffrey C. Suhling, Quina Distinguished Professor of Mechanical Engineering
James S. Davidson, Associate Professor of Civil Engineering

Abstract

Representing the complex morphology of cellular solids in general and metal foams in particular for understanding key factors governing their mechanical behavior is typically achieved using periodic unit cells. Due to the intricacies of foam microstructures, however, such idealizations have many limitations. In this context, the Voronoi tessellation technique in different Euclidean spaces is employed in the present thesis to better represent structural foams. A procedure to generate dry and wet Voronoi structures through stochastic generation of nuclei in a control space based on Poisson probability distribution in 2D and 3D is attempted. Moreover, a process of controlling the degree of irregularity of Voronoi 2D and 3D foams through the application of a Simple Sequential Inhibition (SSI) process is demonstrated. A suitable and intuitively simple index for quantifying the regularity (δ) of a specific foam structure both in 2D and 3D has been identified. Further, the extremely low probability of generating highly regular foam configurations based on pseudo-random generation of nuclei has led to the development of a perturbation process to complement the SSI process. The possibility of creating real Voronoi foams using Additive Manufacturing methods has also been demonstrated.

A finite element modeling procedure incorporating solid modeling methods is developed to analyze the influence of the cell regularity and density on the compression response of Voronoi honeycombs (2D) of low relative densities ($\bar{\rho}$) in the range of 3% to 9%. An isotropic response is seen in all the configurations with only a limited directional dependency in case of regular honeycombs of higher densities. An inverse relationship between regularity and elastic modulus is also identified. A fully irregular ($\delta = 0$) configuration is ~66% stiffer than a completely regular

counterpart ($\delta = 1$). In contrast, the plastic-collapse strength of a regular foam is {28%, 31%, 35% and 50%} higher than a fully irregular Voronoi honeycomb of relative density $\bar{\rho} = \{9\%, 7\%, 5\%, 3\%\}$. Simulations also show that elastic modulus and plastic-collapse strength of Voronoi honeycombs scale with $\bar{\rho}^3$ and $\bar{\rho}^2$, respectively.

The influence of regularity has also been studied in the context of syntactic foam-filled Voronoi honeycombs as a 2D representation of an Interpenetrating Phase Composite (IPC). Voronoi wet honeycombs with $\delta = \{0, 0.5, 0.7, 0.8 \text{ and } 1\}$ and $\bar{\rho} = 9\%$ are used for simulations. Irregular configurations show an isotropic response with an inverse monotonic relation between mechanical properties and cell regularity in the elastic and plastic regimes. In the elastic range, the stress-strain response is bounded by those of regular geometries compressed in two orthogonal directions.

The analysis presented for Voronoi honeycombs is also extended to the 3D space to simulate open cell Voronoi foams. The elastic modulus of foams with different regularities and relative densities in the range of 3% to 9% are compared with the analytical and empirical models available in the literature. Direct relationships between elastic modulus, plastic-collapse strength and plateau strength with the degree of regularity are observed. A regular foam based on a 3D array of regular tetrakaidecahedron cells is {41.3%, 43.7%, 46.5% and 49.5%} stiffer than a fully irregular Voronoi foam for $\bar{\rho} = \{9\%, 7\%, 5\%, 3\%\}$, respectively. Simulations show that elastic modulus of Voronoi foams can be described in terms of relative density ($\bar{\rho}$) using a second order polynomial whereas the plastic-collapse strength scales with $\bar{\rho}^{1.5}$. It is shown that the deleterious effect of sudden collapse of regular 3D foams at yield can be mitigated by introducing a small perturbation to the regularity, say, $\delta = 0.95$.

Acknowledgments

I am filled with a great sense of gratitude towards my advisor Dr. Hareesh Tippur. It has been a privilege to work under his expert technical guidance and support. God could not have placed a better mentor in my path. I gratefully thank Dr. Jeffrey Suhling and Dr. James Davidson for sharing their knowledge at Auburn University, their predisposition to be on my committee, and for reviewing this thesis. I also wish to express my gratitude to Dr. Chandru Periasamy for sharing his experimental results, his expert guidance, and friendly collaboration in the crucial initial stages of this work. I greatly appreciate the Fulbright Foundation from the US and SENESCYT from Ecuador for financial support through grant IIE-ID-No:15111245. I thank ASME for providing partial financial support for this work through the 2011/2012 Rice-Cullimore Scholarship. I want to extend my admiration and recognition of the Laboratory for Failure Mechanics and Optical Techniques team, Kailash, Robert, Vinod, Balamurugan, and Amith for their friendship and collaboration.

Finally, I wish to express my deepest gratitude to my parents and sister for their moral support and backing during these years. I dedicate this work to my wife for her forbearance and understanding.

Table of Contents

Abstract	ii
Acknowledgments	iv
List of Tables	viii
List of Figures	ix
1. INTRODUCTION.....	1
1.1. Motivation.....	1
1.2. Syntactic foam – Aluminum foam Interpenetrating Phase Composite (IPC)	3
1.3. Literature review	10
1.4. Objectives.....	14
1.5. Organization of the thesis.....	15
2. VORONOI DIAGRAMS	17
2.1. Mathematical concepts	20
2.2. Voronoi diagram - Definition.....	28
3. MODELING FOAM GEOMETRY.....	32
3.1. Geometric construction of 2D Voronoi honeycombs	38
3.2. Geometric construction of 2D foam-filled Voronoi honeycombs	45
3.3. Geometric construction of 3D open cell foams.....	47

3.4. Geometric construction of 3D wet foams	54
4. FINITE ELEMENT MODELING OF VORONOI HONEYCOMBS.....	60
4.1. Finite element modeling of Voronoi honeycombs.....	61
4.2. The effect of loading direction.....	71
4.3. Role of regularity	81
4.4. The effect of relative density.....	86
5. FINITE ELEMENT MODELING OF FOAM-FILLED V. HONEYCOMBS.....	90
5.1. Finite Element Modeling of Voronoi Aluminum-Syntactic foam composites.	91
5.2. The effect of loading direction.....	101
5.3. Dependency on regularity	105
6. FINITE ELEMENT MODELING OF 3D VORONOI FOAMS.....	109
6.1. Finite element modeling.....	111
6.2. Results.....	117
6.3. The effect of relative density.....	125
6.4. Role of regularity	130
6.5. Highly regular foams.....	132
7. CONCLUSIONS AND FUTURE WORK	136
7.1. Conclusions.....	136
7.2. Future work.....	139

REFERENCES.....	141
APPENDIX A	144
APPENDIX B	148
APPENDIX C	153

List of Tables

Table 3.1:	Inhibition distance required to place $n = 314$ nucleus points in a unit square area with a SSI process (A , n , and s are the inputs for the SSI algorithm).	39
Table 4.1:	Thickness of struts for different configurations of Voronoi honeycombs	64
Table 4.2:	Elastic modulus data fitting for Voronoi honeycombs with different regularities....	87
Table 4.3:	Plastic-collapse strength data fitting for Voronoi honeycombs with different regularities.....	88
Table 5.1:	Properties of the constituents of syntactic foam constituents.....	92
Table 6.1:	Struts properties for different configurations of Voronoi honeycombs	115
Table 6.2:	Elastic modulus data fitting for Voronoi foams with different regularities	127
Table 6.3:	Plastic-collapse strength data fitting for 3D Voronoi foams with different regularities.....	129
Table 6.4:	Struts properties for different configurations of Voronoi honeycombs	133

List of Figures

Figure 1.1:	Cellular solids structures in nature: (a) balsa wood, (b) trabecular bone (from [2])	2
Figure 1.2:	Two polyhedra representations: (a) closed cell configuration, (b) open cell configuration.....	4
Figure 1.3:	Micrograph of epoxy syntactic foam with 30% volume fraction of hollow glass microballoons (from [8]).	8
Figure 1.4:	Traditional composite	9
Figure 1.5:	Interpenetrating phase composite (IPC): (a) first phase network, (b) second phase network, (c) IPC.....	9
Figure 1.6:	Micrograph of the IPC foam showing the constituents (from [8]).	10
Figure 2.1:	Examples of natural division of space: (a) giraffe skin pattern (arkive.org), (b) a dry lake bed (wunderground.com), (c) osseous tissue (sciencephoto.com).....	17
Figure 2.2:	Metal foam structures: (a) nickel foam, open cell structure (sciencephoto.com), (b) aluminum foam, closed cell structure (http://www.rug.nl/natuurkunde/onderzoek/groepen/mimec/research/metallicfoams?lang=en).	18
Figure 2.3:	(a) Tetrakaidecahedron cell based foam representation, (b) Isolated tetrakaidecahedron cell	19
Figure 2.4:	(a) convex set, (b) no convex set in $m = 2$ (drawn based on concepts in reference [34]).	20
Figure 2.5:	(a) no convex set A, (b) boundary of the convex hull of A, (c) convex hull of A (in $m = 2$, concept from [34] redrawn).	21

Figure 2.6:	(a) no convex set A, (b) convex hull of A ($m = 3$).....	22
Figure 2.7:	Types of planar point patters: (a) complete spatial randomness (CSR), (b) clustered, (c) regular ([34, 36]).	23
Figure 2.8:	Planar point patters for $n = 100$ in a unit square with inhibition distance (a) $s = 0$, (b) $s = 0.05$, (c) $s = 0.1$	25
Figure 2.9:	Three dimensional point pattern in a unit cube for $n = 125$ with regularity parameter: (a) $\delta = 1$, (b) $\delta = 0$	28
Figure 2.10:	Voronoi diagrams in different dimensions: (a) $m = 1$, (b) $m = 2$, (c) $m = 3$	29
Figure 2.11:	(a) Voronoi diagram (dashed lines) and Delaunay tessellation (solid lines), (b) no nucleus point is present inside the circumscribing circle	31
Figure 3.1:	A single open cell of a foam: (a) dry configuration, (b) wet configuration.....	34
Figure 3.2:	Flowchart for constructing Voronoi honeycombs and foams. (SSI: Simple Sequential Inhibition process)	37
Figure 3.3:	Nuclei points produced using SSI process (except $\delta = 1$) with different regularity: (a) $\delta = 0$, (b) $\delta = 0.5$, (c) $\delta = 0.7$, (d) $\delta = 0.8$, (e) $\delta = 1$	40
Figure 3.4:	Partitioning of space and construction of a cell. (a) Output of the Voronoi partition process algorithm (solid squares), (b) Convex hull for the solid squares	42
Figure 3.5:	Voronoi honeycombs for: (a) $\delta = 0$, (b) $\delta = 0.5$, (c) $\delta = 0.7$, (d) $\delta = 0.8$, (e) $\delta = 1$	43
Figure 3.6:	Probability $p(F)$ of finding cells with F faces with different levels of regularity.....	45
Figure 3.7:	Effect of varying relative density in 2D foams for $\delta = 0.8$. (a) $\bar{\rho} = 45\%$, (b) $\bar{\rho} = 25\%$, (c) $\bar{\rho} = 9\%$, (d) $\bar{\rho} = 3\%$	47
Figure 3.8:	Nuclei points to generate one tetrakaidecahedron cell in a unit cube.....	49
Figure 3.9:	Point patterns for, $n = 559$ and (a) $\delta = 1$, (b) $\delta = 0.95$, (c) $\delta = 0.8$	50

Figure 3.10:	A single Voronoi cell construction in 3D: (a) output of the Voronoi partitioning algorithm (square symbols), (b) Convex hull constructed for square symbols	52
Figure 3.11:	3D dry open cell foams: (a) $\delta = 1$, (b) $\delta = 0.95$, (c) $\delta = 0.8$	53
Figure 3.12:	Thickening process for generation of 3D wet foams: (a) dry foam presented in Fig. 3.11(b) over which a “thickening” is performed at one corner region, (b) detail.....	55
Figure 3.13:	Additive manufacturing: (a) CAD model of a foam with 97 cells, $\bar{\rho} = 9\%$ and $\delta = 0.95$ (b) physical model after a Fused Deposition Modeling process with ABS.....	57
Figure 3.14:	Voronoi honeycomb with $\bar{\rho} = 9\%$ and $\delta = 0.95$ produced with a Polyjet Technology in VeroWhitePlus® material.....	60
Figure 3.15:	Rendering of a foam of $\bar{\rho} = 9\%$ and $\delta = 0.95$ with a spherical macroscopic shape.....	59
Figure 4.1:	Voronoi honeycombs with: (a) $\delta = 0$, (b) $\delta = 0.5$, (c) $\delta = 0.7$, (d) $\delta = 0.8$, (e) $\delta = 1$...	62
Figure 4.2:	Material model for Al 6101 – T6.....	63
Figure 4.3:	Boundary conditions for the Voronoi honeycombs simulations (example shown $\delta = 0.8$ loaded in the x_2 direction).	66
Figure 4.4:	Stress-strain curves for Al Voronoi honeycomb with a $\bar{\rho} = 9\%$, $\delta = 1$ loaded in the x_2 direction	70
Figure 4.5:	Stress-Strain curves for a 9% Al Voronoi honeycomb of 40 ppi and $\delta = 0$	73
Figure 4.6:	Stress-Strain curves for a 9% Al Voronoi honeycomb of 40 ppi and $\delta = 0.5$	74
Figure 4.7:	Stress-Strain curves for a 9% Al Voronoi honeycomb of 40 ppi and $\delta = 0.7$	75
Figure 4.8:	Stress-Strain curves for a 9% Al Voronoi honeycomb of 40 ppi and $\delta = 0.8$	76
Figure 4.9:	Stress-Strain curves for a 9% Al Voronoi honeycomb of 40 ppi and $\delta = 1$	77

Figure 4.10:	Al Voronoi honeycomb response with $\bar{\rho} = 9\%$ for $\delta = 0.8$ compressed in the x_2 . The two broken lines correspond to two separate sets of nuclei.....	80
Figure 4.11:	Al Voronoi honeycomb response with $\bar{\rho} = 9\%$ for different regularities compressed in the x_2 direction	82
Figure 4.12:	Stress-strain curves for Al Voronoi honeycombs with a $\bar{\rho} = 9\%$ for different levels of randomness compressed in the x_2 direction	83
Figure 4.13:	Effect of regularity on elastic modulus of Voronoi honeycombs of different relative densities	84
Figure 4.14:	Effect of regularity on plastic-collapse strength of Voronoi honeycombs for different relative densities	85
Figure 4.15:	Influence of regularity parameter on plateau strength of Voronoi honeycombs of different relative densities.....	86
Figure 4.16:	Variation of elastic modulus of Voronoi honeycombs with relative density for different regularities.....	87
Figure 4.17:	Plastic-collapse strength vs. relative density for different regularities	88
Figure 4.18:	plateau strength vs. relative density for different regularities.....	89
Figure 5.1:	Experimental obtained compression response of syntactic foam with 40% volume fraction of hollow microballons in epoxy matrix	93
Figure 5.2:	Partitions on a two-phase composite and the corresponding sets created (example shown $\delta = 0.8$, compression in the x_2 direction)	94
Figure 5.3:	Boundary conditions for the two phase composite simulation (example shown $\delta = 0.8$ loaded in x_2 direction).	95
Figure 5.4:	Typical mesh configuration for a two phase composite ($\delta = 0.5$ loaded in the x_2 direction).....	96
Figure 5.5:	Von Mises stress for applied strains of: (a) 0.5%, (b) 0.7%, (c) 5.03%, (d) 7.06%, (e) 12.02% and (f) 16.06% for $\delta = 0.5$	99

Figure 5.6:	Strain contours at: (a) 0.5%, (b) 0.7%, (c) 5.03%, (d) 7.06%, (e) 12.02% and (f) 16.06% strain for $\delta = 0.5$. (units of stress in the color bar Pa)	100
Figure 5.7:	Stress-Strain curves of foam-filled Voronoi honeycombs (AL-9% and SF-40), $\delta = 1$	102
Figure 5.8:	Stress-Strain curves of foam-filled Voronoi honeycombs (AL-9% and SF-40), $\delta = 0.8$	103
Figure 5.9:	Stress-Strain curves of foam-filled Voronoi honeycombs (AL-9% and SF-40), $\delta = 0.7$	103
Figure 5.10:	Stress-Strain curves of foam-filled Voronoi honeycombs (AL-9% and SF-40), $\delta = 0.5$	104
Figure 5.11:	Stress-Strain curves of foam-filled Voronoi honeycombs (AL-9% and SF-40), $\delta = 0$	104
Figure 5.12:	Stress-Strain curves of foam-filled Voronoi honeycombs (AL-9% and SF-40) for different regularities in the strain range of 0 to 0.02	105
Figure 5.13:	Stress-Strain curves of foam-filled Voronoi honeycombs (AL-9% and SF-40) for different regularities.....	106
Figure 5.14:	Effect of regularity on elastic modulus of foam-filled Voronoi honeycombs generated using SSI process	107
Figure 5.15:	Effect of regularity on plastic-collapse strength of foam-filled Voronoi honeycombs generated using SSI process	108
Figure 5.16:	Influence of regularity on plateau strength of foam-filled Voronoi honeycombs generated using SSI process	108
Figure 6.1:	Geometry of 3D Voronoi foams for: (a) $\delta = 0$, (b) $\delta = 0.5$, (c) $\delta = 0.7$, (d) $\delta = 0.8$, (e) $\delta = 1$	113
Figure 6.2:	3D Al Voronoi foam response with $\bar{\rho} = 9\%$ for different regularities.....	118

Figure 6.3:	3D Al Voronoi foam response with a $\bar{\rho} = 9\%$ for different regularities	118
Figure 6.4:	3D Al Voronoi foams response with $\bar{\rho} = 7\%$ for different regularities	119
Figure 6.5:	3D Al Voronoi foams response with $\bar{\rho} = 7\%$ for different regularities	119
Figure 6.6:	3D Al Voronoi foams response with $\bar{\rho} = 5\%$ for different regularities	120
Figure 6.7:	3D Al Voronoi foams response with $\bar{\rho} = 5\%$ for different regularities	120
Figure 6.8:	3D Al Voronoi foams response with $\bar{\rho} = 3\%$ for different regularities	121
Figure 6.9:	3D Al Voronoi foams response with $\bar{\rho} = 3\%$ for different regularities	121
Figure 6.10:	Von Mises stress contour of AL Voronoi foam with $\delta = 0.7$ and $\bar{\rho} = 3\%$ for applied strains of: (a) 1.35%, (b) 2.05%, (c) 8.01%, (d) 15.75%. (units of stress in the color bar are in Pa).....	124
Figure 6.11:	Variation of elastic modulus of 3D Voronoi foams with relative density for different regularities	126
Figure 6.12:	Plastic-collapse strength vs. relative density for different regularities.....	128
Figure 6.13:	The plateau strength variation with relative density for different regularities.....	129
Figure 6.14:	Effect of regularity on elastic modulus of 3D Voronoi foams of different relative densities	130
Figure 6.15:	Effect of regularity on plastic-collapse strength of 3D Voronoi foams for different relative densities	131
Figure 6.16:	Influence of regularity parameter on plateau strength of 3D Voronoi foams of different relative densities.....	132
Figure 6.17:	3D Al Voronoi foams with a $\bar{\rho} = 9\%$ for different regularities.....	134

Figure 6.18: 3D Al Voronoi foams with a $\bar{\rho} = 7\%$ for different regularities..... 134

Figure 6.19: 3D Al Voronoi foams with a $\bar{\rho} = 5\%$ for different regularities..... 135

Figure 6.20: 3D Al Voronoi foams with a $\bar{\rho} = 3\%$ for different regularities..... 135

CHAPTER 1

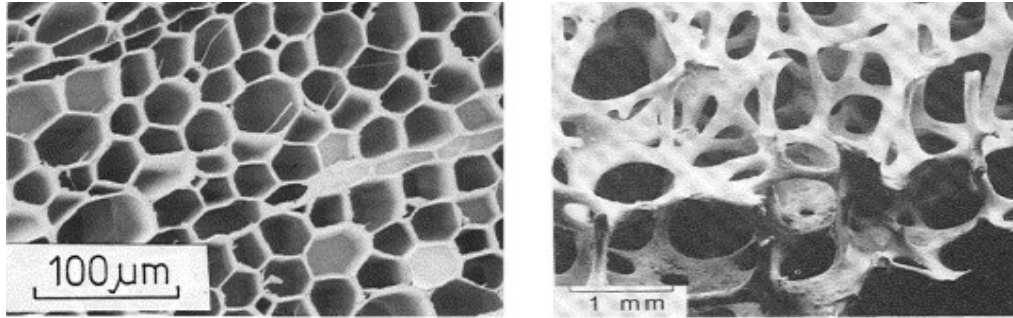
INTRODUCTION

1.1. Motivation

The impact of humans on earth after 300,000 years of existence is evident all around us. Bridges cross rivers and underwater tunnels connect islands inaccessible just a hundred years ago. In order to accomplish these magnificent engineering feats, machines that transform natural resources into energy have been invented. It has caused an insatiable appetite for energy. Pollution, lack of raw materials, global warming and raising oil prices are just a few unexpected side effects. Certainly, the energy crisis has forced efficient utilization of natural resources. Engineers and scientists play an important role in finding effective use for materials, natural resources and energy. Indeed, their designs can have a major impact on preventing detrimental effects imposed over the planet. Author's desire to contribute to this objective has motivated the current research.

First, after millions of years of experimentation nature has succeeded in using minimum resources for maximum performance. For that reason, it is not unusual that nature is a strong motivator for engineers to achieve efficient structural designs. For instance, honeycomb designs are utilized by biological creatures as an efficient natural structure that maximizes space for larvae while minimizing construction material [1]. Consequently, designers are mimicking honeycomb designs to create lightweight and high strength parts for the aerospace industry. The particular shape of honeycombs is based on a repetition of a standard hexagonal unit cell. Indeed, most biological creatures build by replicating a cell based structure. However, the standard regular unit cell repetition is not common in nature; most of the time the cell arrangement in cellular solids is irregular. For example, Fig. 1.1

shows a section of balsa wood (a) and trabecular bone (b) where it is clear that irregularity of cells is intrinsic. As a consequence, engineers and scientists have to model such complex structures in order to understand its properties and apply its concepts in future designs.



(a)

(b)

Figure 1.1: Cellular solids structures in nature: (a) balsa wood, (b) trabecular bone (from [2]).

Second, nature is not only a source of inspiration for efficient designs but also for efficient manufacturing processes. By mimicking natural ways of production, humans can improve current trends in manufacturing and construction. In order to construct a specific structure, nature and humans usually take different approaches. While most of the human construction methods are based on removing material from a bulk to obtain the final product, most, if not all, natural ways of construction are mainly based on an additive process (see [1]). For instance, bones, trees, plant stems, corals, shells are just a few examples of natural structures that were created by adding material. On the other hand, cutting, sanding, drilling, sculpting, extrusion, stamping, drawing, forming, rolling, grinding, turning are processes commonly employed by humans where the removal of material is the main strategy to sculpt the final product. Nevertheless, creating products or parts by adding material layer-by-layer into a growth process is recently being explored. In fact, advances in the field of Additive Manufacturing have dramatically opened the possibilities of creation of products to the human imagination.

Scientific computing plays a major role in understanding the way nature designs and constructs its structures. Computer simulations can explore complex natural phenomena inaccessible for researchers just a few years ago. Meanwhile, accessibility to high performance computing and advanced computer modeling languages for researchers has increased tremendously. Along with the theory and experimentation, scientific computer modeling has become an important tool for scientific discoveries [3]. At the present, computer modeling has helped to understand phenomena that can be expensive or impossible to study experimentally [4]. Examples of such applications are not uncommon. In advanced materials engineering, researchers need to perform a considerable number of experiments to validate their theories. Often, specimens need to be destructively tested to measure their mechanical properties, and hence cannot be reused. However, high performance materials can be expensive and difficult to produce. Alternatively, simulation on a virtual model, representative of the experiment, can be performed repeatedly without this disadvantage of requiring a new specimen for each test. As a result, new demands have risen for researchers in scientific computing field. How to correlate models with experiments and how to deal with errors during simulation are questions one must face. The present study intends to take advantage of the current computational capacity and explore the complexity of natural structures through computer modeling and simulations.

1.2. Syntactic foam – Aluminum foam Interpenetrating Phase Composite (IPC)

a) Cellular Solids

According to Gibson [2], a cellular solid is formed by a network of faces and ligaments which are interconnected to one another forming units or cells. A few natural structures are shown in Fig. 1.1(a) (balsa wood) and Fig. 1.1(b) (trabecular bone). When structures do not present a significant variation in the axial direction (perpendicular to the

sheet in Fig 1.1(a), they can be analyzed in a two dimensional (2D) space and are frequently referred to as honeycombs. Consequently, cells can be idealized as a regular or irregular arrangement of polygons as in the case of a honey bee built structure and balsa wood (Fig. 1.1(a)) sections, respectively. On the other hand, when cells are represented by polyhedra and are packed to fill a three dimensional space (Fig. 1.1(b)), they are normally referred to as foams. When a polyhedron encloses a space and isolates it from the neighboring regions, it is called a closed cell or closed polyhedron (see Fig. 1.2(a)). In contrast, when regions surrounding the polyhedron are not isolated from the region inside the cell, it is designated as an open cell (see Fig. 1.2(b)). For that reason, foams can have two basic configurations, namely open or close cell foams although the nomenclature as reticulated or non-reticulated foams can also be applied, respectively. However, a combination of the two configurations is not uncommon.

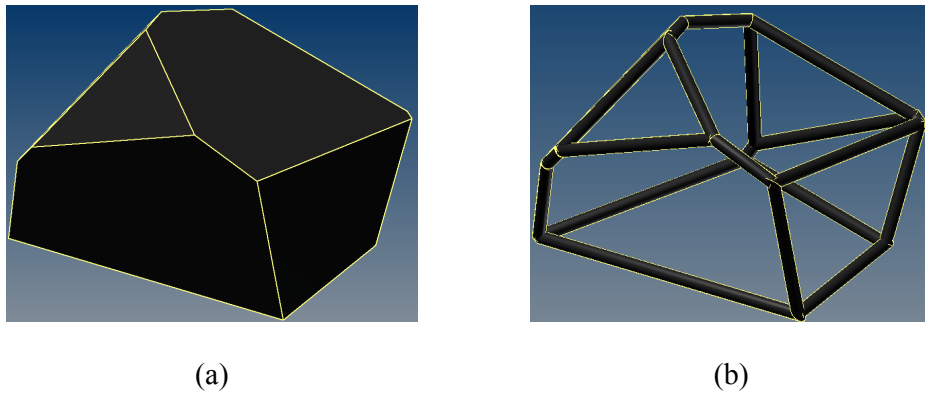


Figure 1.2: Two polyhedra representations: (a) closed cell configuration, (b) open cell configuration.

The most important attribute of a cellular solid is its relative density defined by,

$$\bar{\rho} = \frac{\rho^*}{\rho_s}$$

where $\bar{\rho}$ is the relative density of the foam, ρ^* is the density of the cellular material and ρ_s is the density of the solid with which the cells are made of. The cellular solids have low relative

densities, typically less than 30%. Their particular microstructure combined with a low relative density gives cellular solids properties not easily found in fully compact solids. As a result, cellular solids have been widely utilized by the industry due to their desirable mechanical, thermal and acoustic characteristics. First, their lightweight combined with stiffness makes cellular solids an exceptional option for structural applications. For instance, the most widely used structural material is a natural cellular solid, wood [2, 5]. Wood is a cellular material formed by large cells and fibers generally aligned in one direction. In fact, the fiber alignment gives wood a directional dependence that must be taken into account during design. Moreover, the extraordinary capacity of cellular solids to absorb energy during crushing has made them competitive in the packaging industry as shock and impact absorbers. The low density also translates into low shipping and transportation cost [2]. Second, low thermal conductivity of cellular solids, specifically in case of polymer and glass foams, make them outstanding alternatives for insulation materials. For instance, melamine resin foam is used to insulate steel tanks carrying liquefied natural gas (LNG) where critical temperatures as low as -160°C are required. At such low temperatures, the resin foam needs to be stable enough to maintain its mechanical properties, yet not to behave in a brittle manner. Finally, cellular solids possess an extraordinary capacity to absorb noise and filter out sound. Noise absorption applications include, aircraft passenger ventilation ducts, data processing equipment, anechoic chambers, among others.

Among the wide range of cellular solids available for structural applications, the focus of this thesis is on modeling open cell aluminum foams, syntactic foams and their combination into an interpenetrating or co-continuous foam.

b) Open cell aluminum foams

Metallic foams are cellular solids that compete with polymeric foams due to improvements in their production process [6]. Although almost all metals can be foamed, elaborate techniques are used to produce metal foams of aluminum, nickel, tantalum, gold, silver and titanium. Indeed, the low melting point and corrosion resistance have made aluminum most suitable for the currently available techniques. Common procedures to produce aluminum foam are detailed by Ashby [6]. For example, procedures such as particle decomposition in liquid, vapor phase deposition and solidification in an open cell mold are normally used to produce aluminum foams. The last two methods produce open cell microstructures while decomposition in liquid ordinarily produces closed cell aluminum foam configurations. In fact, the technique that produces the lowest relative density is the vapor phase deposition procedure [6]. Here an open cell polyurethane foam precursor is used to deposit aluminum particles on the polyurethane cell ligaments that are eventually replaced by aluminum. However, the cost of production still needs to be reduced to completely expand its applications from aerospace to regular industries. In spite of the fact that the cost is still the primary disadvantage of open cell aluminum foams, its exceptional mechanical and physical characteristics have made aluminum foam rather competitive. Thus, marine, automotive, aerospace and military industries take advantage of high stiffness to weight ratio, energy absorption, low density, vibration damping capacity and high rigidity characteristics of aluminum foams. In addition, sandwich structures increase their flexural rigidity by using aluminum foam as the core material. More importantly, bonding between foam core and face sheets in sandwich structures is superior compared to honeycomb cores. Furthermore, aluminum foam is resistant to fire, 100% recyclable, acoustically insulating and does not produce toxic gases when burnt, making them appropriated for personnel cabins inside petroleum refining facilities.

c) Syntactic foams

According to Shutov [7], syntactic polymer foams are a relatively new kind of materials formed by mechanically combining a polymer matrix and hollow spherical filler into a ternary system as shown in Fig. 1.3. The ternary system is a direct consequence of the different materials that form hollow spherical filler and matrix along with the empty (or gas filled) space within the hollow spheres. Normally, the polymer matrix could be an epoxy, polyester, phenolic resin or polyurethane while hollow spherical fillers are made of glass, carbon, metals, or polymers. Micro or macrospheres can be employed as hollow spherical fillers. While microspheres are in the range of 1 to 500 μm , macrospheres can exceed 1 mm in diameter [7]. As a consequence, mechanical characteristics of syntactic foams depend on the matrix material, size and proportion of hollow spherical filler along with the level of homogenization of the mixture. In fact, high uniformity of hollow fillers is usually achieved by mechanically blending the hollow spheres in an uncured matrix although high viscosity of some polymers at room temperature usually makes this process difficult. Thus, characteristics such as good specific mechanical properties, low density and buoyancy make syntactic foams suitable for aerospace and deep sea structures. The present work deals with modeling of a syntactic polymer foam made from an epoxy matrix with 40% of hollow glass microballons (SF-40) with a wall thickness of $\sim 0.6 \mu\text{m}$ and an average diameter of 60 μm . The property of this closed cell ternary system is homogenized for modeling and analysis purposes.

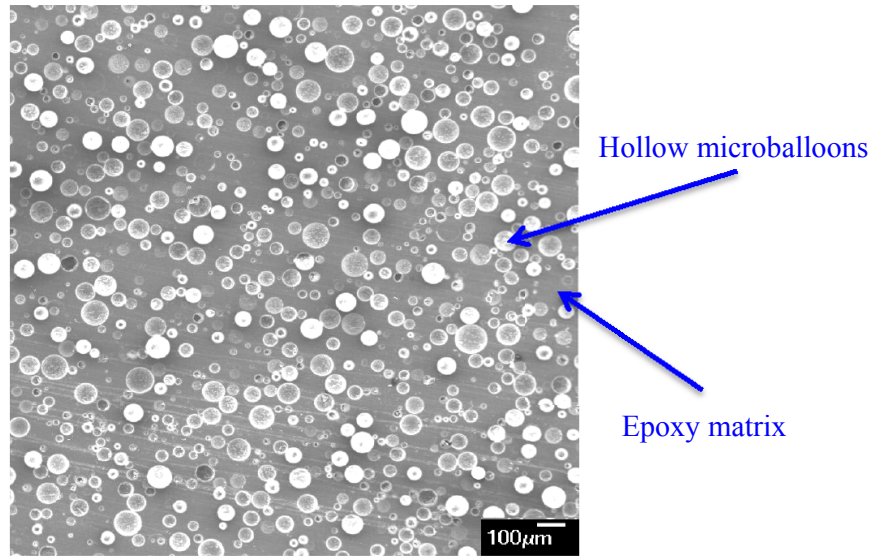


Figure 1.3: Micrograph of epoxy syntactic foam with 30% volume fraction of hollow glass microballoons (from [8]).

d) IPC foams

The multiphase interconnected morphology of bone tissue and other natural structures have inspired the development of more advanced composite materials. These include the ones in which the matrix phase cannot be distinguished from the reinforcement phase as in conventional composites. In conventional composites, a discrete reinforcement phase is embedded in a matrix phase (see [9]). As a consequence, the elements of the reinforcement phase are isolated from one another, as shown schematically in Fig. 1.4, and only the matrix phase can be considered three dimensionally connected. In contrast, interpenetrating phase composites (IPC) are multiphase composites in which all individual phases are intermingled and co-continuous in a 3D space. In practice, the feasibility of producing IPC with two phases has been proposed by many researchers ([9-11]). However, interpenetrating phase composites do not have a limit in the number of phases interconnected from a theoretical point of view.

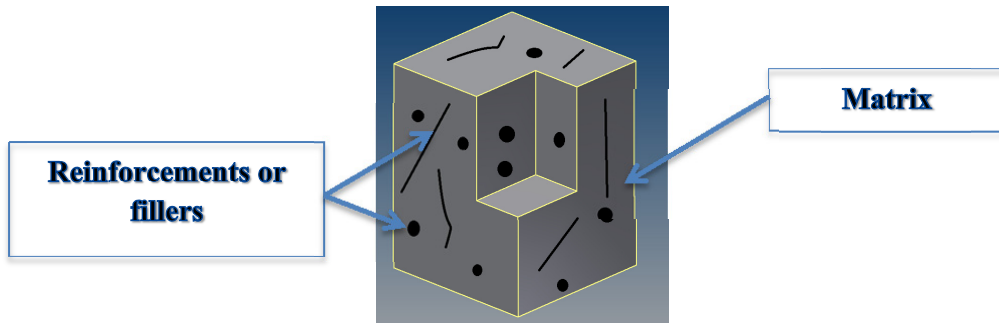


Figure 1.4: Traditional composite

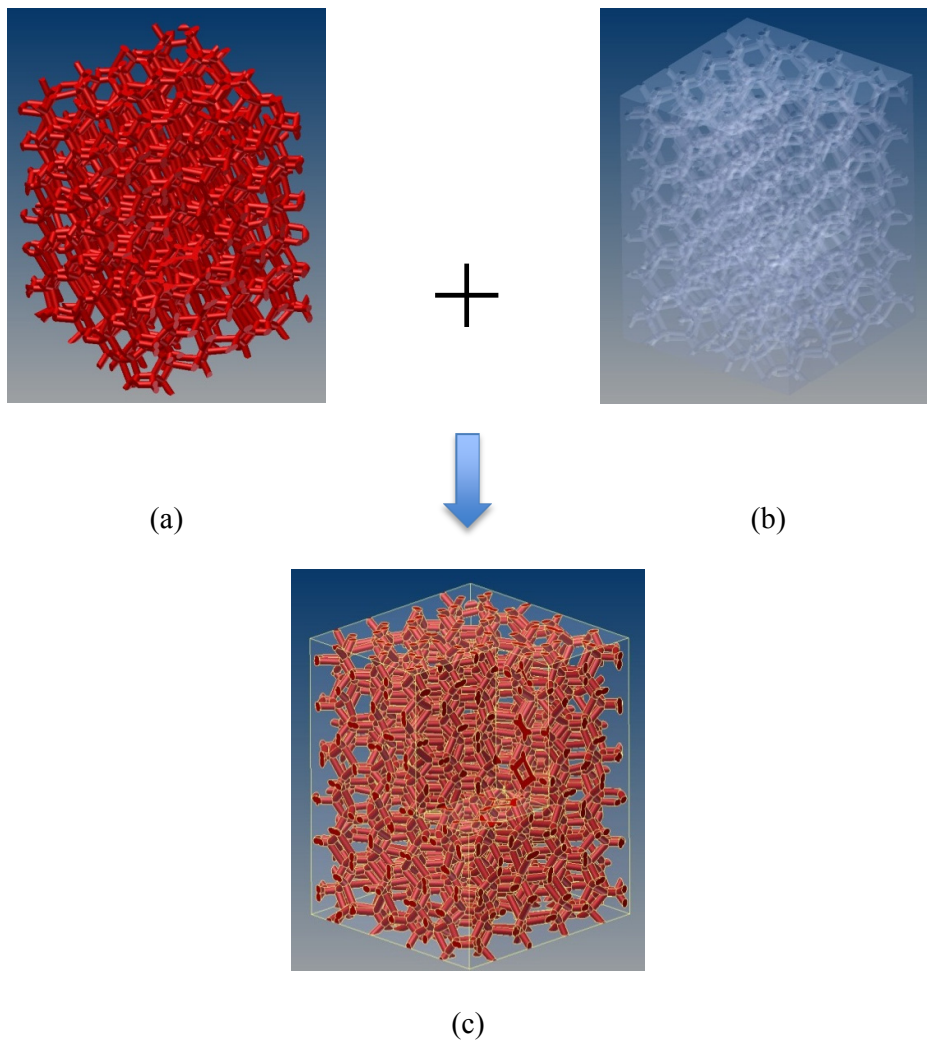


Figure 1.5: Interpenetrating phase composite (IPC): (a) first phase network, (b) second phase network, (c) IPC.

Thus, with advances in the field of Additive Manufacturing, it is not difficult to foresee 3D printed IPC with multiple phases in the near future. For the sake of simplicity, a two-phase idealization of an IPC is presented in Fig. 1.5(c). The first and second phase networks are displayed separately in Fig. 1.5(a) and (b). For better visualization, the second phase has been turned into a transparent material to fully appreciate the interior channels to be filled by the first phase without leaving empty spaces. Hence, the configuration of IPC contributes to superior mechanical results than simple mixing of the two phases.

The present thesis deals with modeling of Interpenetrating Phase Composites made with syntactic foam containing 40% of volume fraction of microballoons (SF-40) infused into an open-cell aluminum foam (relative density 9%) demonstrated by Jhaver and Tippur [10]. Fig. 1.6 shows a micrograph of the cross sectional configuration of an IPC foam with SF-30.

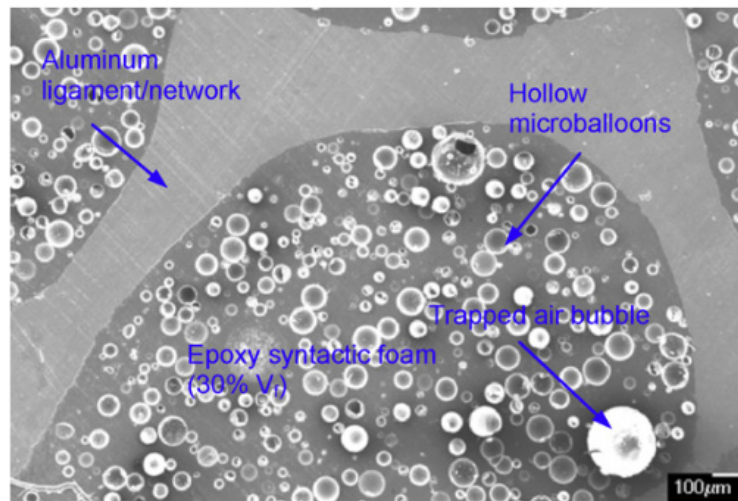


Figure 1.6: Micrograph of the IPC foam showing the constituents (from [8]).

1.3. Literature review

In order to understand the behavior of three dimensional foams, an in-plane analysis of honeycombs is quite useful. In 1997 Papka and Kyriakides [12] conducted an experimental

and numerical analysis of the in-plane compression response of regular honeycombs. The mechanisms governing quasi static compression behavior of aluminum honeycomb were identified and correlated with experimental observations. The application of the FE method showed excellent agreement with measurements and has been successfully applied subsequently by other authors for modeling honeycombs and foams (see [13-16]). The limitation of regular periodic honeycombs to accurately represent the random morphology of natural foams has led to the development of the so-called Voronoi approach. Silva and Gibson [14] generated non-periodic Voronoi honeycombs in order to capture the random morphology of real foams. The authors generated different Voronoi honeycombs and compared the elastic properties with those of regular honeycombs. They concluded that the effective strength (plateau strength) of Voronoi honeycombs is on average 30% to 35% lower than those of their regular counterparts. In a previous research [15], the same authors showed that variation in the arrangement of cells of Voronoi honeycombs introduce a small change in the elastic properties of isotropic Voronoi honeycombs. They also studied the sensitivity to defects inferring that they have significant impact on the effective mechanical properties of Voronoi and regular honeycombs. Likewise, one of the few studies regarding the dependency of irregularities on Voronoi honeycombs on irregularities have been presented by Zhu et al., [17]. The authors defined and analyzed the influence of the cell irregularity on the mechanical response of periodic Voronoi honeycombs at high levels of strain. Contrary to the common practice, they generated Voronoi honeycombs with different levels of regularity in order to understand its influence. However, Zhu et al., [17] restricted their results to 2D analysis and concede a restriction in FEA simulations when cell ligaments come in contact to likely influence their results significantly. Like Zhu et al., Borovinek [18] studied the effect of irregularity on the crushing response of open cell foams. However, their conclusions differ in terms of elastic modulus prediction. While Zhu et al., suggest an inverse relation between

modulus and regularity, Borovinek infers a direct one. Thus, research to clarify this ambiguity is also desirable.

The FEA has also been applied to analyze interpenetrating phase composites by Jhaver and Tippur [19]. They demonstrated the advantages of IPC by using 3D aluminum scaffolds infused with syntactic foam. The authors studied the effect of the variation in the volume fraction of microballons (in syntactic foams) on the compression response of regular foam-filled honeycombs and IPC. Improvements in the elastic modulus and plateau strength values by as much as 31% and 39%, respectively, are reported. They also analyzed the directional dependency of foam-filled honeycomb experimentally and numerically. Unlike regular honeycomb structures, which show a dependency on the direction of loading (L or W), Javher and Tippur [19] did not find a strong directional dependency for foam-filled honeycombs. Their experiments however showed a modest increase in the plateau strength for specimens loaded in the W direction. This is a result that is not obvious due to the fact that the opposite is true for honeycomb structures (see [12, 13]).

With the increase of the data processing capacity of computers and development of high level programming languages, simulation and modeling of foams are being extended to the third dimension. Jang et al., [20] conducted a detailed study of the morphology of open cell aluminum and polyester urethane foams by means of micro-computed X-ray tomography. The authors revealed that cross section of struts in polyester urethane foams has a hypocycloid shape traditionally known as Plateau border. In the same fashion, the cross section area for aluminum foams is between triangular and circular shapes. Certainly, the Plateau border shape of polyester urethane foams is a direct consequence of Plateau's second law which states that three faces meet at 120 degrees in a soap film. Moreover, the area of cross section along the struts varies in relation with its location relative to the nodes; the closer to the nodes, the greater is the cross sectional area. For modeling in FEA, the authors

idealized the foam as a regular assembly of tetrakaidecahedron cells, as a perturbation of tetrakaidecahedron cells, and as random foams. The models have accurately predicted the elastic modulus although random foams were 5 to 10% stiffer. Turning to IPC analysis in three dimensions, Periasamy and Tippur [21] conducted an experimental and numerical analysis of IPC foams under dynamic compression. A split Hopkinson pressure bar apparatus was employed to evaluate stress-strain curves for syntactic epoxy foam-filled aluminum scaffolds. Moreover, a tetrakaidecahedron representative volume and infinite eight node brick elements proved to be an efficient strategy for modeling interpenetrating phase composites subjected to stress wave loading. Likewise, representing foam with a tetrakaidecahedron idealization has been successfully applied by many researchers (see [20-22]). However, the tetrakaidecahedron structure cannot accurately represent the structure of metal foams [23]. A statistical comparison between ninety years of experimental observations of microstructures in real foams and tetrakaidecahedron scaffold was developed by Raj in 2011 [23]. By means of optical tomography of FeCrAlY foams and microstructural observations of foams available in the literature [24-26], the author concluded that tetrakaidecahedron cannot accurately describe the FeCrAlY foam cell structure. For instance, the most common polygon forming the cell faces in real foams has five edges while none of the faces in a tetrakaidecahedron representation has that configuration. Thus, in order to accurately represent the geometry of real foams, a new approach is required. Nonetheless, the approach must be able to represent the complex morphology of foams, yet relatively simple to be handled with the computational resources available. Therefore, Voronoi approach has been extended to the three dimensional space to accomplish this objective. Researchers such as Zhu et al., [27], Borovinsek [18] and Jang et al., [20] have successfully generated 3D representation of foams based on the Voronoi diagrams. However, none of them have studied the effect of regularity in the context of an IPC and normally the geometries generated have

been limited to a small number of cells. Moreover, the regularity parameter is sometimes not even mentioned in an important number of studies available in the literature (see for instance [14, 15, 20, 28]). Commonly, the geometries generated by Voronoi diagrams are referred to as random foams. Nevertheless, it is important to identify the level of randomness from a quantitative stand point before modeling using FEA, so that the results can be interpreted accurately.

1.4. Objectives

The present research is aimed towards understanding the influence of regularity on the compression response of aluminum foams and syntactic foam-aluminum foam IPCs in a sandwich configuration. This particular investigation is part of an ongoing study to develop interpenetrating phase composites for potential applications in aerospace and military industry. The following are the specific objectives:

- Establish a procedure to virtually generate 2D geometric representation of metal foam morphology by generating pseudo random seed points in a two dimensional space and apply the Voronoi tessellation technique.
- Select a suitable index for quantifying the level of randomness of a specific foam structure in two and three dimensions.
- Develop a two dimensional finite element model to capture the linear and nonlinear responses representing aluminum foam specimens under compression in a sandwich configuration.
- Study the effect of regularity on the compression response of aluminum open cell foams represented by 2D random geometries in a finite element environment.

- Analyze the effect of relative density on the crushing response of two dimensional random foams and compare the response to analytical models available in the literature.
- Generate a two dimensional finite element model in order to capture compression response of aluminum foam-syntactic foam composites in both the linear and nonlinear regimes.
- Understand the role of the regularity parameter on the compression response of foam-filled Voronoi honeycombs in both the linear and nonlinear regimes.
- Extend the method of generating random foam geometries to three dimensional space and quantitatively measure regularity levels of geometries generated by means of pseudo random seeds and spatial Voronoi tessellations.
- Explain the role of tetrakaidecahedron foams and regular hexagonal honeycomb representations as a particular case of random foams and quantitatively describe their regularity.
- Generate an efficient 3D finite element model for aluminum foams to accurately capture the mechanical response of metal foams within the computational resources available at Auburn University.
- Demonstrate the feasibility of constructing random foams by means of Additive Manufacturing techniques following a three dimensional virtual design and suggest improvements in the morphology of metal foams and interpenetrating phase composites that cannot be easily realized using common production procedures.

1.5. Organization of the thesis

The present dissertation is divided into seven chapters. The first is an introductory chapter which is essentially preparatory in nature. It includes motivation for the research,

literature review and a general overview of cellular solids, metal foams along with interpenetrating phase composite architectures. The second chapter presents a detailed overview of the mathematical concepts and the theory behind Voronoi approach with an emphasis and exposure to general Euclidean spaces. Mathematical concepts presented are generally valid for different dimensions and will be the strategy adopted in the present thesis. The specific algorithms for generating pseudo random seed points in two and three dimensional spaces are discussed in the third chapter. Additionally, scripts for partitioning of space and techniques of creating random geometries using computer aided design software are also detailed in this chapter. In chapter four, a finite element model to represent aluminum foam in a two dimensional space is developed. An analysis of the influence of regularity and relative density on the compression response of Voronoi honeycombs is discussed in this chapter. Chapter five deals with modeling interpenetrating phase composites in two dimensions. It differs from chapter four in one important aspect. In this chapter two phases are made to interact with each other to capture the mechanical response of foam-filled Voronoi honeycombs. Details such as relevant material properties, model discretization and boundary conditions are fully discussed. The 3D version of modeling of aluminum foams is explored in chapter six. The geometry is no longer represented by a Voronoi honeycomb but by a true 3D Voronoi foam. Finally, summary and conclusions of the present research are offered in chapter seven along with a few potential future research directions.

CHAPTER 2

VORONOI DIAGRAMS

Patterns on a giraffe's skin, a dry lake bed, a honeycomb, a section of balsa wood, a trabecular bone, grains of a metal, sponge, coral, bread, cork are some natural manifestations of a related phenomenon (see Fig. 2.1).

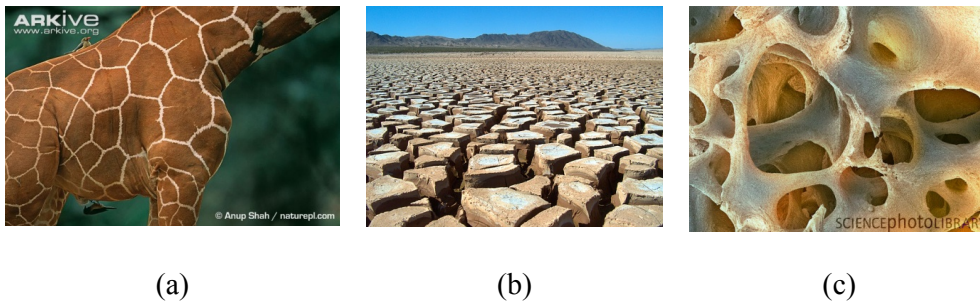
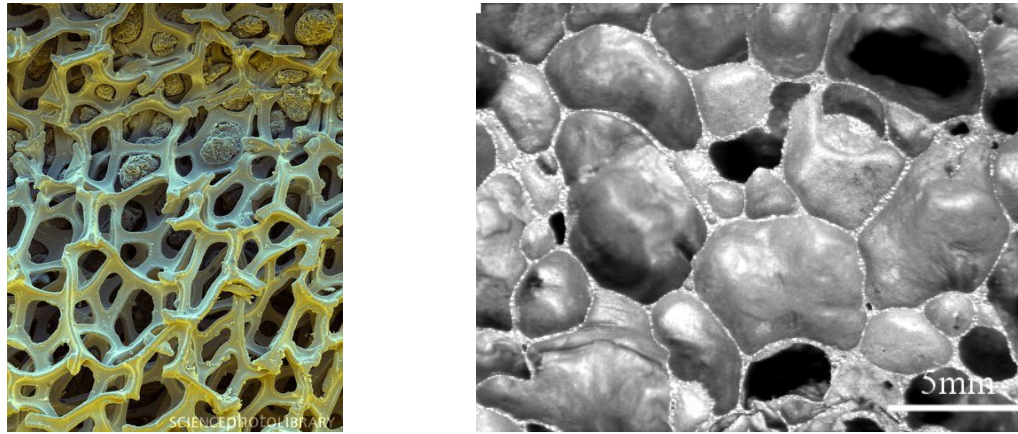


Figure 2.1: Examples of natural division of space: (a) giraffe skin pattern (arkive.org), (b) a dry lake bed (wunderground.com), (c) osseous tissue (sciencephoto.com).

It is not a mere coincidence that these natural shapes and microstructures look similar. Indeed, all of them follow common natural laws during formation. As mentioned in the last chapter, nature and humans usually take different approaches to construct structures. Most of the human construction methods are based on extracting (removing) material from a bulk to obtain the final product. Natural ways of construction, however, are mainly based on an additive process [1]. Nevertheless, humans have learned how to create products by simulating natural processes. For example, metal, syntactic and polymeric foams, and even some food products such as bread, meringue, and ice cream are just a few products where humans mimic natural approaches to generate the final product. During the creation of the goods mentioned, humans only set up the initial conditions and do not have a complete control over the final

shape of the product [6]. Consequently, complex products can result, as in the examples presented in Fig. 2.2.



(a)

(b)

Figure 2.2: Metal foam structures: (a) nickel foam, open cell structure (sciencephoto.com), (b) aluminum foam, closed cell structure (from [29]).

The present study focuses on modeling open cell aluminum foams as a structure in the context of an IPC. Recall from the previous chapter that interpenetrating phase composites (IPC) are multiphase composites in which individual phases are intermingled and co-continuous in a 3D space. Exact analytical equations for such random geometries have not been developed, and numerical approximations are quite useful. Among them, finite element methods have been successfully applied to study the mechanical behavior of metal foams and interpenetrating phase composites [19, 20, 28, 30, 31]. According to Strano [32], homogenization, realistic reconstruction, and repetition of standard unit cells are the three most common approaches to successfully simulate metal foams using finite element methods (FEM). Homogenization approaches model the foam material as a continuum, paying little attention to the geometry of the foam at the micro or mesoscale. On the other hand, studies on realistic construction and repetition of standard unit cells direct their efforts towards the geometry of foams. Indeed, the most efficient way to construct the geometry of foams is by

repeating standard unit cells. For instance, one of the most widely used techniques applied for analyzing metal foams is based on the repetition of a standard tetrakaidecahedron cells (see [20-22]). The efficient volume to surface area representation of space using tetrakaidecahedron cells is schematically shown in Fig. 2.3.

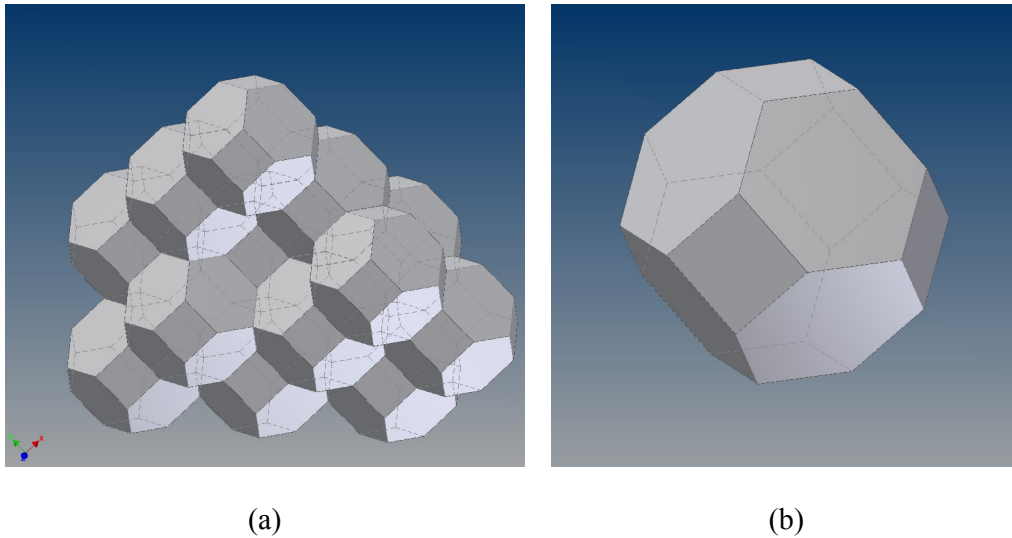


Figure 2.3: (a) Tetrakaidecahedron cell based foam representation, (b) Isolated tetrakaidecahedron cell.

Although tetrakaidecahedron cells have been successfully used for idealizing foams, the arrangement of cells does not completely capture the microstructure of foams [23]. A different technique to realistically construct the geometry of foams is to create a three dimensional volume using tomographic information of real foams. However, the lack of resolution and cost can be an issue in its application to real world problems (see [33, 34]). Another approach capable of capturing the essential characteristics and imperfections present in aluminum foams is based on the Voronoi diagrams and will be the one utilized in the present thesis. Before explaining the procedure of constructing a Voronoi diagram, some mathematical concepts need to be understood first.

2.1. Mathematical concepts

a) Convex and non-convex sets

A formal definition for convex sets can be found in Okabe [35]. Let A be a set defined in the m dimensional Euclidean space. Quoting Okabe, “Formally, if for any two points x_1 and x_2 in A the line segment joining the points is contained in A , i.e.,

$$\lambda x_1 + (1 - \lambda)x_2 \in A \text{ for all } 0 \leq \lambda \leq 1,$$

then we call the set A a *convex set*; otherwise, a *non-convex set*”. Figure 2.4 shows a general representation of a convex set (a) and a non-convex set (b) for a $m = 2$ Euclidean space.

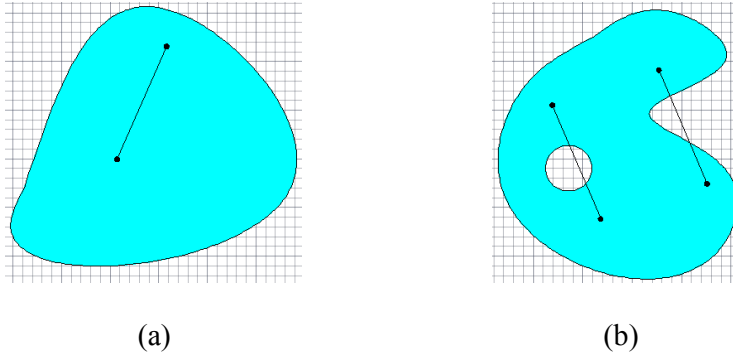


Figure 2.4: (a) convex set, (b) no convex set in $m = 2$

(drawn based on concepts in reference [35]).

Informally, if no holes or discontinuities are present in the trajectory of a line in the interior of a set, the set is defined as a convex set (Fig. 2.4(a)). On the other hand, if holes or discontinuities are present in the trajectory of a line in the interior of a set A , the set is defined as a non-convex cell (Fig. 2.4(b)). It is important to note that in convex analysis, it can be shown that the intersection of any two convex sets is another convex set (see [36]).

b) *Convex hull*

According to Okabe [35], for a set A defined in a m -dimensional Euclidean space, the intersection of all the possible convex sets that contain A is the *convex hull* of the set A . For a $m = 2$ Euclidean space, Okabe asks us to imagine a flexible rubber band encircling the set A . All the points in the interior of the rubber band constitute the convex hull of the set A . In Fig. 2.5, a general set A is encircled by a rubber band to show the border of the convex hull and the convex hull is created by grouping all the points in the interior of the rubber band.

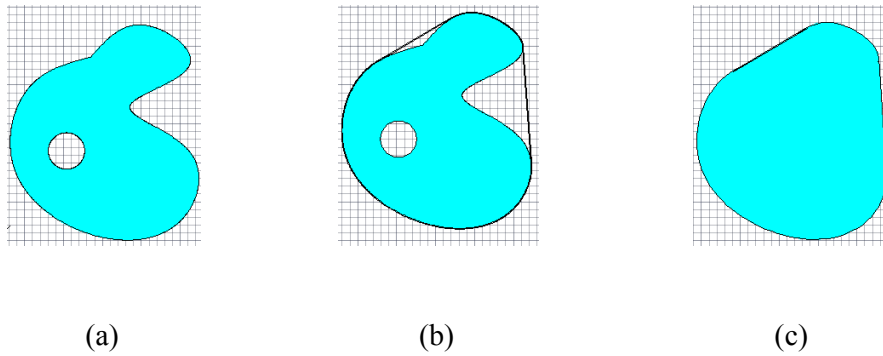


Figure 2.5: (a) no convex set A , (b) boundary of the convex hull of A ,
(c) convex hull of A (in $m = 2$, concept from [35] redrawn).

The analogy of the rubber band in the $m = 3$ Euclidean (3D) space would be a rubbery skin. For instance, for the torus presented in Fig. 2.6, the convex hull of the torus is created as a result of the intersection of all possible convex sets that contain the torus. As a result, the convex hull of the torus does not have any holes or discontinuities in the interior of the set. (see Fig. 2.6(b))

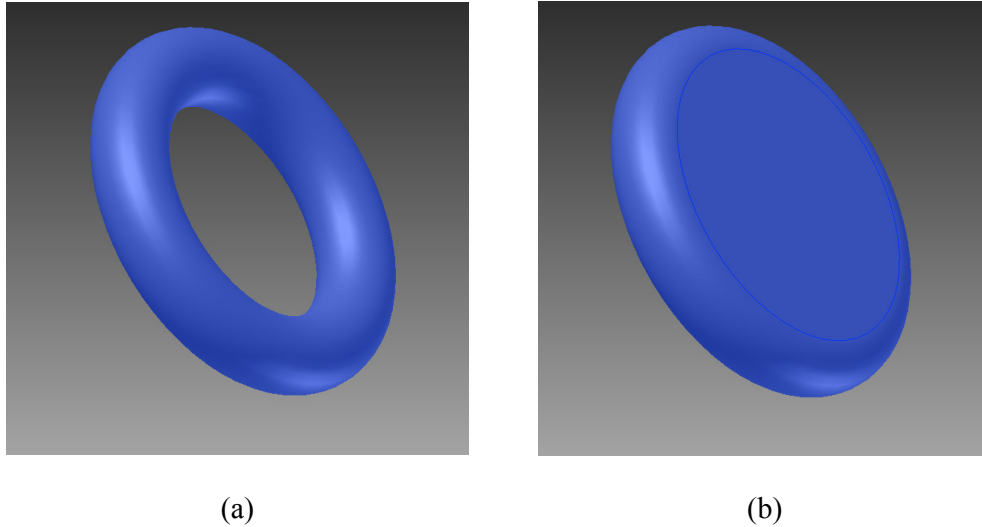


Figure 2.6: (a) no convex set A, (b) convex hull of A ($m = 3$).

c) Spatial stochastic point process

A detailed explanation of the generation of metal foams can be found in Ashby [6]. He classified the methods of generating foams into nine types. All of them involve generation of porous structure in metal foams based on growth of bubbles in space or are based on a template produced by this process. Furthermore, quoting Silva [14], “Cellular solids are often formed by the nucleation and growth of bubbles.” The location of the initial bubbles can be represented as points in space due to their relative small size compared to the whole structure. Consequently, an analysis of a pattern of points in space is required. According to Okabe [35], point patterns can be classified into three classes, namely, complete spatial randomness (CSR), clustered, and regular. Examples of these three classes can be visualized in Fig. 2.7.

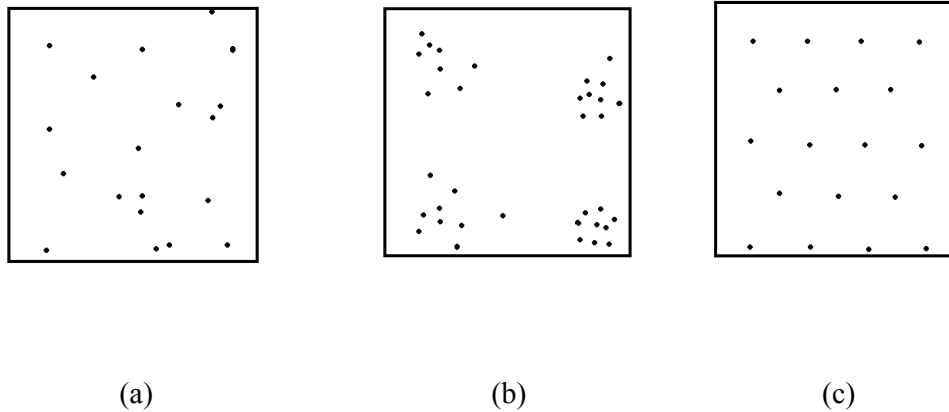


Figure 2.7: Types of planar point patters: (a) complete spatial randomness (CSR), (b) clustered, (c) regular ([35, 37]).

In a complete spatial randomness process, points are randomly generated in space following a probability distribution function (Fig. 2.7(a)). For that reason, all the regions inside the control region (denoted by a square box in Fig. 2.7) have similar density of points. In contrast, the density of points is different in some regions in the clustered point pattern (Fig. 2.7(b)). This type of point pattern could be useful to analyze certain phenomena where points attract one another during generation or in the analysis of, say, functionally graded foams. Additionally, in a regular point pattern, points do not show any randomness and the distance among them is equal without any specific zones with higher point densities. Moreover, foams generated with bubbles that have nucleated in clustered point patterns (Fig. 2.7(b)) are commonly called polydisperse foams while those generated from complete spatial randomness and regular point patterns generate monodisperse foams. The analysis of foams generated from bubbles nucleating from a completely random spatial pattern is the main interest of this study. For that reason, the distribution function that governs the generation of points (or ‘events’ in probability theory) in a general Euclidean space needs to be understood. According to Guenter [38], if:

- “Events that occur in one time interval (or, region of space) are independent of those occurring in any other non-overlapping time interval (or, region of space).
- For a small time interval (or region of space) the probability that an event occurs is proportional to the length of the time interval (or region of space).
- The probability that two or more events occur in a very small time interval (or region of space) is so small that it can be neglected,”

then, for a discrete variable, the probability function governing the generation of points into any subset A can be described with a homogeneous Poisson distribution defined as,

$$\Pr(N(A) = x) = \frac{\lambda |A| e^{-\lambda |A| x}}{x!}, \quad x = 0, 1, 2, \dots$$

where A is a subset in a real space (R^m), x is the number of points to be generated, λ is the density of points and $\Pr(N(A) = x)$ stands for probability of x number of points to be placed in the subset A . Therefore, points generated in the subset A under the Poisson distribution have the same probability to be generated in any location [35, 37], so point patterns as the one shown in Fig. 2.7(a) are generated. However, in the analysis of certain phenomena, a complete spatial randomness point pattern does not always describe what is observed. For example, imagine that the points generated randomly represent trees of a certain type growing in a field. When two trees grow too close to each other, the stronger tree kills the other by competing for soil, sun and other resources. As a result, the final distribution of trees exhibits some degree of regularity. Similarly, in the field of computational geometry, two approaches can be considered to eliminate points that are closer than a certain distance s . First, a number of points n can be generated in the set A and subsequently points that are too close can be eliminated. As a result, the complete spatial randomness process generates a more regular distribution of points. However, the final output contains less number of points

than the initial condition (n). Alternatively, a different approach is the so-called Simple Sequential Inhibition (SSI) process.

d) Simple Sequential Inhibition (SSI) process

In a Simple Sequential Inhibition process, points in space are generated in a set A based on a completely random process described by the Poisson distribution. After each point is generated, its distances with respect to the previous ones are evaluated. If none of the distances is greater than a certain value s , the point is kept; otherwise it is eliminated. The process continues until n points are generated in the set A . The effect of introducing the inhibition distance s is to generate a more regular pattern of points. For instance, Fig. 2.8(a) shows a pattern of 100 point generated on a one unit square area based on Poisson distribution while in Fig. 2.8(b) and 2.8(c) distances of inhibition of $s = 0.05$ and $s = 0.1$ have been introduced, respectively.

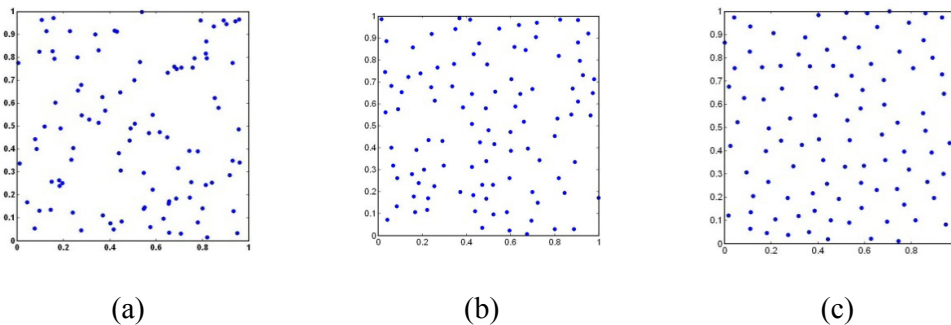


Figure 2.8: Planar point patters for $n = 100$ in a unit square with inhibition distance (a) $s = 0$, (b) $s = 0.05$, (c) $s = 0.1$.

As we increase the value of s , the pattern of points is more regular (see Fig. 2.8(c)). However, demand for more computer resources increases as s increases making the process of generation of points very difficult if not impossible for higher values of s . For instance, if we use $s = 2$ as the inhibition distance for the examples presented in Fig. 2.8, a determinate algorithm will generate one point in a 1×1 square area, but no more points will be placed.

The reason is that the locations inside a square of unit length cannot fill the minimum requirements of $s=2$ with respect to the first point generated. Consequently, whether there is a maximum value beyond which it is impossible to place n points inside a certain area A is a question that arises in the analysis. Moreover, the probability of achieving a fully regular arrangement of points based on SSI process is very small even with infinite computational resources, so a different approach is necessary for achieving highly regular configurations. For instance, instead of increasing the regularity of the pattern of points starting with an irregular arrangement, a regular one could be used as a starter and perturb the location of points.

e) Perturbation process

The Simple Sequential Inhibition (SSI) process is a very simple approach in order to obtain point patterns more regular than the ones generated in a complete spatial randomness (CSR) process. However, as stated in the last section, the probability of achieving a fully regular arrangement of points based on SSI is very small. Indeed, it implies that the first point was randomly generated in the exact position of a regular arrangement of points. Subsequently, the second and all the other points were also randomly generated in a regular position. Evidently, the probability of it occurring during a simulation is extremely low but not zero. For that reason, a perturbation process has been applied in the present study to generate highly regular arrangement of points. In contrast to the SSI process that has a completely random spatial arrangement of points at the beginning, in a perturbation process a regular arrangement of points is the initial state. Points are directly located at regular intervals in a 2D or 3D space and a perturbation is introduced by varying their coordinates (x,y) in 2D or (x,y,z) in 3D. The amount of perturbation must be directly related to how much disorder is to be introduced into a regular arrangement. For that reason, it is important to quantify the order or disorder of a specific pattern of points.

f) Definition of regularity

According to Zhu et al., [17], the distance between two points in a regular and planar arrangement of points similar to the one presented in Fig. 2.7(c) can be calculated using,

$$r = \sqrt{\frac{2A}{\sqrt{3}n}}$$

where r is the distance between two neighboring points in a regular planar point pattern (see Fig. 2.7(c)), and A is the area inside which n points are located [17]. In an earlier study Zhu [27] also presented a formula for calculating the distance r between two neighboring points in a spatial body centered packing of points,

$$r = \frac{\sqrt{6}}{2} \left(\sqrt{\frac{V}{\sqrt[3]{\sqrt{2}n}}} \right)$$

where V is the volume inside which n points are located. Therefore the regularity can be measured by relating the inhibition distance s with respect to the maximum value r [17, 27] as,

$$\delta = \frac{s}{r}$$

In the present thesis δ will be referred to as the regularity parameter or simply “regularity”. A value of $\delta = 1$ implies a regular arrangement of points (see Fig. 2.7(c) for a 2D example) while $\delta = 0$ represent a complete spatial randomness of points (see Fig. 2.7(a)). This definition is similar for both 3D and 2D spaces. For that reason, a value of $\delta = 1$ in a 3D space implies a regular arrangement of points in a body centered packing as the example shown in Fig. 2.9(a). Similarly, a value of $\delta = 0$ represents a complete spatial randomness of points as shown Fig. 2.9(b).

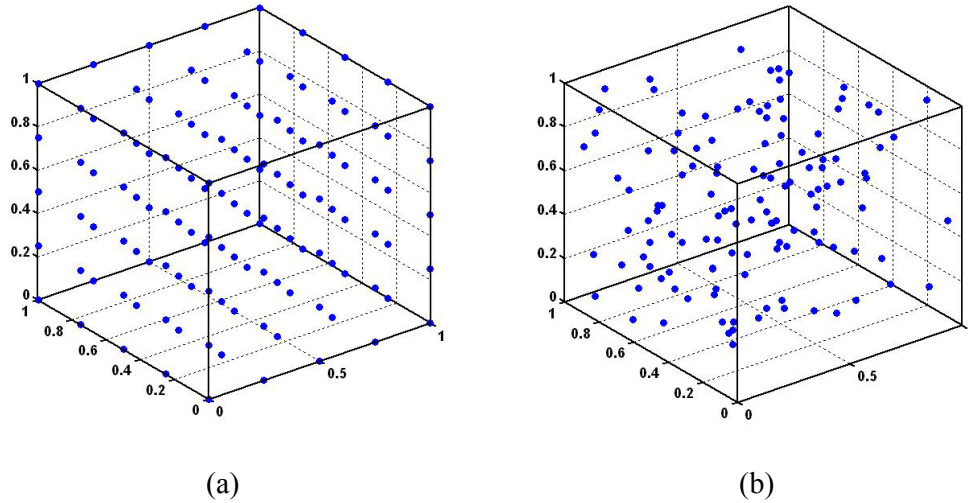


Figure 2.9: Three dimensional point pattern in a unit cube for $n = 125$ with regularity

parameter: (a) $\delta = 1$, (b) $\delta = 0$.

Therefore, in order to define the regularity of a specific point pattern, one can either indicate the inhibition distance s or the inhibition distance as a proportion of the maximum distance allowed. From this point forward, the order or disorder of a pattern of points will be characterized by δ . However, it is important to mention that, in the present thesis there are two ways to generated random point patterns namely SSI and perturbation process. *In both cases the regularity can be characterized with the parameter δ although they are not comparable. In other words, a pattern of points with regularity, say $\delta = 0.7$, generated from a SSI process is not comparable with a pattern of points with the same regularity but generated with a perturbation process. However, this rule obviously does not apply for the extreme value of $\delta = 1$.*

2.2. Voronoi diagram - Definition

When it is necessary to understand the influence of a determinate event in space that surrounds it, and the event is sufficiently small compared to the space, then it can be represented by a point. Then, a Voronoi diagram can be a good starting point for analysis [35]. For instance, the event or more generally the events can be bubbles growing in space,

fish swimming in the seabed or black holes absorbing light at different locations of our galaxy. In this and other examples, researchers need to associate the regions of space close to each event. The result of this association is the so-called Voronoi diagram. Many natural phenomena can be associated with Voronoi diagrams [35, 39-41]. For that reason, it is not surprising that the Voronoi diagram concept has been applied to different fields such as archeology, biology, crystallography, physics, urban planning, and forestry [35, 39-41].

Mathematically, given a set S of n points in a R^m dimensional space, the process of associating all the locations of the R^m space into polyhedral regions $v(p)$ ($p \in S$) with the closest point of S is called Voronoi partitioning process. The polyhedral regions $v(p)$ are called cells and are formally defined as:

$$v(p) = \{x \in R^m \mid \|x, p\| \leq \|x, q\| \quad \forall q \in S - p\}$$

where $\|*\|$ is the distance function between the two points (see [40]). The union of all the cells is then referred to as a Voronoi diagram.

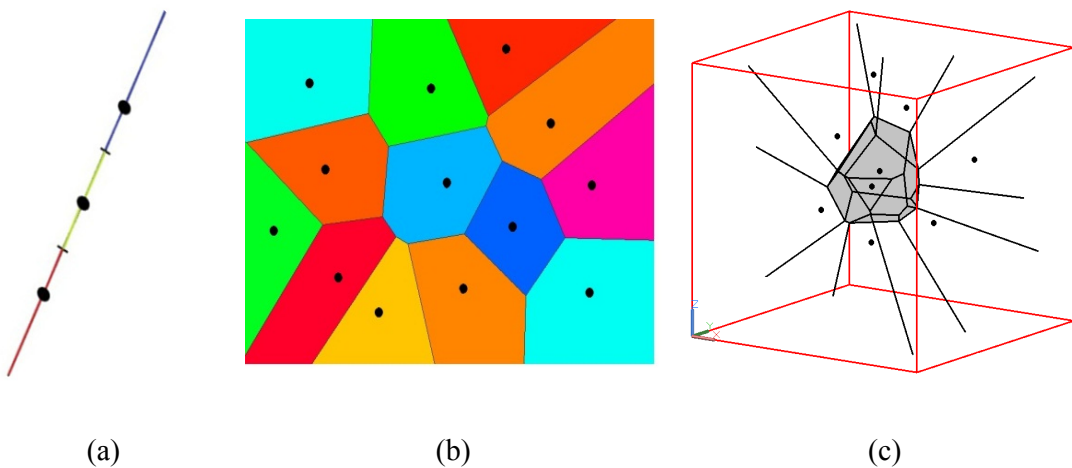


Figure 2.10: Voronoi diagrams in different dimensions: (a) $m = 1$, (b) $m = 2$, (c) $m = 3$.

Theoretically, a Voronoi diagram can be constructed in any dimensional space with $m > 0$. For instance, representations of Voronoi diagrams for lower dimensional spaces $m = 1, 2$ and 3 are presented in Fig. 2.10. However the concept is so broad that it can be easily generalized to higher order dimensions using the same basic concepts. From Fig. 2.10, it is clear that the number of regions or cells formed after a Voronoi partition process is equal to the number of nuclei or events. Also, the limit between two neighboring cells has a $(m - 1)$ dimension. For instance, the limits of cells in a 2D Voronoi diagram are lines (1D entities). Similarly, the limits of cells in a 1D Voronoi diagram are points (0D entities). Furthermore, cells can be classified into unbounded and bounded regions depending on whether the size of the cells is infinite or finite, respectively.

The process of constructing a Voronoi diagram for a given set of points in 2D can adopt the following procedure. First, a Delaunay tessellation needs to be performed between the given points. The Delaunay tessellation in 2D is created by drawing triangles with the nuclei as vertices, but the triangles must satisfy one important requirement. The circle circumscribing the triangle should not enclose any other nucleus points. Subsequently, the Voronoi diagram can be constructed by generating perpendicular bisectors of the sides of those triangles [35, 39, 40]. For instance, Fig. 2.11 shows a plot of a Voronoi diagram (dashed lines) and the Delaunay tessellation (solid lines) for a set of 30 points. Figure 2.11(b) graphically demonstrates that no other nucleus point is contained inside the region enclosed by a circle circumscribing an arbitrary triangle. The same is true for the rest of the triangles. Construction processes in other dimensions can follow the same procedure. For instance, triangles will be replaced by tetrahedrons, lines by planes and circles by spheres for the 3D case shown in Fig. 2.10(c).

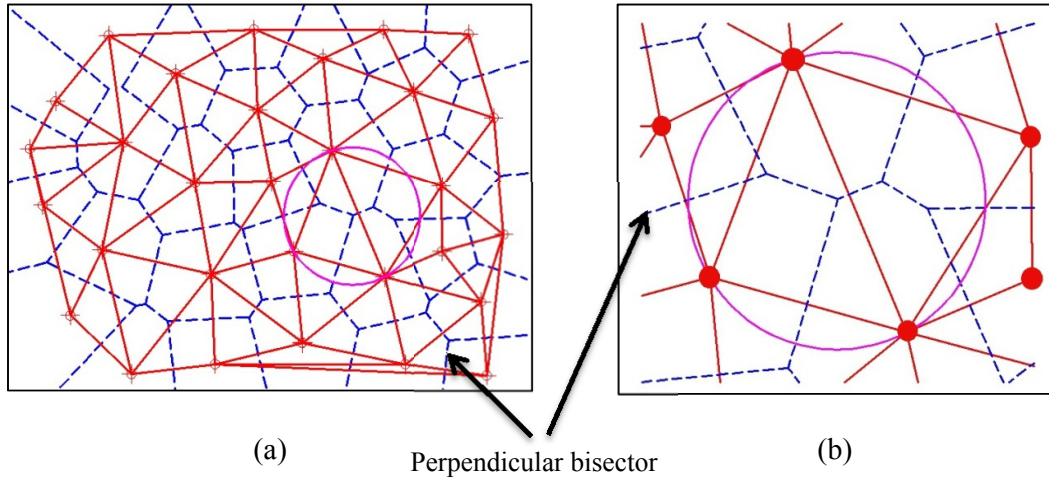


Figure 2.11: (a) Voronoi diagram (dashed lines) and Delaunay tessellation (solid lines), (b) no nucleus point is present inside the circumscribing circle.

According to Boots [42], a Voronoi diagram can be viewed as the limiting case of a bubble growth process with assumptions, namely,

- Seed points are generated in space simultaneously,
- The rate of growth of bubbles from each point is the same,
- The rate of growth is linear and equally weighted in all directions,
- Seed points remain in the original position during the growth process,
- Growth normal to the bubble is interrupted in a specific direction when a cell touches a neighboring cell.

CHAPTER 3

MODELING FOAM GEOMETRY

In chapter 2, theoretical concepts behind the approach used for random generation of cellular foams have been detailed. The present chapter applies those concepts and procedures to construct 2D and 3D geometries for simulation using the finite element method (FEM). The MATLAB® software package is used for generating random points and partition space while the family of 3D CAD software programs from Autodesk, Inc. is employed for constructing model geometries. Specifically, Autodesk Inventor 2012 for solid modeling and AutoCAD 2012 for constructing lines structures are used. AutoCAD is chosen among other CAD programs due to the features to design geometries from user defined scripts. In fact, Lisp programming language of AutoCAD allow designers to accomplish tasks that would be time consuming or practically impossible in a graphical user interface (GUI). By means of scripts, the repetitive task such as the creation of cells in foams can be programed with coded instructions. In addition, computer applications that can be integrated with AutoCAD are accessible for performing different types of tasks. For instance, the commercially available application InnerSoft v. 2.9.1 [43] is utilized here to create convex hulls for a set of points.

Before starting the process of creating geometries for cellular foams in a virtual environment, designers should clearly define the following characteristics of the foam to be constructed:

- a) *Dispersity*. Monodisperse or polydisperse are the two categories in which foams can be classified based on the type of point-pattern precursor used. Recall from previous chapters that clustered nuclei patterns such as the one presented in Fig. 2.7(b) generates polydisperse foams.

- b) *Configuration*. Foams can have two basic configurations based on the type of geometric entities separating their cells, namely the open and the close variety although alternative nomenclature such as reticulated or non-reticulated foams can also be applied, respectively (see section 1.2(a) and Fig. 1.2).
- c) *Directional geometric dependency*. If a foam exhibits some geometric directional dependency, it is referred to as anisotropic. Otherwise, the foam is isotropic. Geometric anisotropy in foams can be generated in the initial steps of foam construction or at the end of the process. For example, generating nuclei randomly in a control volume and affecting, say, the y coordinate by a factor α will result in a Voronoi diagram with an anisotropy in the y direction proportional to α . Alternatively, an isotropic foam can be generated following the procedure conceptually defined in chapter 2, and anisotropy can be introduced as a final step. In short, an elongation in a particular direction can be effortlessly applied in a CAD software simply by scaling the geometry in a chosen direction. Thus, the elongation can be proportional to α producing the same result.
- d) *Regularity*. This is self-explanatory (refer to 2.1(f))
- e) *Size*. The number of cells to be generated for a particular foam design is directly related to the control area (2D) or control volume (3D) and the density of cells. The density of cells is normally supplied by the manufacturer as pores per inch.
- f) *Dimensionality*. In the present thesis, geometries will be generated in 2 or 3 dimensions.
- g) *Cross sectional shape*. Geometric entities describing ligaments of open cell foams can be represented by lines of zero thickness (essentially 1D entities) or by solid struts with a cross sectional area associated with the line. Foams represented by lines without thickness are commonly referred to as “dry foams” (see for instance [44]).

Otherwise, foams are referred to as “wet foams”. Figure 3.1 graphically illustrates the difference between a dry (Fig. 3.1(a)) and a wet (Fig. 3.1(b)) open cell. Similarly, closed cell foams can also have a wet or dry configuration. In a dry configuration, cell faces will be represented by planes of zero thickness emulating soap film foams. On the other hand, the wet configuration of closed cell foams will be represented by planes of finite thickness. However, closed cell foams are beyond the scope of the present thesis.

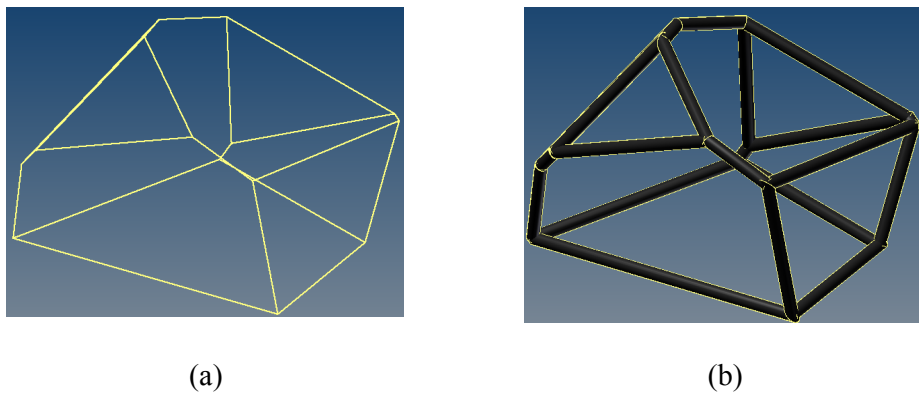


Figure 3.1: A single open cell of a foam: (a) dry configuration, (b) wet configuration.

h) *Density*. When the cross sectional shape of an open cell foam representation is defined, the cross sectional dimension depends on the density of the foam. A direct relationship between density and cross sectional dimensions is obvious.

In this thesis, characteristics (a), (b) and (c) are already defined due to the fact that we will be dealing with monodisperse, open, and isotropic foams. However, the method developed in the present chapter can be used to create polydisperse, closed, anisotropic foams or a combination of these characteristics with the same basic procedure. Considering characteristic (d), the primarily objective of the present research is to understand the influence of regularity on the mechanical response of open cell aluminum foams and

Interpenetrating Phase Composites, or IPCs. Specifically, open cell foams made of AL 6101-T6, pore density $\cong 40$ ppi, relative density $\cong 9\%$ manufactured by ERG Inc is considered during modeling. For that reason, geometries with different levels of regularities are constructed since regularity in real foams is uncertain. In fact, methods for quantifying regularity of real foams have not yet been proposed. Next, the size (e) or the number of cells can be calculated from the control area or control volume and cell density. According to the manufacturer, pore density of 40 ppi implies 22 to 26 cells per inch on average. Thus, it can be assumed that the average cell density is equal to 24 (cells per inch) with an average individual cell size of approximately 1.06 mm (0.042 in). Therefore, the number of cells for a model can be calculated with the cell density and the size of the control area (2D) or volume (3D). The size of the control area should be sufficiently large to capture the compression response of metal foams. A few studies are available regarding specimen size effects in foams. For the 2D case, Tekoğlu et al., [16] suggested a ratio of the control area to cell size of greater than or equal to 16 for uniaxial compression simulations. In this thesis, a control area corresponding to a ratio of the area size to cell size equal to ~ 16 has been selected. For the 3D case, Andrews et al., [45] conducted an experimental study of the influence of the size specimen into the compression response of open (Duocel) and closed (Alporas) aluminum foams. They concluded that elastic modulus for both foams is well predicted with a ratio of the specimen size to cell size of 6. In this thesis, a control volume corresponding to a ratio of the volume size to cell size equal to ~ 6 has been selected for simulations. Regarding the cross sectional shape, Jang et al., [20] conducted a detailed study of the morphology of open cell aluminum foam by means of micro-computed x-ray tomography. The authors determined that the ligament cross sectional area of open cell aluminum foams is in between triangular and circular. In the present study, for the sake of simplicity, a constant circular cross sectional shape is adopted. In addition, the value of the radius/thickness of struts depends on the density of the foam. In two dimensions it can be estimated by the formula (see [27, 31]),

$$\bar{\rho} = \rho^* / \rho_s = \left(\frac{1}{A} \right) \sum_{i=1}^N h_i l_i$$

where $\bar{\rho}$ is the relative density of the foam, ρ^* is the density of the cellular material, ρ_s is the density of the solid, N is the number of struts in the cell, h_i is the thickness of struts, l_i is the cell wall length and A is the control area. Similarly, in three dimensions the thickness of struts can be estimated from the formula,

$$\bar{\rho} = \rho^* / \rho_s = \left(\frac{1}{V} \right) \sum_{i=1}^N A_i l_i$$

where A_i is the cross sectional area of the struts and V is the control volume.

The process of constructing random Voronoi foams and honeycombs in more general condition (3D solid) can be divided into five levels identified with letters (a, b, ..., e) in Fig. 3.2. Flowchart presented in Fig. 3.2 schematically represents the five stages required to construct a honeycomb (2D) or a foam (3D) along with the necessary software packages.

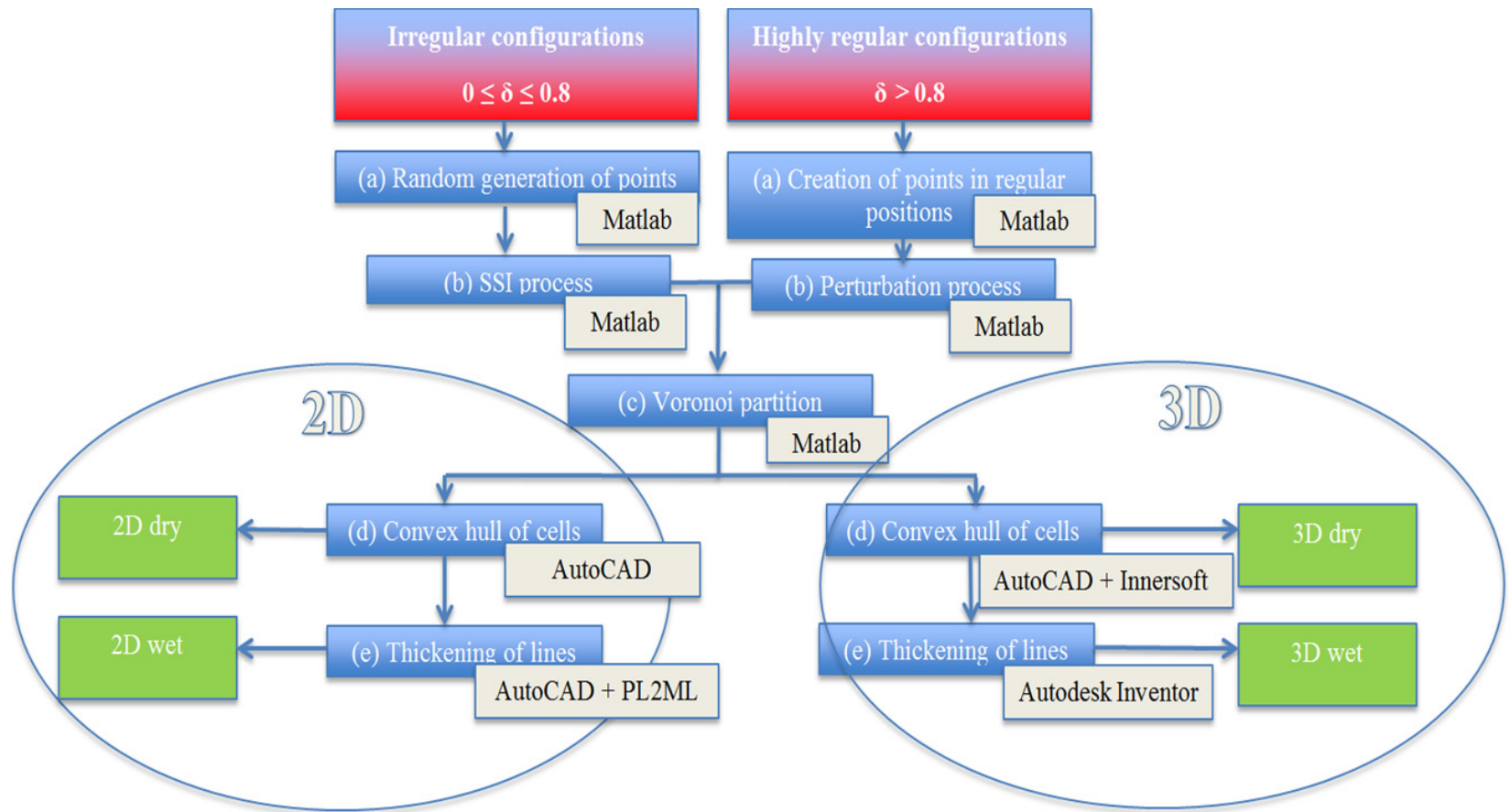


Figure 3.2: Flowchart for constructing Voronoi honeycombs and foams. (SSI: Simple Sequential Inhibition process)

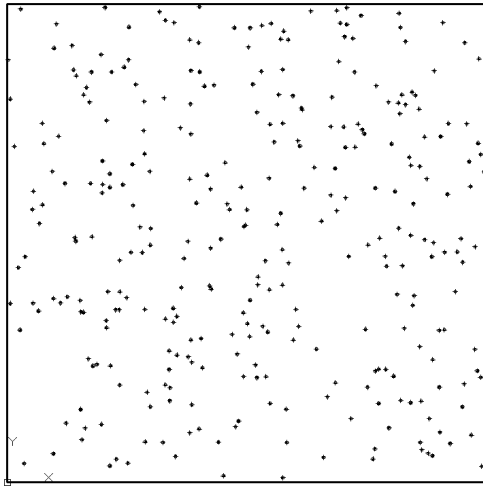
3.1. Geometric construction of 2D Voronoi honeycombs

(a) Random generation of points and (b) Simple Sequential Inhibition (SSI) process

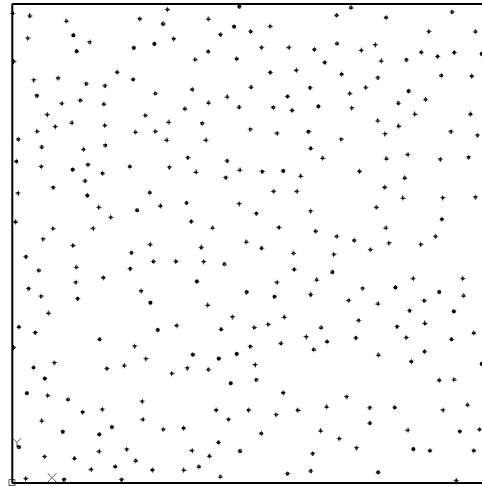
Concepts governing random generation of points have been introduced in section 2.1(c). In the present section we focus on the random generation of points in space. A number of algorithms for random generation of points have been proposed (see for instance [37, 46, 47]). In the present section, the code for Matlab proposed by Martinez [37] has been used for random generation of points and SSI process. The relevant code is listed in Appendix B. The input for the SSI code consists of the control area (A), the number of points (n) to be placed inside A , and the inhibition distance (s) between points. In the present thesis and during SSI and Voronoi partitioning steps, all the points will be generated inside a unit area. Subsequently, in a CAD environment the unit control area can be scaled to the required size. The output of the SSI code consists of a list of points and their coordinates $(x,y)_n$. For a ratio of the control area size to cell size equal to ~ 16 and using properties of AL 6101-T6, pore density = 40 ppi, relative density = 9% has a cell density of 23 to 24 cells per inch. Therefore, 314 nucleus points are placed in the unit control area. For $n = 314$ cells and a unit square area ($A = 1$), the distance for a regular arrangement of points is equal to $r = 6.064 \times 10^{-2}$ units. Due to the fact that the main objective of the present research is to understand the influence of the regularity parameter (δ) over the mechanical response of random Voronoi honeycombs, geometries with different regularities in the range of 0 to 1 are generated. Specifically, values of $\delta = \{0, 0.5, 0.7, 0.8, 1\}$ have been investigated. The corresponding values for the inhibition distance to be used as input in the SSI algorithm are listed in Table 3.1. The effect of the variation of δ over the distribution of points in a SSI process is shown in Fig. 3.3.

Regularity (δ)	Distance for a regular arrangement of points (r)	Number of nuclei (n)	Inhibition distance (s)
0	6.064×10^{-2} units	314	0 units
0.5			3.032×10^{-2} units
0.7			4.245×10^{-2} units
0.8			4.851×10^{-2} units
1			6.064×10^{-2} units

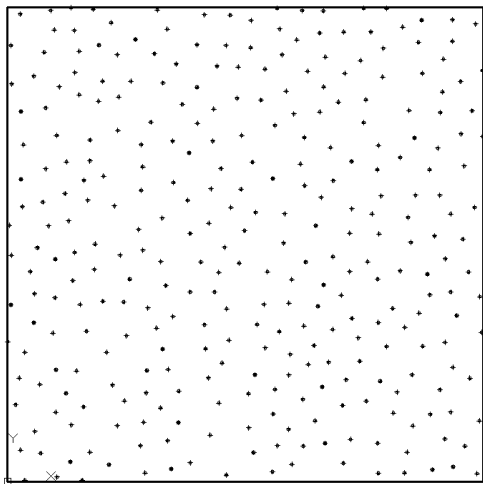
Table 3.1: Inhibition distance required to place $n = 314$ nucleus points in a unit square area with a SSI process (A , n , and s are the inputs for the SSI algorithm).



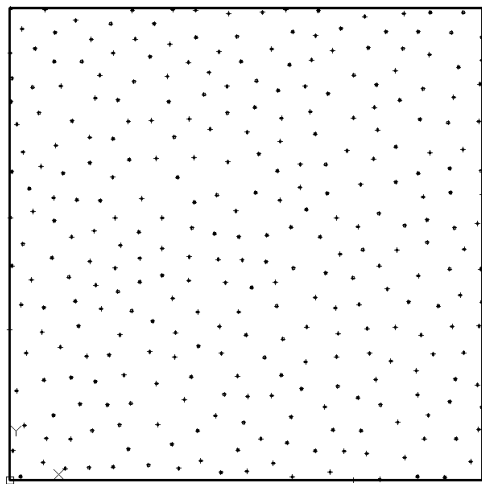
(a)



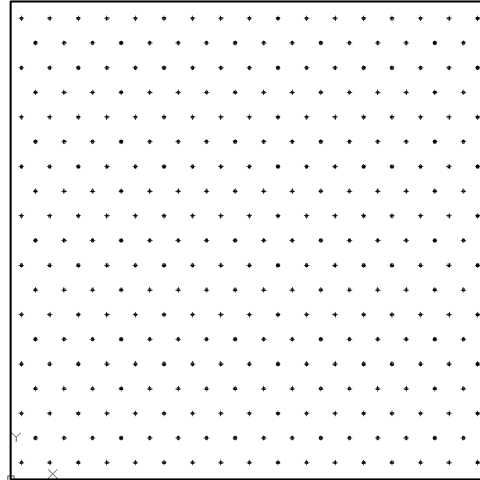
(b)



(c)



(d)



(e)

Figure 3.3: Nuclei points produced using SSI process (except $\delta = 1$) with different regularity: (a) $\delta = 0$, (b) $\delta = 0.5$, (c) $\delta = 0.7$, (d) $\delta = 0.8$, (e) $\delta = 1$.

The pattern of points in each of the above cases have been generated with the SSI algorithm except the one for $\delta = 1$. As discussed in section 2.1(d), the generation of a regular arrangement of points with a SSI process is practically improbable. For that reason, the pattern of points for $\delta = 1$ was directly generated by placing regular points with a distance $r = 6.064 \times 10^{-2}$ units from its neighbors.

(c) Voronoi partition process

MATLAB numerical computing environment is used to partition the 2D space. A Matlab code is created for this purpose. The relevant part of the code is listed in Appendix B. The code uses the function `voronoin(x,y)` of Matlab to generate a partition of the whole 2D space. The function `voronoin(x,y)` applies the Qhull algorithm developed at the Geometry Center of the University of Minnesota –Twin Cities [48] to partition the 2D space (downloadable from [49]). The output of the code contains the coordinates of the vertices delimiting each cell (or polygon in 2D) associated with a nucleus point. For instance, the output points of the Voronoi partition process of a single cell are represented in Fig. 3.4(a) as

square symbols while the nucleus point is represented by a red circular point. In fact, a set of points (nuclei points) is the input of the Voronoi partitioning algorithm and the set of points of all the vertices delimiting the future cells (or polygons in 2D) is the output (see Fig. 3.4 (a)).

(d) Convex hull of cells

Steps (a), (b), and (c) described as a flowchart in Fig. 3.2 are executed in Matlab. Then, it is necessary to migrate from Matlab to AutoCAD. Due to the fact that the locations of the vertices are available as output of the partitioning process, creation of points in AutoCAD is a straightforward procedure. However, the process needs to be repeated as many times as the number of cells created. One of the advantages of using AutoCAD is the ability to automate a determinate plotting routine by means of scripts. A script file (*.scr) is an ASCII text file that contains a set of commands for AutoCAD to execute. For instance, a script file to draw the convex hull for a set of points as the ones presented in Fig. 3.4 (b) is as follows:

```
CLAYER 1
      PLINE
          x1,y1
          x2,y2
          . .
          . .
          . .
          x7,y7
      CLOSE
```

where (x1,y1) are the coordinates of the first vertex of the cell, and (x7, y7) is the last vertex that delimits the cell. An important advantage of AutoCAD is the feasibility to use different

layers to construct different geometric entities. In fact, the command `CLAYER 1` will create the lines in layer #1, so that each cell can be easily manipulated in the future as needed.

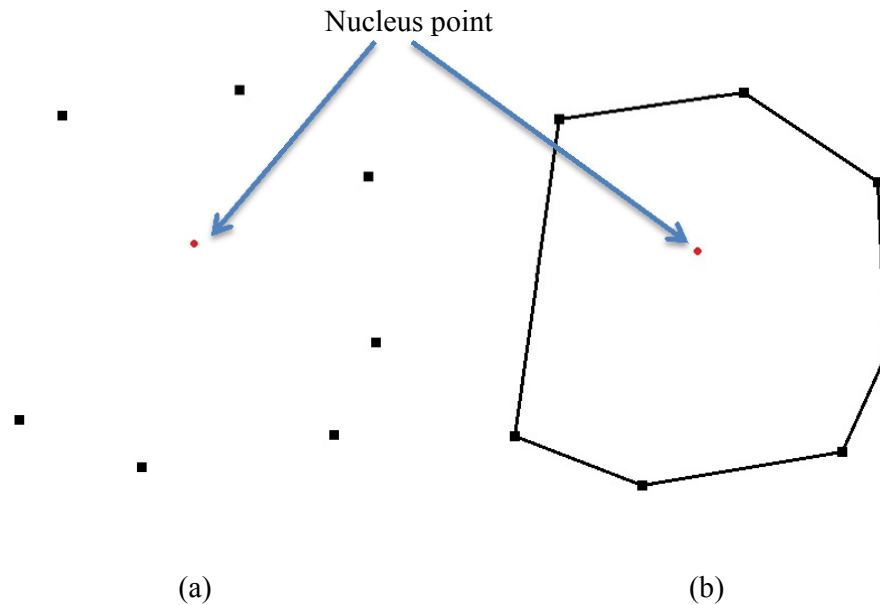


Figure 3.4: Partitioning of space and construction of a cell. (a) Output of the Voronoi partition process algorithm (solid squares), (b) Convex hull for the solid squares.

The assembly of the entire cell structure will generate a Voronoi honeycomb with a double line in each of the polygons ligament. The command `OVERKILL` of AutoCAD will solve this problem by eliminating multiple lines connecting two points. Moreover, some cells located on the border of the control area will have an unbounded limit. An intersection with the control area will turn them into bounded cells. Figure 3.5 presents the Voronoi honeycomb geometries for $\delta = \{0, 0.5, 0.7, 0.8, 1\}$ along with their pattern of points.

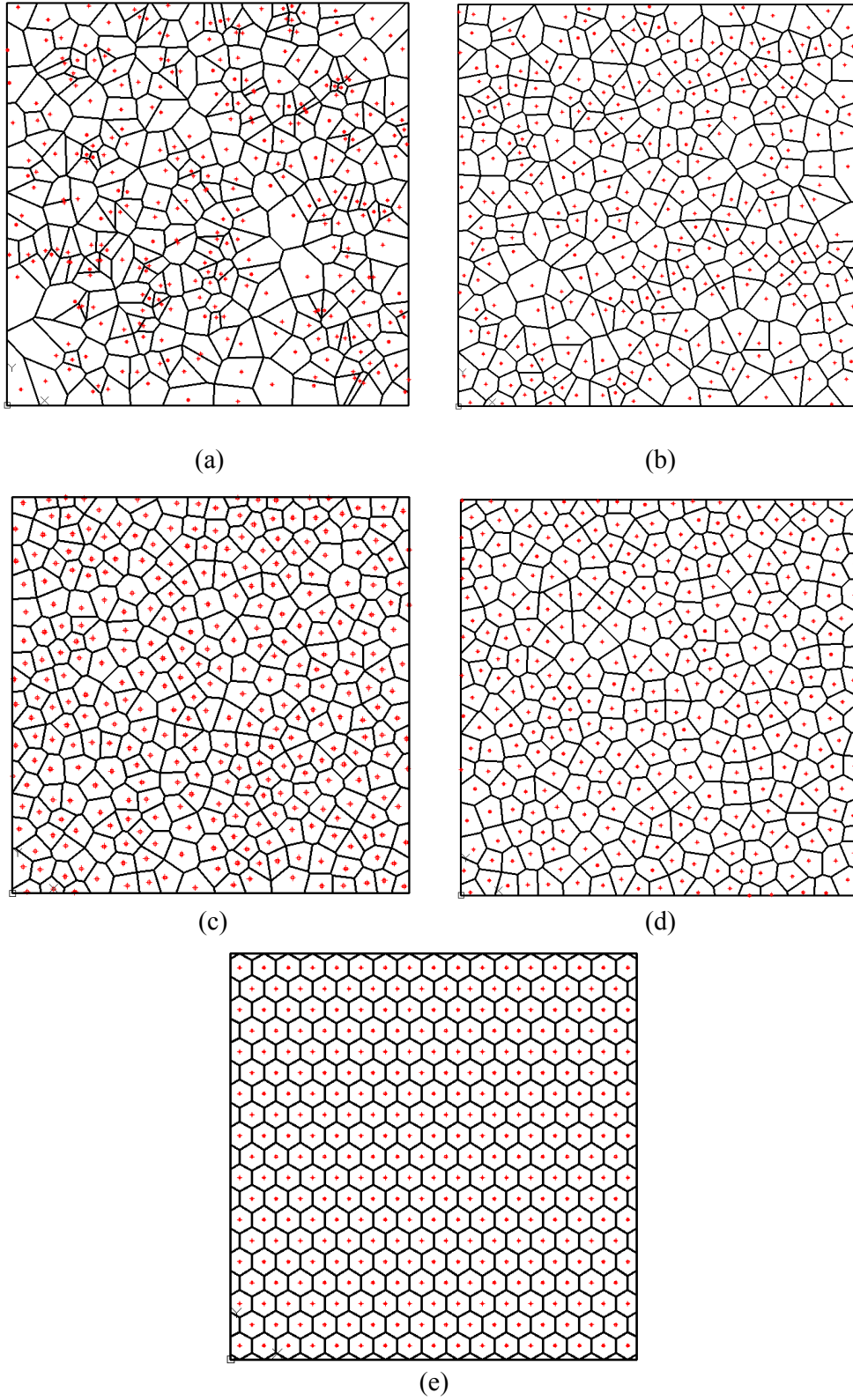


Figure 3.5: Voronoi honeycombs for: (a) $\delta = 0$, (b) $\delta = 0.5$, (c) $\delta = 0.7$, (d) $\delta = 0.8$,
(e) $\delta = 1$.

An analysis of the geometries generated by the Voronoi partitioning for different levels of regularities presented in Fig. 3.5 leads to some observations. First, the cell size distribution varies with the regularity parameter. In the case of a regular distribution of points ($\delta = 1$) all the cells have the same area, so there is no difference in the size between cells. However, reducing the degree of regularity increases the differences between cell sizes. The most dramatic case is the Voronoi geometry generated from a complete random distribution ($\delta = 0$) of nuclei. In this case, the largest cell is almost 30 times the area of the smallest one. According to Gibson [50], differences between of cell sizes is not related with anisotropy. For that reason, at the macroscopic level a foam generated with a regularity of $\delta = 0$ can still be considered isotropic. Second, the degree of regularity has an important influence on the number of faces cells can have. While the probability of finding cells with six sides ($F = 6$) in a regular 2D Voronoi honeycomb is equal to 1, irregular Voronoi honeycombs have less probability of having cells with six sides. However, a six sided polygon is still the most probable polygon that can be found in an irregular 2D geometry, but as regularity level decrease there is an increase in the differences between polygons. From only hexagons in case of $\delta = 1$ to polygons with up to nine faces for case of $\delta = 0$. For instance, the probability of finding cells with F faces for the geometries presented in Fig. 3.5 has been calculated and presented in Fig. 3.6. The trivial situation for $\delta = 1$ is not presented in Fig. 3.6. By examining Fig. 3.6 it is clear that spread around $F = 6$ increases with irregularity. Furthermore, six sided polygons are not only the most probable polygons in a 2D Voronoi honeycomb generated in the present work, but symmetry of the probability distributions suggest that the average number of faces per cell is also 6 as required by the Euler's law (see [50]).

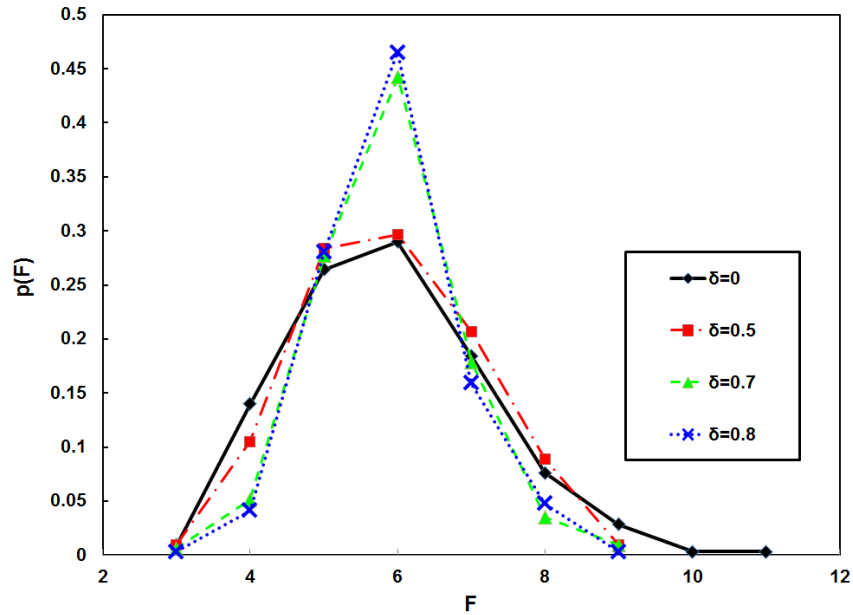


Figure 3.6: Probability $p(F)$ of finding cells with F faces with different levels of regularity.

The implication is that the geometries generated are indeed capturing the majority of characteristics observed in real foams giving a high degree of confidence in the method of generating virtual foams. However, the effect of surface tension which is also an important factor that influences geometry of foams still needs to be captured.

3.2. Geometric construction of 2D foam-filled Voronoi honeycombs

In the last section, the procedure for constructing 2D irregular dry foams has been explained. Dry foams are quite useful in simulating metal foams because the geometries can be exported directly to a finite element (FE) software as wire features (lines or 1D elements) without a particular thickness associated with lines. Essentially, the ligaments are simulated with beam elements and information about thickness and cross sectional shape is automatically created in the FE software as part of the beam option. However, the present study is also interested in the simulation of metal foams in the context of IPC configurations. Consequently, the two phases that will interact during simulations need to be created. The

approach developed in the present study is to simulate the two phases by means of 2D continuum elements. For that reason, the full two dimensional space needs to be subdivided in two regions. One region will be used to represent the aluminum phase and the other will represent the syntactic epoxy foam phase. In order to accomplish this task, the lines generated after the Voronoi partitioning require to be “thickened”. In the flowchart presented in Fig. 3.2, this operation is identified with the letter (e). Thickening of lines will be the final step to complete 2D wet foams and its complementary syntactic foam.

e) Thickening of lines

In order to create 2D wet foams, flowchart presented in Fig. 3.2 must be followed until level identified with the letter (d) in a similar procedure already explained and presented in section 3.1. Subsequently, lines of the Voronoi skeletal structures can be transformed into multi-lines (double lines in this case) one-by-one or automatically by means of *lisp* routines available in AutoCAD. In the present thesis, the *lisp* routine PL2ML that automatically converts lines to multi-lines has been used. The relative density of the metal foam is the parameter that defines the thickness of lines through the application of the formula presented in the introduction of this chapter. For example, the effect of varying density in a Voronoi random 2D geometry with $\delta = 0.8$ is presented in Fig. 3.7. In order to facilitate the visualization, values of relative density of $\bar{\rho} = \{45\%, 25\%, 9\%, 3\%\}$ have been chosen. However, the open cell aluminum foam is usually fabricated in the range of 3% to 12%. For that reason, for each one of the 2D geometries created in section 3.1 ($\delta = \{0, 0.5, 0.7, 0.8, 1\}$), a thickening process representing values of relative density of $\bar{\rho} = 9\%$ is used. As a result, a total of 5 configurations representing 2D foam-filled Voronoi honeycombs are generated and used for simulation in the future chapters. The final objective is to understand the influence of regularity on the compression response of 2D foam-filled Voronoi honeycombs by means of FE simulations.

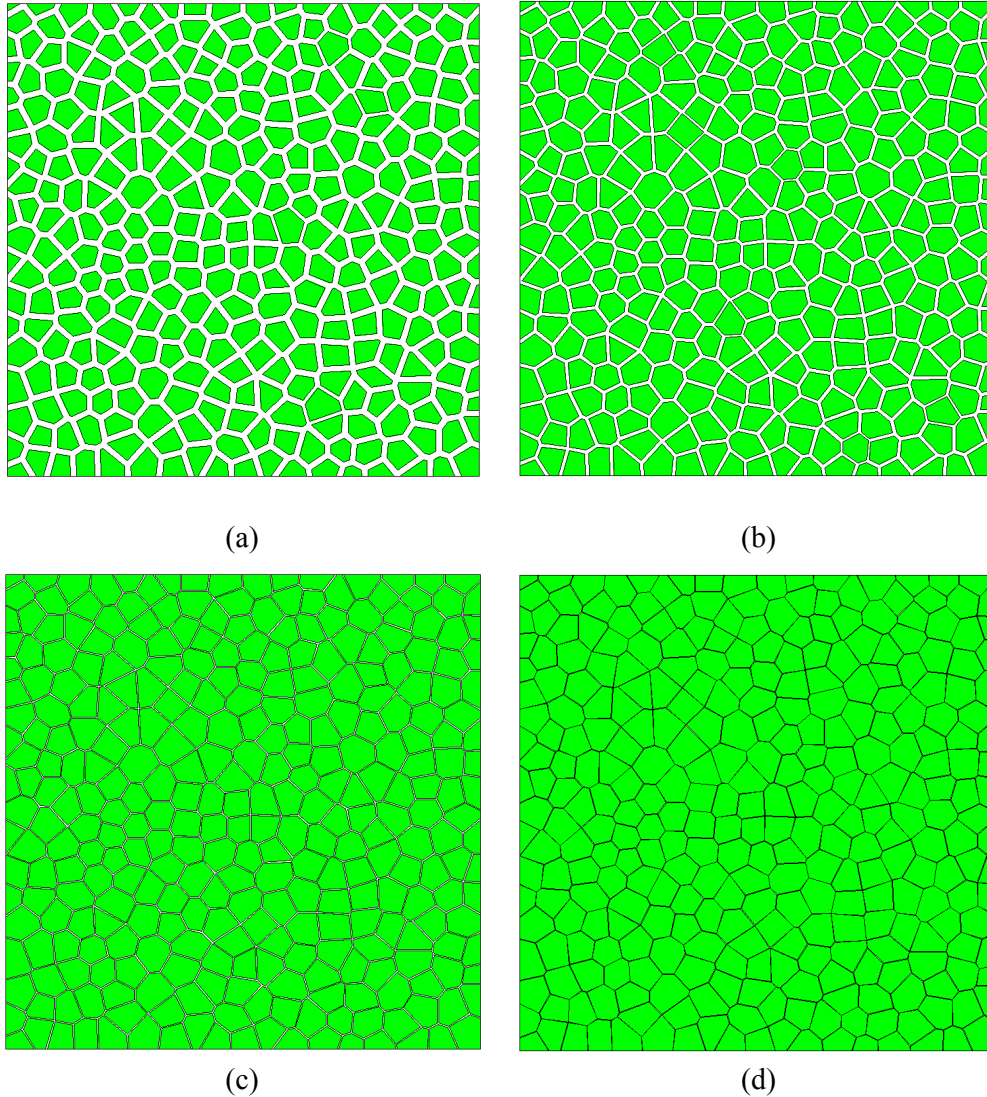


Figure 3.7: Effect of varying relative density in 2D foams for $\delta = 0.8$. (a) $\bar{\rho} = 45\%$, (b) $\bar{\rho} = 25\%$, (c) $\bar{\rho} = 9\%$, (d) $\bar{\rho} = 3\%$.

3.3. Geometric construction of 3D open cell foams

Concepts behind the construction of 3D foams based on Voronoi approach do not vary from the 2D counterpart. However, the procedure in 3D certainly requires some modifications detailed in the present section. Similar to 2D cases, the flowchart presented in Fig. 3.2 schematically represents the five steps required to generate 3D foams and the software packages required to execute them. The designer can either follow the left side of

the flowchart presented in Fig. 3.2 in order to generate irregular configurations, or can follow the right side approach in order to generate highly regular configurations. It is of particular interest to generate highly regular configurations of foams in 3D in order to avoid small ligaments. Due to the fact that lines will be represented by beam elements in FE simulations, small elements that are not slender enough cannot fully capture the beam-like behavior. This can be avoided in a 2D geometry by eliminating small elements and merging ligaments connected to the small elements into a single point. This procedure has been shown not to affect simulations (see for instance [15, 28]). However, the process of identifying and eliminating small elements is more challenging in 3D. Nevertheless, the number of small elements reduces with regularity. Indeed, in the most extreme case of $\delta = 1$ all the ligaments have the same length; differences between lengths increases as regularity decreases. For that reason, the probability of having small ligaments is reduced for geometries with higher level of regularity.

a) Creation of points in regular positions

In section 2.1(f), the formula for calculating the distance between points in a regular arrangement of points in a 3D space was introduced. This distance depends on the control volume (V) and the number of nuclei (n). Similar to the 2D case, the nucleus points can be generated in a control volume equal to 1 ($V=1$) and scaled to the required size in a CAD environment. The number of regular cells to be generated depends on the pore density of the foam to be simulated; in the present thesis it is 40 ppi. According to the manufacturer, on average 24 cells per inch exist in ERG Aluminum foam. In order to keep the number of cells manageable, the ratio of foam size to cell size corresponds to ~ 6 [45]. For the case of a regular arrangement of points six tetrakaidecahedron cells are generated along the border of a unit cube. In order to calculate the number of nuclei required for generating six tetrakaidecahedron cells along the border of a unit cube, the following analysis is needed.

The creation of a single tetrakaidecahedron cell inside a unit cube requires nine nuclei in a body centered arrangement as shown in Fig. 3.8. Although the nine nuclei have divided the space into nine regions, the unbounded regions are not useful for our simulations and are not taken into account. From analyzing Fig. 3.8, it is clear that the number of nuclei (n) required to generate (l) Tetrakaidecahedron cells along the border of a unit cube can be calculated with the formula,

$$n = (l + 1)^3 + l^3$$

In the current case $l = 6$, and hence the number of nuclei required is equal to $n = 559$.

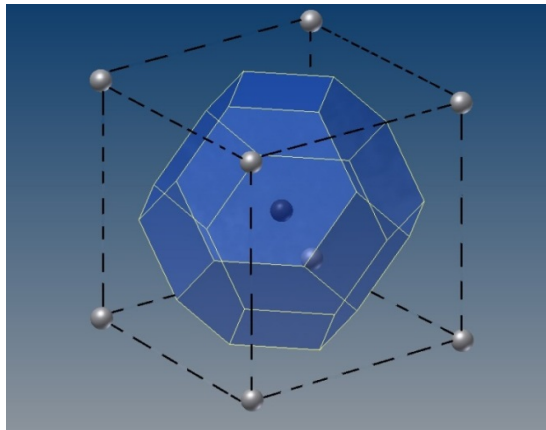


Figure 3.8: Nuclei points to generate one tetrakaidecahedron cell in a unit cube.

Knowing n and V , the distance (r) among the nuclei can be calculated with the formula detailed in section 2.1(f). Nuclei can be easily generated starting in one corner of a unit cube and adding l times the distance r to form a vector (L). The coordinates of the nuclei for a regular arrangement of points in 3D can be generated by performing all the possible permutations of elements of the vector (L), taken three at a time repeatedly. A Matlab code has been created for this purpose. The relevant part of the code is listed in Appendix B. The final result is a regular arrangement of n points inside a cube as the one presented in Fig. 2.9(a).

b) *Perturbation process*

After n nuclei have been regularly generated inside a cube of volume V , a random perturbation of magnitude (h) needs to be introduced in their locations. The Matlab function `rand` generates pseudorandom numbers between 0 and 1, so the code `h*(2*rand-1)` will generate random numbers in the range $[-h, h]$ that can be added to each coordinate of a regular arrangement of points. This addition will generate a perturbation in the point locations characterized by h . The complete Matlab code is presented in Appendix B. The level of irregularity introduced will be directly related with the value h . Due to the fact that each of the nuclei will move to a new location inside a cube of side $2h$, the minimum possible separation between two nuclei can be calculated with the formula,

$$s = r - 2\sqrt{3} h$$

Thus, the regularity, as defined in section 2.1(f), is,

$$\delta = 1 - 2\sqrt{3} \frac{h}{r}$$

Hence, for a given value of r , h can be calculated for the required level of regularity. In this thesis, levels of regularity of $\delta = \{1, 0.95, 0.8\}$ have been chosen in order to generate highly regular geometries avoiding generation of short ligaments after the Voronoi partitioning process. The patterns of points for $\delta = \{1, 0.95, 0.8\}$ that will be used are shown in Fig. 3.9.

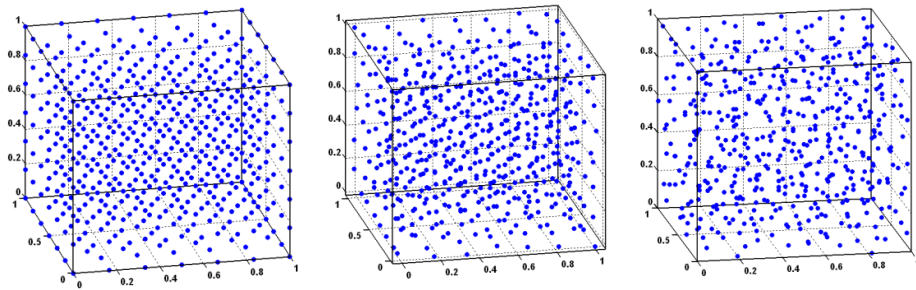


Figure 3.9: Point patterns for, $n= 559$ and (a) $\delta = 1$, (b) $\delta = 0.95$, (c) $\delta = 0.8$.

c) 3D Voronoi partition

The process of creating Voronoi partitions for points in 3D does not conceptually differ from 2D. The only difference is that the input and output points of the script to generate a 3D Voronoi partition will have a third coordinate. As in 2D, the numerical computing environment Matlab will be used to partition the 3D space (listed in Appendix B). The output of the code contains the coordinates of the vertices that delimit each cell (or polyhedron in 3D) associated with a nucleus point (referred to as the delimiting points to distinguish them from nuclei). For instance, the output points of the Voronoi partitioning process of a single cell are represented in Fig. 3.10(a) as solid square symbols. In the particular example presented in Fig. 3.10(a), for one single nucleus point, 22 points which delimit the cell from its neighbors have been generated. For instance, the 559 nuclei for $\delta = 0.8$ shown in Fig. 3.9(c) have resulted in a cloud of 12246 delimiting points after performing Voronoi partitioning. Furthermore, at this step, it is straightforward to identify an unbounded cell. Theoretically, unbounded cells have one of their delimiting points located at infinity. In reality, the unbounded cells can be identified due to the fact that one of their delimiting points is extremely far away when compared to the rest of the points generated. In fact, Matlab identifies the location of such a point with three coordinates described by the letters **Inf** that represents a number higher than the maximum number of the floating point representation used. Subsequently, unbounded cells can be identified and eliminated from the analysis.

d) Convex hull of cells.

Before creating convex hulls for a 3D structure, the coordinates of delimiting points of each cell have to be migrated from Matlab to AutoCAD following the same procedure described in section 3.1(d). As explained in 3.1(d), it is also important to group the points belonging to the same cell in different layers. In this manner, points can be isolated from the

full cloud of points generated after the Voronoi partitioning process (12246 points for the example presented in Fig. 3.9(c)).

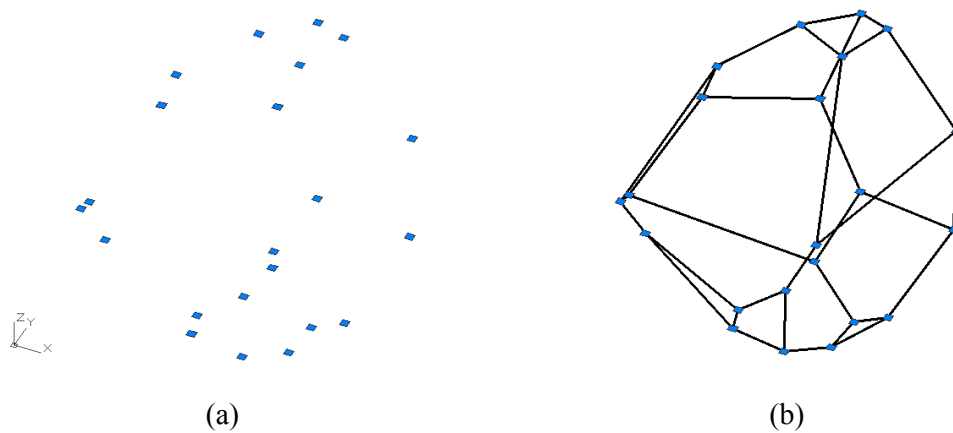
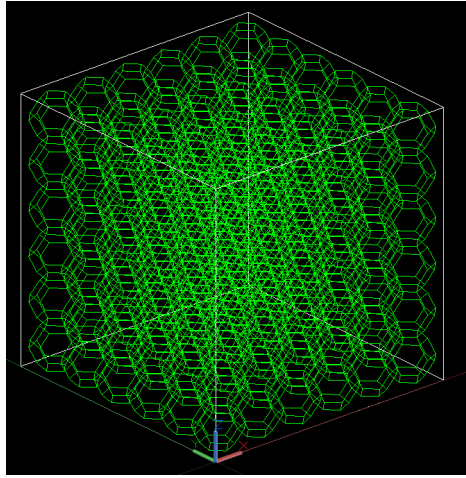
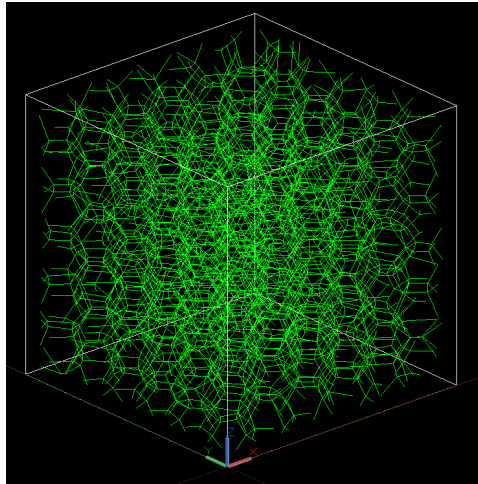


Figure 3.10: A single Voronoi cell construction in 3D: (a) output of the Voronoi partitioning algorithm (square symbols), (b) Convex hull constructed for square symbols.

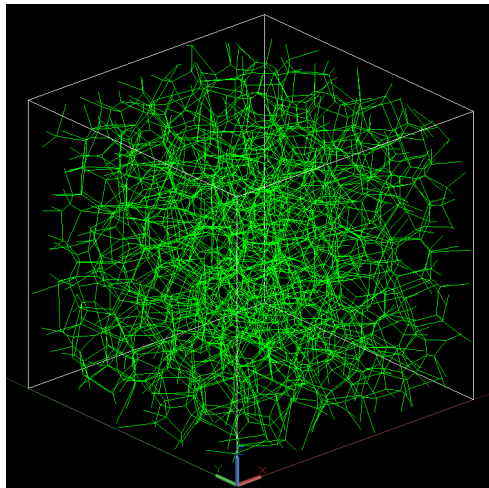
Indeed, the convex hull operation needs to be performed cell by cell, isolating each group of points and performing a convex hull operation per group. If points are drawn in different layers, the creation of convex hulls can be automated. The commercially available application for AutoCAD called Innersoft (Available from [43]) has been used for this purpose. Basically, Innersoft integrates with AutoCAD the Qhull algorithm developed at the Geometry Center of the University of Minnesota –Twin Cities [48] to generate convex hulls in 3D. (Available for a free download from [49]). Figure 3.10 illustrates the creation of a convex hull for a set of points associated with a single cell. Due to the fact that the interest of this thesis is to construct open cell structures, the ligaments rather than the planes formed after the convex hull operation will be used for the creation of the complete structure. For closed cell configurations, planes rather than ligaments should be used to assemble the full structure. The result of performing convex hull operations for each cell is a structure that still exceeds the limits of a unit cube even though unbounded cells have been eliminated.



(a)



(b)



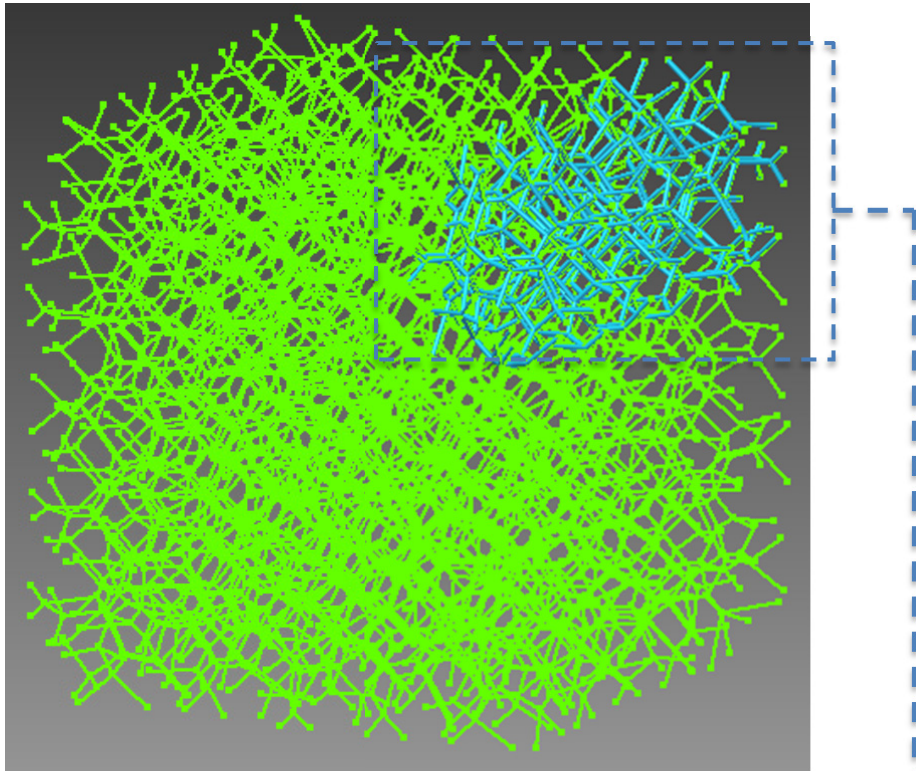
(c)

Figure 3.11: 3D dry open cell foams: (a) $\delta = 1$, (b) $\delta = 0.95$, (c) $\delta = 0.8$.

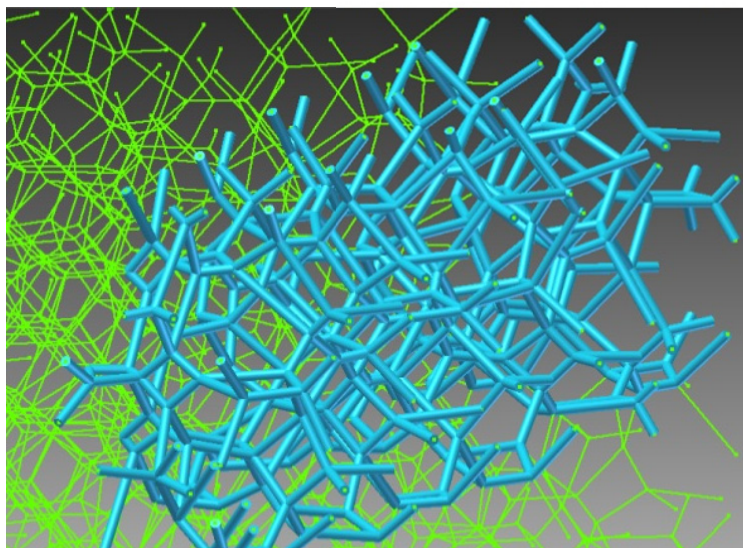
The virtual foam thus generated exceeds the limits of a unit cube because delimiting points of cells that are close to the borders of the cube can be located far from the limits of the control volume. Nevertheless, an intersection with the cube will extract the geometry required for modeling. Figure 3.11 depicts perspective views of 3D open cell dry foams along with the control volume for point patterns presented in Fig. 3.9 ($\delta = 1, 0.95, 0.8$). For the regular arrangement of points which take into account the competitive growth as the only factor that shape foams, all the cells generated take the shape of a tetrakaidecahedron. Also, cells for $\delta = 0.95$ presented in Fig. 3.11(b) have a shape similar to a tetrakaidecahedron cell but perturbed so that all of the polyhedra have 14 faces.

3.4. Geometric construction of 3D wet foams

The construction of dry foams based on the Voronoi approach has relevance in the simulation of compression/crushing of foams in 3D. Geometries can be directly exported to a FE software package without information regarding the cross sectional shape. Essentially, ligaments forming cells can be meshed using beam elements and the information about their thickness and cross sectional shape is automatically created in the FE software as part of the beam characteristics. However, dry foams are not practical if the final objective is to produce a model using Additive Manufacturing techniques. Normally, files accepted by companies that offer 3D printing services are based on a solid feature definition (common file formats are: STL (Standard Tessellation Language), VRML2/97 (.wrl), COLLADA (.dae), X3D and OBJ.), so a cross sectional shape associated with each line is required. The process of creating a solid strut having a line and cross sectional shape is normally generated through a ‘extrude’ operation in which a section is essentially swept along a path defined by the line. This approach is straightforward when only a few lines have to be handled. However, such an operation will be time consuming in case of complex 3D geometric assemblies such as the ones shown in Fig. 3.11.



(a)



(b)

Figure 3.12: Thickening process for generation of 3D wet foams: (a) dry foam presented in Fig. 3.11(b) over which a “thickening” is performed at one corner region, (b) detail.

In the present thesis, a different approach has been adopted. By means of the frame generator tool available in Autodesk Inventor, solid struts with a circular cross section are generated automatically simply by selecting the skeletal part on which the frames will be inserted. Hence, the cross sectional shape can vary within the options of frame profiles that are available in the frame generator. For example, Fig. 3.12 illustrates the result of inserting circular frames in a region of a skeleton part. Specifically the foam presented in Fig. 3.12 corresponds to the dry foam displayed in Fig. 3.11(b). A detail over the corner where the thickening process has been performed is presented in Fig. 3.12(b). Completing the process over the whole structure generates a foam with solid struts that can be manufactured with Additive Manufacturing (AM) techniques. In AM techniques, a part conceived and generated in a Computer Aided Design (CAD) program can be directly created without the necessity of elaborate production process or production tools [51]. In AM processes thin layers of a specific material are added one at a time guided by the computer design emulating a growth process. Hence, the creation of complex parts does not have the constraints imposed by the traditional production processes. Additive Manufacturing processes have been commonly used for the creation of prototypes in aerospace, automobile and bioengineering fields. However, the rapid reduction in the cost of 3D printers, the increases of computer capacity and the creation of new techniques and new materials have made Additive Manufacturing applicable not only for rapid prototyping but for manufacturing itself. Hence, the process presented in the present chapter along with an Additive Manufacturing technique is proposed as a procedure for the creation of the Voronoi foams. For example, Fig. 3.13 shows a foam with 97 cells, relative density $\bar{\rho} = 9\%$, regularity $\delta = 0.95$ with circular cross sectional ligaments created in a 3D printer based on a Fused Deposition Modeling (FDM). In a FDM process, a thermo-plastic polymer is melted in an injection head and thin layers are deposited sequentially. In the 3D printer available at Auburn University, elements with a dimension as

small as 0.04 inches with a tolerance of ± 0.001 can be created. However, successful efforts to print micro/nanostructures using laser lithography has been recently reported [52]. In the example shown in Fig. 3.13, the deposition process is numerically controlled based on the CAD design. The thermo-plastic polymer used for the foam presented in Fig. 3.13 is Acrylonitrile-Butadiene-Styrene (ABS).

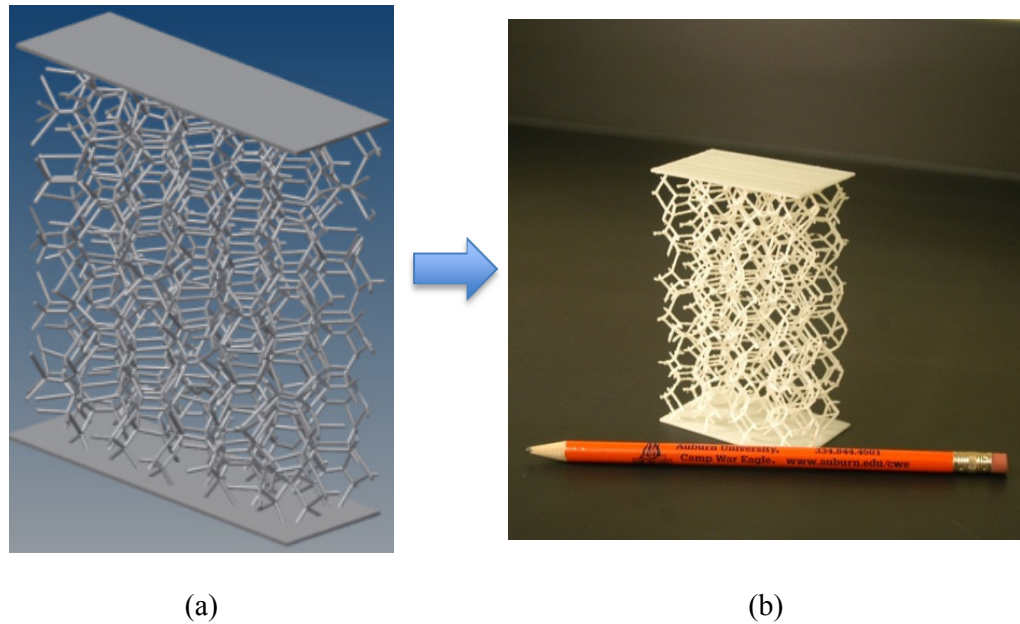


Figure 3.13: Additive manufacturing: (a) CAD model of a foam with 97 cells, $\bar{\rho} = 9\%$ and $\delta = 0.95$ (b) physical model after a Fused Deposition Modeling process with ABS.

Voronoi honeycombs can also be produced with Additive Manufacturing methods. For example, Fig 3.14 shows a Voronoi honeycomb with $\bar{\rho} = 9\%$ and $\delta = 0.95$ produced with a Polyjet Technology in VeroWhitePlus® material. In a Polyjet Technology, a thin layer (as thin as $1/1000^{\text{th}}$) photopolymer in liquid state is injected over a build tray immediately followed by a UV lamp that cures the photopolymer. The build tray moves down and the process is repeated numerically controlled by a computer according to a CAD model.

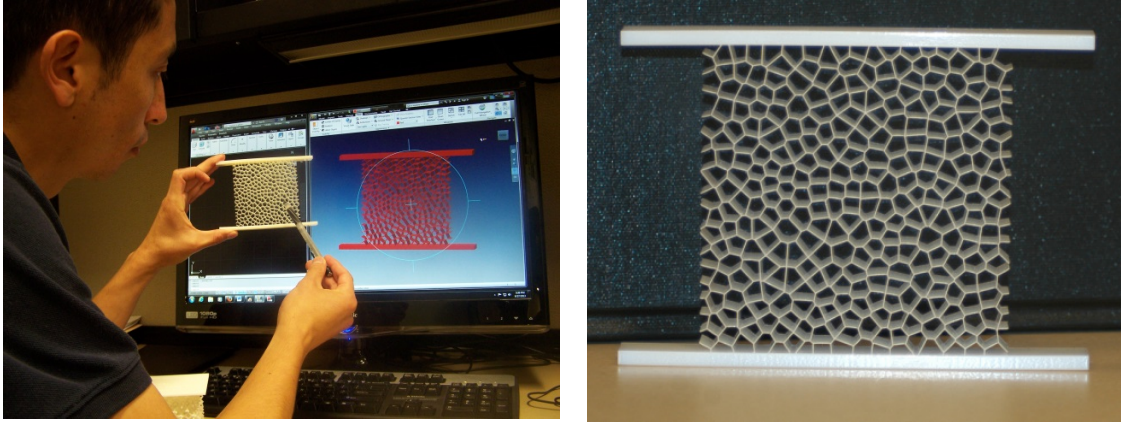


Figure 3.14: Voronoi honeycomb with $\bar{\rho} = 9\%$ and $\delta = 0.95$ produced with a Polyjet Technology in VeroWhitePlus® material.

The advantage of the proposed method over the methods commonly applied for foam production is the capacity to control the final morphology of the foam. In the currently available techniques of foam production, manufacturers commonly control the initial conditions of the processes and have limited control over the final morphology of the foam. Normally, the relative density, size of the cells and base material are the parameter that can be controlled with common foam production processes. However, regularity and cross sectional shape can also be defined with the proposed method. Essentially, controlling the pattern of points gives a direct control over the final shape of the Voronoi foam. Thus, Voronoi foams can be created with the three types of pattern of points presented in Fig. 2.7. For instance, a clustered pattern of point can be used to create functionally graded foams where the size of the cells and regularity vary from region to region within a foam structure. The shape of the computationally generated foams can also be controlled in a macroscopic context. For example, varying the approach followed in this work, volume controls other than a cube can be used for the creation of the pattern of points in order to control the macroscopic shape of the foam. Alternatively, a foam with a different macroscopic shape can be extracted

from the geometries already created with a subtract Boolean operation in Autodesk Inventor. For instance, Fig. 3.15 shows a rendering of a foam extracted from a structure with a relative density $\bar{\rho} = 9\%$ and regularity $\delta = 0.95$ with a spherical macroscopic shape.

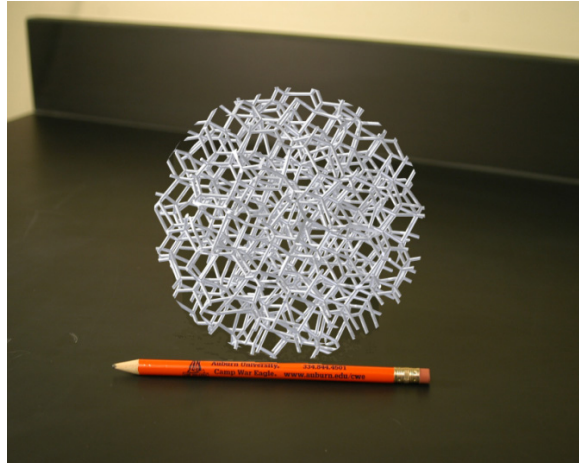


Figure 3.14: Rendering of a foam of $\bar{\rho} = 9\%$ and $\delta = 0.95$ with a spherical macroscopic shape.

CHAPTER 4

FINITE ELEMENT MODELING OF VORONOI HONEYCOMBS

Modeling, simulation and compression response of aluminum honeycombs (2D) generated using Voronoi diagrams are described in this chapter. Typically, mechanical response of Voronoi honeycombs is analyzed for geometries with a fixed regularity parameter or without any discussion about the regularity parameter. For instance, Ajdari et al., [53] have studied mechanical properties of functionally graded 2D cellular structures although level of randomness used in their study has not been identified. Also, Takoğlu et al., [16] have studied mechanical response of Voronoi honeycombs with randomness level of 0.7 whereas Mangipudi et al., [54] used 0.9. The main reason for this differences is possibly that there is not control over the level of randomness of foams with the current foam production processes. Consequently, researchers focus their efforts on modeling random foams with a regularity parameter as close as possible to the real foams. However, current advances in the field of Additive Manufacturing (3D printing, rapid prototyping) have made it possible to control the level of randomness during foam construction. For that reason, the main objective of this chapter is to study the effect of randomness on the compressive response of aluminum 2D Voronoi honeycombs. Simulations are carried out for five different samples whose construction approach was described in the previous chapter. The only difference among them is the level of randomness (regularity δ). Values of $\delta = \{0, 0.5, 0.7, 0.8, \text{ and } 1\}$ have been chosen for analysis. Recall from the previous chapters that regularity of $\delta = 1$ corresponds to a regular arrangement of nucleation points. Similarly, a level of randomness of $\delta = 0$ denotes complete random distribution of the nucleation points, so a minimum restriction in the inhibition distance was not used for this case (see Fig. 4.1). The effect of varying the relative density is also analyzed in this chapter. Hence, each geometric configuration is simulated with different values of relative densities. We have limited the

relative density to an upper value of 9% due to the fact that foams with higher relative densities cannot be well represented by beam elements of constant cross section. Indeed, in foams with high relative densities the material tends to concentrate at the junctions of ligaments and hence cannot be accurately modeled with beam elements with a constant cross section [20]. Such an idealization is acceptable for relative densities below 10% [55]. Additionally, open cell aluminum foams manufactured by, say ERG, are normally in the range of 3% to 12%. Hence, values of relative density of $\bar{\rho} = \{9\%, 7\%, 5\%, 3\%\}$ have been selected for analysis. Simulations focus on open-cell aluminum foams made of AL 6101-T6 and pore density = 40 ppi. (The open-cell aluminum foam described above is commercially manufactured by ERG Inc.) Physical properties of Aluminum 6101-T6 are described in the Appendix A. (Information provided by The Aluminum Association, Inc. from Aluminum Standards and Data 2000 and/or International Alloy Designations and Chemical Composition Limits for Wrought Aluminum and Wrought Aluminum Alloys (Revised 2001)).

The numerical simulations are carried out using Abaqus® structural analysis software v.6.10-2. The SI units are used as input data throughout this thesis. Abaqus® bases its calculations on finite element method, which has been successfully used by many researches to analyze mechanical response of foams and interpenetrating phase composites (see for instance [19, 28, 30, 56]). In the first part of the chapter (4.1), the approach followed during modeling is detailed in a chronological order (following Abaqus/CAE model tree). Subsequently, the effect of loading direction is studied in section 4.2. Section 4.3 deals with analysis of the influence of regularity in 2D Voronoi honeycomb response. Finally, the effect of relative density is studied in section 4.4.

4.1. Finite element modeling of Voronoi honeycombs

In the pre-processing stage, the geometry for each of the Voronoi honeycombs was developed by applying the method described in section 3.1. Zhu et al., [17] determined that

the minimum number of cells to maintain deviation between simulations to a minimum is 64. It is a particular interest to the present thesis to increase the number of cells in order to generate accurate results. However, the computational time limitations must also be considered in order to generate results that are manageable. In the present thesis a control area corresponding to a ratio of the control area size to cell size equal to approximately 16 has been considered as suggested by Tekoğlu et al., [16] for uniaxial compression. Hence, the control area corresponds to $n = 314$ cells. In addition, only dry configurations are required to model Voronoi honeycombs (2D). Hence, the flowchart presented in Fig. 3.2 was executed until the level identified with the letter (d). Thus, five types of dry geometries were generated with a regularity of 0, 0.5, 0.7, 0.8 and 1. Left and right lines of the area of control have been eliminated to emulate real foams in a sandwich configuration. Geometries were then imported from AutoCAD to Abaqus® through ACIS SAT (*.sat) files. The geometries are the basis for creating 2D deformable wire mesh in Abaqus®. The imported geometries into Abaqus are shown in Fig. 4.1.

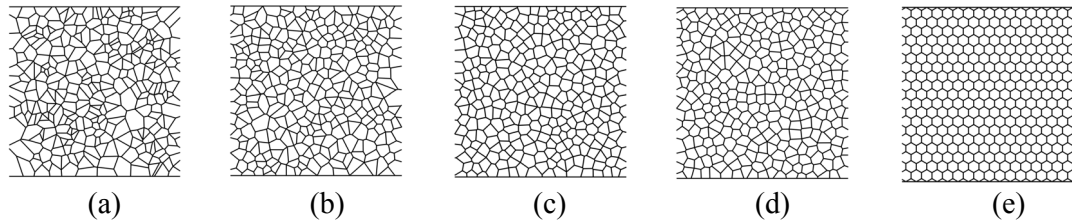


Figure 4.1: Voronoi honeycombs with: (a) $\delta = 0$, (b) $\delta = 0.5$, (c) $\delta = 0.7$, (d) $\delta = 0.8$, (e) $\delta = 1$.

Subsequently, a material model for AL-6101-T6 needs to be considered. In this work a bilinear stress-strain behavior for Aluminum 6101-T6 is used and is schematically presented in Fig. 4.2. The bilinear material model is based in properties reported in Appendix A at 25 °C and will be the model used from this point forward. As shown in Fig. 4.2, the elastic region is described by the modulus of elasticity (E) and Poisson's ratio of 68.9 GPa and 0.33, respectively.

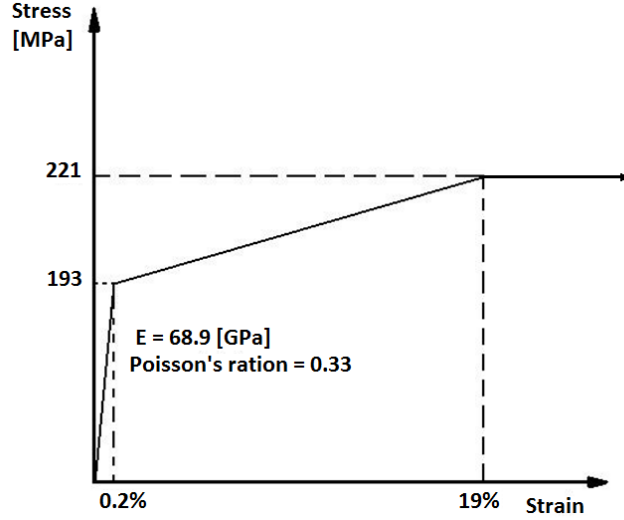


Figure 4.2: Material model for Al 6101 – T6

In order to characterize the plastic regime, Abaqus® requires strain divided into elastic and plastic regimes [57]. The relation to calculate plastic strain can be written as,

$$\varepsilon^{pl} = \varepsilon^t - \varepsilon^{el} = \varepsilon^t - \sigma/E,$$

where ε^{pl} is the true plastic strain, ε^t is the true total strain, ε^{el} is the true elastic strain, and σ is the true stress. A constant stress response is assumed by Abaqus for deformations beyond a strain of 19% (see Fig. 4.2). Next, a beam section with a circular profile is assigned for all the line features created. As explained in the previous chapters, for the sake of simplicity, cross-section of all the struts is idealized to be circular although in reality the diameter varies along the length [20]. Such idealization is acceptable for relative densities below 10% [55]. Moreover, as established by Zhu et al. [27], and utilized by other researchers ([16] [31]), the value of the strut thickness (h_i) depends on the density of the foam. Hence, in 2D it can be estimated by,

$$\bar{\rho} = \rho^*/\rho_s = \left(\frac{1}{A}\right) \sum_{i=1}^N h_i l_i$$

where $\bar{\rho}$ is the relative density of the foam, ρ^* is the density of the cellular material, ρ_s the density of the solid, N the number of struts, h_i the thickness of struts, l_i the cell wall length and A the control area. The sum of all the ligament lengths of the Voronoi honeycombs can be evaluated in AutoCAD through the transformation of lines into a single polyline. The properties of the polyline store the information of the total length. Hence, the thickness of struts (or diameter of circular sections) can be calculated. The corresponding results are presented in Table 4.1.

Relative density ($\bar{\rho}$)	Regularity (δ)	Strut thickness (h_i [m])
9%	0	5.0775×10^{-5}
	0.5	5.1092×10^{-5}
	0.7	5.2273×10^{-5}
	0.8	5.2616×10^{-5}
	1	5.0597×10^{-5}
7%	0	3.9471×10^{-5}
	0.5	3.9738×10^{-5}
	0.7	4.0653×10^{-5}
	0.8	4.0919×10^{-5}
	1	3.9357×10^{-5}
5%	0	2.8203×10^{-5}
	0.5	2.8389×10^{-5}
	0.7	2.9050×10^{-5}
	0.8	2.9231×10^{-5}
	1	2.8106×10^{-5}
3%	0	1.6922×10^{-5}
	0.5	1.7033×10^{-5}
	0.7	1.7430×10^{-5}
	0.8	1.7539×10^{-5}
	1	1.6863×10^{-5}

Table 4.1: Thickness of struts for different configurations of Voronoi honeycombs.

As observed in the Table 4.1, the variation of thickness is relatively small for a given value of relative density. The variation is essentially a consequence of length differences.

Nonlinear effects due to large deformations are activated in a general static analysis performed in ABAQUS/Standard module. Moreover, unstable nonlinear problems require an

adaptive automatic stabilization scheme [10, 57]. Values of 2×10^{-4} and 0.05 for dissipated energy fraction and ratio of stabilization energy to strain energy are used in this work ABAQUS/Standard. Furthermore, the number of attempts per increment is set to 10 and the allowable time increment is reduced to $1 \times 10^{-8} s$ for stabilizing the simulation.

The interaction among cell walls when large deformations occur plays an important role in the mechanical response of Voronoi honeycombs. If no interaction occurs between cells, interpenetration of elements is normally observed in deformed structures (see for instance [17]). In order to prevent interpenetration of nodes among cells at high strain levels, surfaces in the interior of each closed cell are created and frictionless interaction of the self-contact type is stipulated for these surfaces. No interaction has been considered for the open cells located at the right and left boundaries of the control area for geometries compressed in the x_2 direction (and top and bottom for geometries compressed in the x_1 direction). The reason is that a closed surface is necessary for creating a self-contacting type interaction. However, the exclusion of such cells does not affect the simulation because they represent only $\sim 10\%$ of the total number of cells in the control area. More importantly, the majority of the cells located on the border of the control area do not even come into inter-cell contact during simulations as will be demonstrated in section 4.2.

Special attention is required for setting the boundary conditions for the model. The imposed boundary conditions should contribute to the convergence of the simulation. For that reason, a smooth step displacement (instead of boundary forces) is applied at the top surface while lower surface is constrained from displacement in the x_2 direction. Similarly, a restriction for displacement in the x_1 direction is applied to a single point at the top and bottom surfaces.

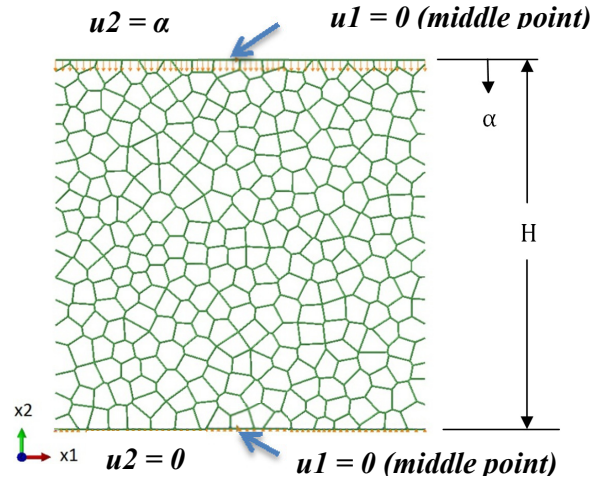


Figure 4.3: Boundary conditions for the Voronoi honeycombs simulations (example shown $\delta = 0.8$ loaded in the x_2 direction).

For maintaining symmetry during simulations, the points constrained in the x_1 direction are located in the middle of the top and bottom surfaces. For example, Fig. 4.3 illustrates the boundary conditions applied over a Voronoi honeycomb with a regularity of $\delta = 0.8$ crushed in the x_2 direction. In order to understand the directional dependency, the 2D Voronoi honeycombs are loaded in both x_2 and x_1 directions. The boundary conditions differ for the 2D Voronoi honeycombs compressed in the x_1 direction. In this case, the left side of the Voronoi honeycomb is constrained for displacements in the x_1 while translation in the x_2 direction is allowed. Further, a restriction for displacement in the x_2 direction is imposed for two points in the middle of the right and left surfaces.

Plane beam elements with three active degrees of freedom per node and a quadratic interpolation within the domain are selected for FE discretization. Beam elements are suitable for simulating geometries with one of the dimensions significantly greater than the other two [57]. The elements are identified as B22 in Abaqus® where ‘B’ stands for beam, the first ‘2’ indicates the dimensionality, and the second ‘2’ indicates the interpolation formulation (quadratic in this case). B22 elements base their formulation on Timoshenko’s beam theory, so they take into account shear deformation, which is significant in short beams subjected to large deformations. The number of elements per wall must be sufficiently small in order to

assure convergence, but sufficiently high to minimize the creation of extremely short ligaments because short ligaments cannot be accurately modeled using beam elements. Tekoğlu [58] showed that one element per edge is enough for achieving convergence in the case of elastic loading. However, this work deals with the simulation of Voronoi honeycombs in the plastic regime as well. Hence, two elements per edge are used for meshing. Further, short edges are discretized only with one element to avoid elements that are not sufficiently slender. Only elements longer than 1.5 times the thickness of the edge are tolerated. That is, edges shorter than 1.5 times the thickness are eliminated and extreme points of the element are merged into a single point [14]. The number of elements in a typical simulation is in the range of 1702 to 2058.

In the processing stage, simulations are run as a batch job in a parallel processing environment. The Samuel Ginn College of Engineering High Performance Computer Cluster (HPCC) is used for this purpose. The HPPC consist of 512 cores each with a processing capacity of ~2.80 GHz associated in four compute nodes. Each node has 16 blades with 2 central processing units per blade. The HPPC shares a memory of 1.536TB and has a storage capacity of 20.48TB. The theoretical performance calculated is approximately 5.735 teraflops.

In the post-processing stage, the reaction forces on the bottom surface of the model are added in order to get the total reaction force (F). The average stress over the Voronoi honeycomb is obtained as a ratio of the force (F) to the area of the base (see Fig. 4.3). A similar analysis is performed when the displacement is applied in the x_l direction. Next, in order to get the average strain of the sample, displacement of the top surface (α) is divided by the length of the control area (H) (see Fig. 4.3). When the average strain is calculated for geometries crushed in the x_l direction, the displacement of the right surface (α) is divided by the initial width (H). All these calculations are accomplished for every load increment in

order to get continuous curves. Detailed results for Voronoi honeycombs with $\bar{\rho} = 9\%$ are presented in section 4.2 (see Fig. 4.4 through 4.11) and a comparison of critical characteristics for different densities and regularities are presented in Fig. 4.12 through 4.18.

Validation of results have been performed by comparing simulation of Al Voronoi honeycomb with a $\bar{\rho} = 9\%$ and $\delta = 1$ loaded in the x_2 direction with analytical models. Gibson and Ashby [2] derived a formula for calculating the elastic modulus of hexagonal honeycombs ($\delta = 1$) based on simple beam theory. They estimate that the relation between elastic modulus of an hexagonal honeycomb (Voronoi honeycomb with $\delta = 1$) to the solid material is equal to,

$$\frac{E^*}{E_s} = \frac{4}{\sqrt{3}} \left(\frac{h}{l}\right)^3$$

where, E^* is the elastic modulus of the hexagonal honeycomb, E_s is the elastic modulus of the solid material, h is the thickness of the ligaments and l is the length of a ligament in the hexagon. However, Gibson and Ashby derived their formula assuming a rectangular beam cross section for each ligament. For that reason, a formula was derived using the same approach but for a circular cross in order to compare the FE results from the present work. Appendix C details the derivation of the formula,

$$\frac{E^*}{E_s} = \frac{\sqrt{3}\pi}{4} \left(\frac{h}{l}\right)^3$$

Similarly, Gibson and Ashby [2] have derived a formula for calculating the plastic-collapse strength (σ_{pcs}^*) of hexagonal honeycombs ($\delta = 1$) by equating the work done by a force applied over a hexagonal cell and the work required to produce plastic hinges at the vertices of the hexagon. They estimate that the relation between the plastic-collapse strength of the foam to the yield stress of the cell-wall material is,

$$\frac{\sigma_{pcs}^*}{\sigma_{ys}} = \frac{2}{3} \left(\frac{h}{l} \right)^2$$

where, σ_{pcs}^* is the plastic-collapse strength of the hexagonal honeycomb, σ_{ys} is the yield stress of the cell-wall material, h is the thickness of the ligaments and l is the length of a ligament in the hexagon. Again, Gibson and Ashby have derived the previous equation by assuming a rectangular shape for the cross section of the beams. The same derivation has been performed in Appendix C for the case of a circular cross section. The modified formula is,

$$\frac{\sigma_{pcs}^*}{\sigma_{ys}} = \frac{4}{9} \left(\frac{h}{l} \right)^2$$

The formulae presented by Gibson and Ashby have been validated by experiments. Accordingly, a comparison of the simulation for the Voronoi honeycomb with $\delta = 1$, $\bar{\rho} = 9\%$, loaded in the x_2 direction is presented along with the theoretical counterparts in Fig. 4.4. The figure also depicts deformed shapes of the structure at five points of interest in order to compare with the experimental results available in the literature. It is well known that the in-plane response of cellular solids under uniaxial compression produces a stress strain curve that can be divided into three regions, namely, an elastic region, a plateau region and a densification region. In the linear elastic region, elastic bending is the primary deformation mode of Voronoi honeycombs [2]. When a critical strain is reached, a drop in the slope of stress-strain curve is observed due to local buckling and plastic yielding [2]. The stress-strain curve presented in Fig. 4.4 shows that simulation is indeed capturing the general form of this response observed in cellular solids in the elastic and plateau regimes at the expected level. First, the linear elastic regime presents good agreement with the theoretical calculations presented by Gibson and Ashby [2] although it is not perfectly linear. The deformed shape in the elastic regime causes barreling of the honeycomb (see Fig. 4.4(1)). Second, when a

certain level of strain is reached, a slope change in the stress-strain curve is observed. Deformation initiates along the diagonals beginning at the corners of the control area (akin to shear band formation in solid specimens).

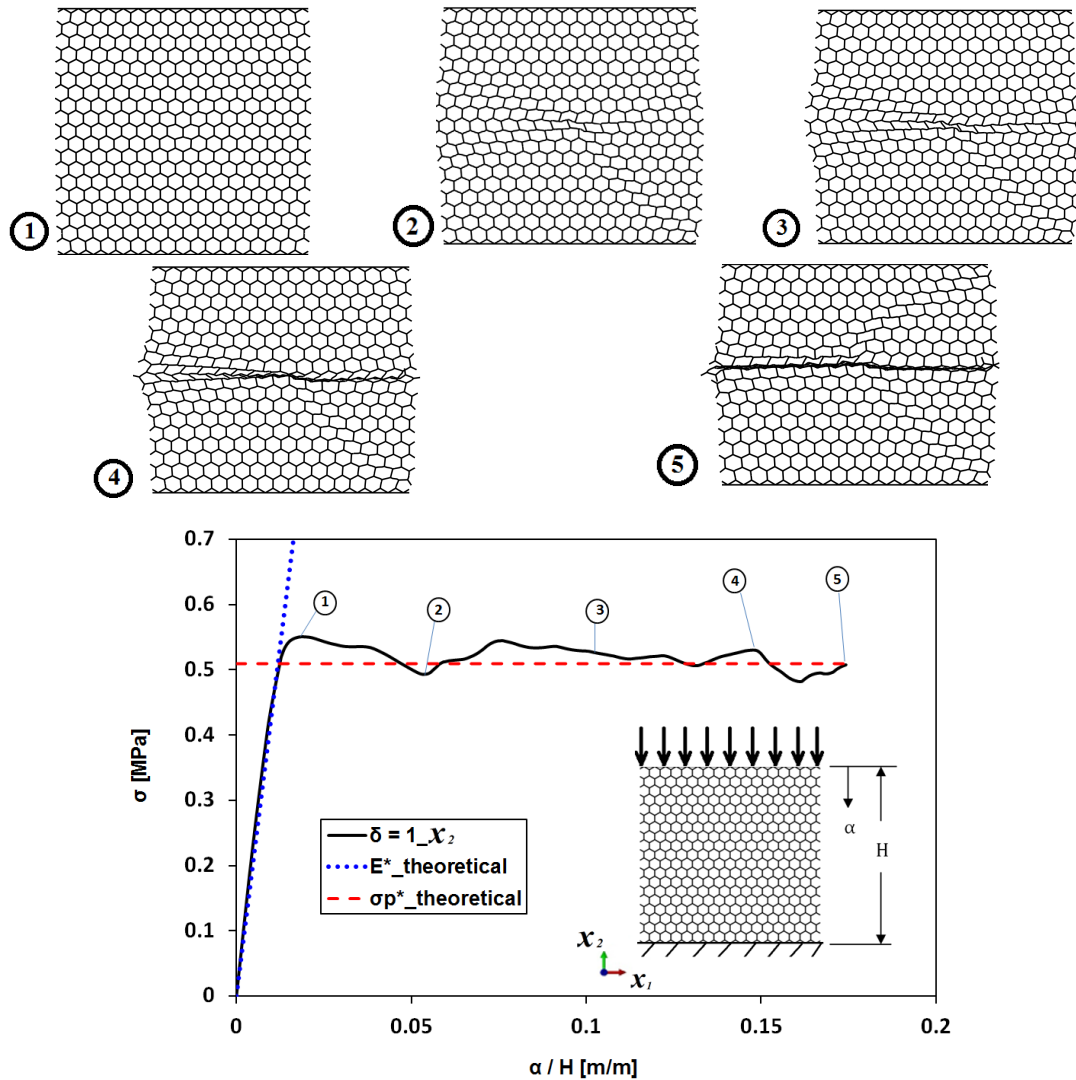


Figure 4.4: Stress-strain curves for Al Voronoi honeycomb with a $\bar{\rho} = 9\%$, $\delta = 1$ loaded in the x_2 direction.

Deformation starts to localize at the intersection of the diagonals. The first cells to collapse are located close to the center of the structure. After the first cell collapses, all the cells in the same row follow the trend until the entire row is completely closed, initiating an

oscillatory behavior in the stress-strain curve, as the process spreads to all the other cells. Hence, the plateau shows oscillations corresponding to the collapse of cells in the horizontal bands [12]. This oscillation is consistent with experimental observations and numerical simulations available in literature (see for instance [13, 18, 59]). The perturbation generated for the first collapsed row causes a disturbance and subsequent collapse of the neighboring rows. Similar analysis has been performed by other researchers for hexagonal honeycombs arriving at comparable results (see [12, 13]).

The consistency between experimental observations available in the literature and simulations presented in the present thesis, suggests that the modeling approach is able to capture the salient features of crushing of hexagonal honeycombs. Moreover, the plateau strength and elastic modulus presented in Fig. 4.4 shows a good agreement with the theoretical values calculated using Gibson and Ashby approach. Due to the fact that a hexagonal honeycomb can be considered as a special case of a Voronoi honeycomb, consistency of simulation of hexagonal honeycombs with the theory and experiments give a high degree of confidence with the approach followed in modeling the rest of regularity factors. In section 4.2, the loading direction dependency for Voronoi honeycombs with different regularities is analyzed for a constant density of $\bar{\rho} = 9\%$.

4.2. The effect of loading direction

In the present section a comparison between the compression response for Voronoi honeycombs ($\bar{\rho} = 9\%$) displacement controlled loading in the x_2 and x_1 directions is presented. Figures 4.5 through 4.9 depict the compression response in the x_2 and x_1 direction for different regularity parameters. In order to make the results more useful, the stress has been normalized by the yield stress of the solid material (σ_{ys}) and the square of the density $\bar{\rho}^2$. Hence, the formula for calculating the reduced stress $\bar{\sigma}$ is,

$$\bar{\sigma} = \frac{\sigma}{\sigma_{ys} \cdot \bar{\rho}^2}$$

$\bar{\rho}^2$ is used in the normalization due to the fact that the strength scales with $\bar{\rho}^2$ as shown in section 4.4. Additionally, the deformed models at five points of interest on the stress-strain curve are also presented. The deformed models for the points of interest are identified by a number in case of compression in the x_2 direction and by a letter for compression in the x_1 direction. Results presented in Figs. 4.5 to 4.9 show that the simulations are able to successfully capture the two initial regimes (elastic and plateau regimes) corresponding to the level of imposed deformation.

Regarding the elastic regimes in Figs. 4.5 to 4.9, all the configurations exhibit a nearly linear variation whose magnitude depends upon the level of regularity. The variation in the elastic modulus for different regularities is analyzed in section 4.3. In the present section, the focus is on the directional response of Voronoi honeycombs. Essentially, the elastic response is independent of the direction of loading. In all configurations, the elastic modulus is comparable when compressed in the x_1 and x_2 directions. This is also observed when $\delta = 1$ (see Fig. 4.9) consistent with the literature for 2D cellular solids (see [2]). Moreover, in the elastic regime, the barreling seen in case of hexagonal honeycombs is not evident for the rest of the regularities considered. A possible explanation is that random geometries do not deform uniformly in the elastic range. Furthermore, in all the configurations, a noticeable drop is seen at the onset of inelastic deformations. For the sake of analysis, the corresponding peak is identified as “plastic-collapse strength” (σ_{pcs}^*) in the present thesis to differentiate from the plateau strength (σ_{pla}^*). The plastic-collapse strength is similar for the entire regularity range (0 to 1). The small differences are attributed to the randomness of the structures. In the most extreme case, this difference is ~4.2% for $\delta = 0$ (see Fig. 4.5).

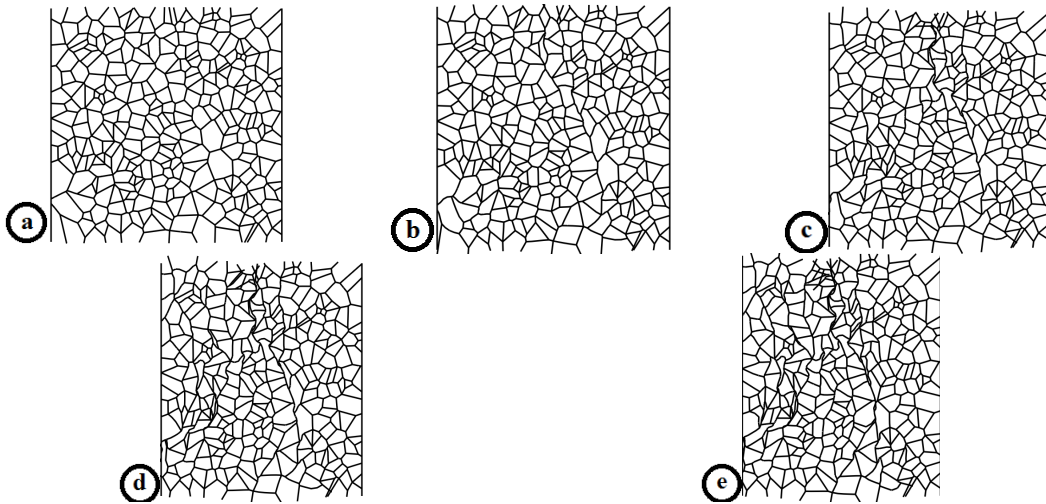
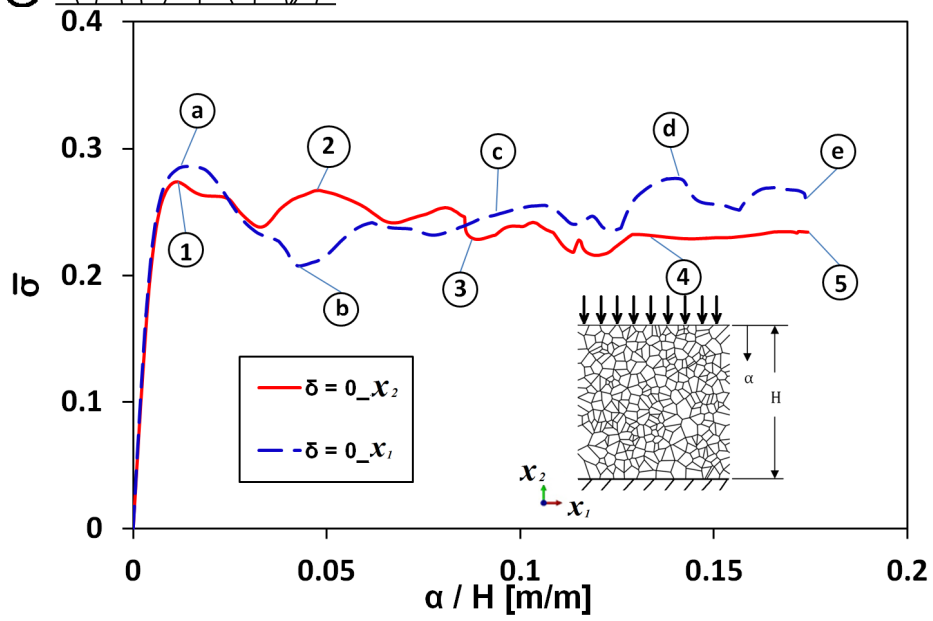
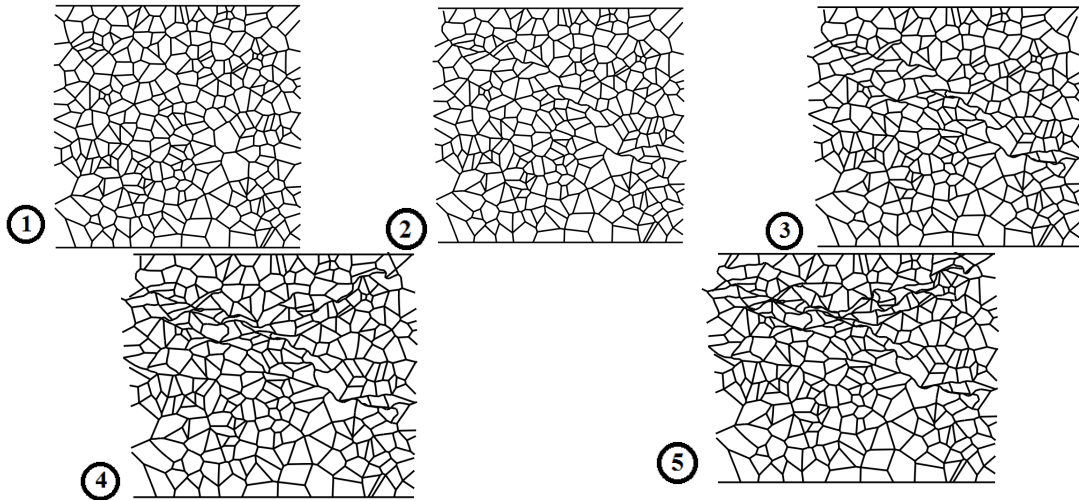


Figure 4.5: Stress-Strain curves for a 9% Al Voronoi honeycomb of 40 ppi and $\delta = 0$.

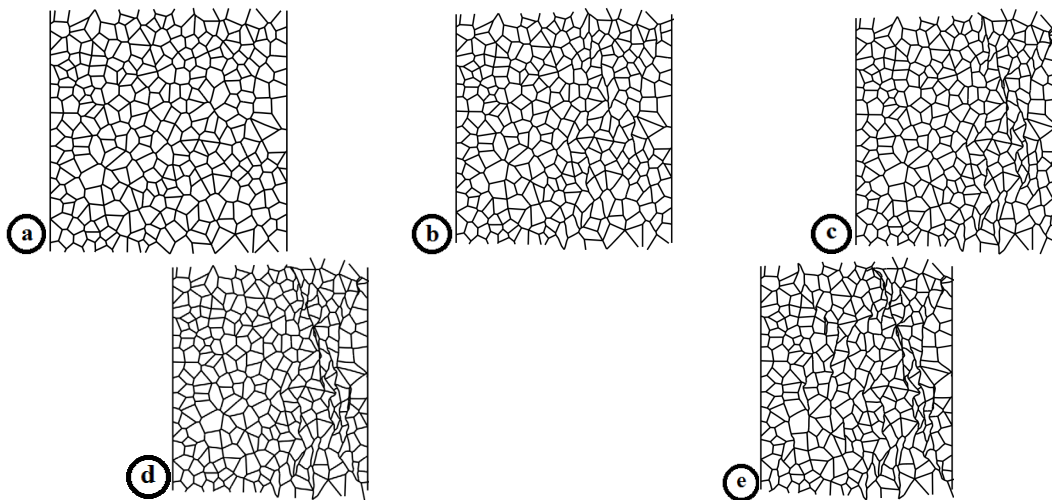
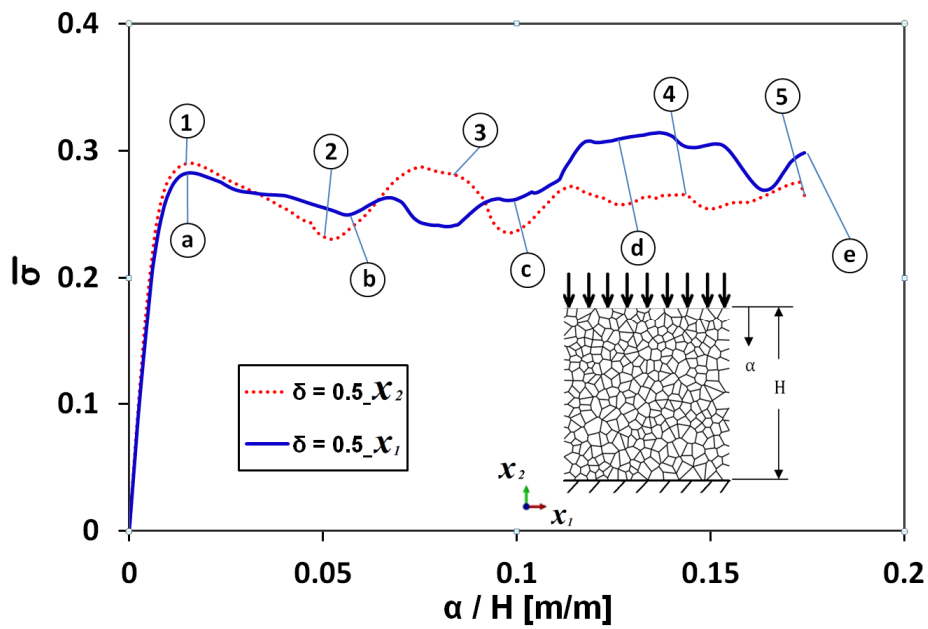
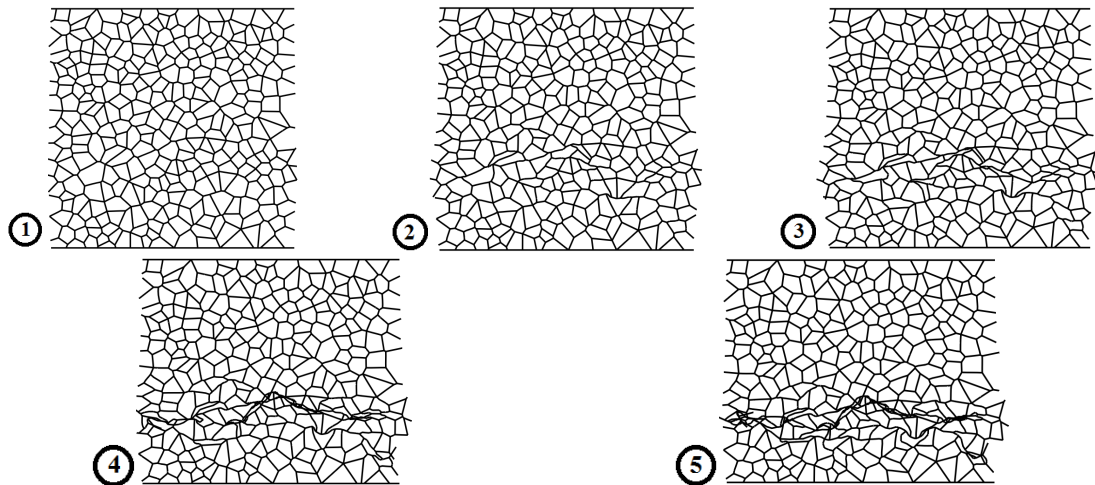


Figure 4.6: Stress-Strain curves for a 9% AlVoronoi honeycomb of 40 ppi and $\delta = 0.5$.

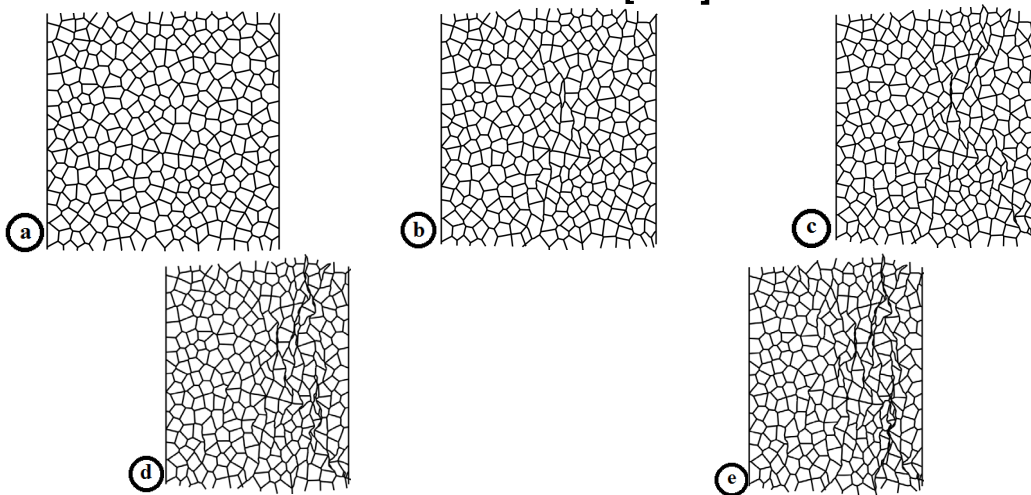
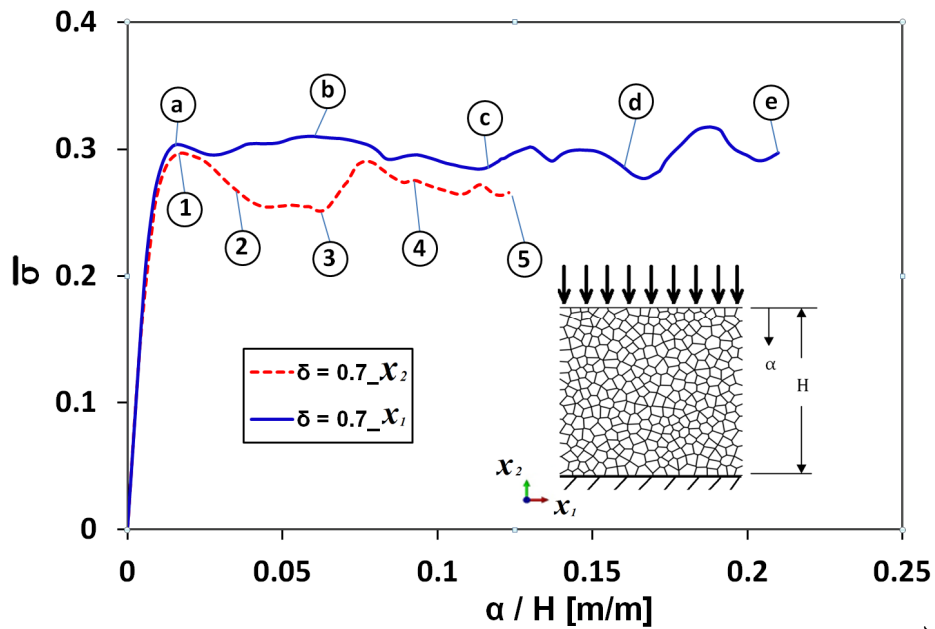
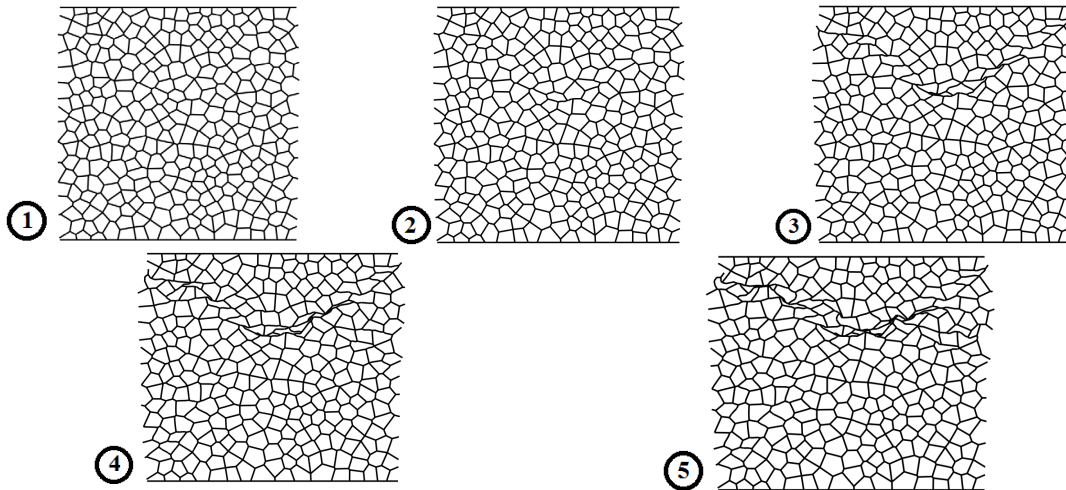


Figure 4.7: Stress-Strain curves for a 9% Al Voronoi honeycomb of 40 ppi and $\delta = 0.7$.

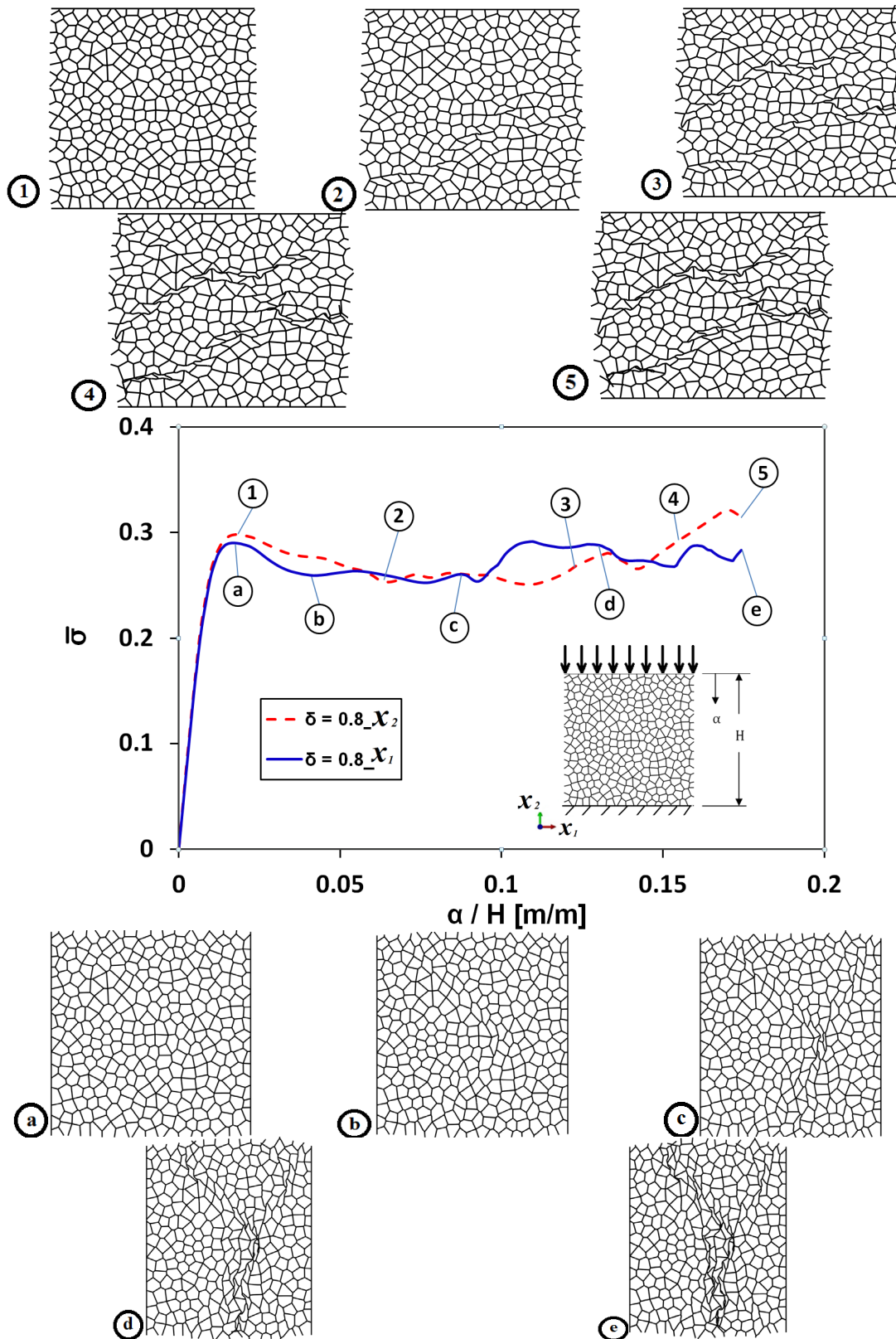


Figure 4.8: Stress-Strain curves for a 9% Al Voronoi honeycomb of 40 ppi and $\delta = 0.8$.

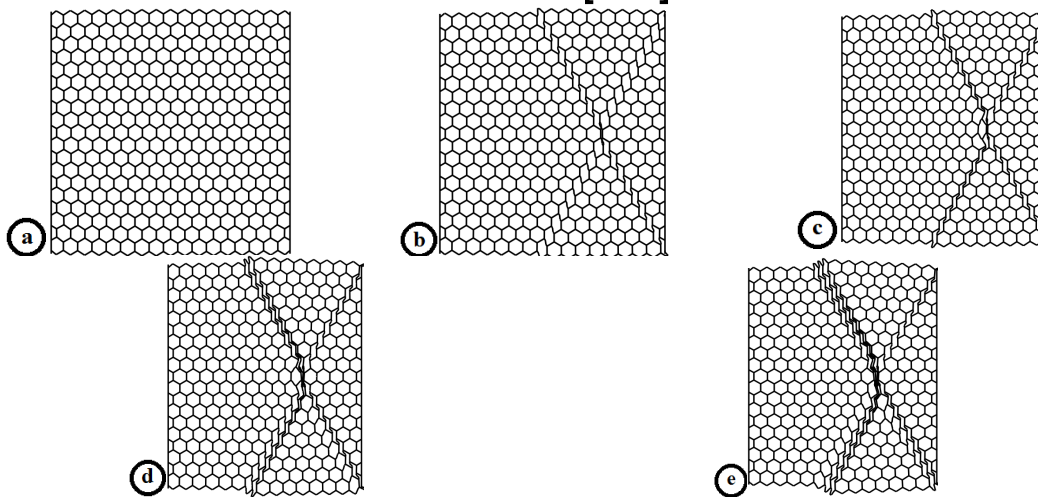
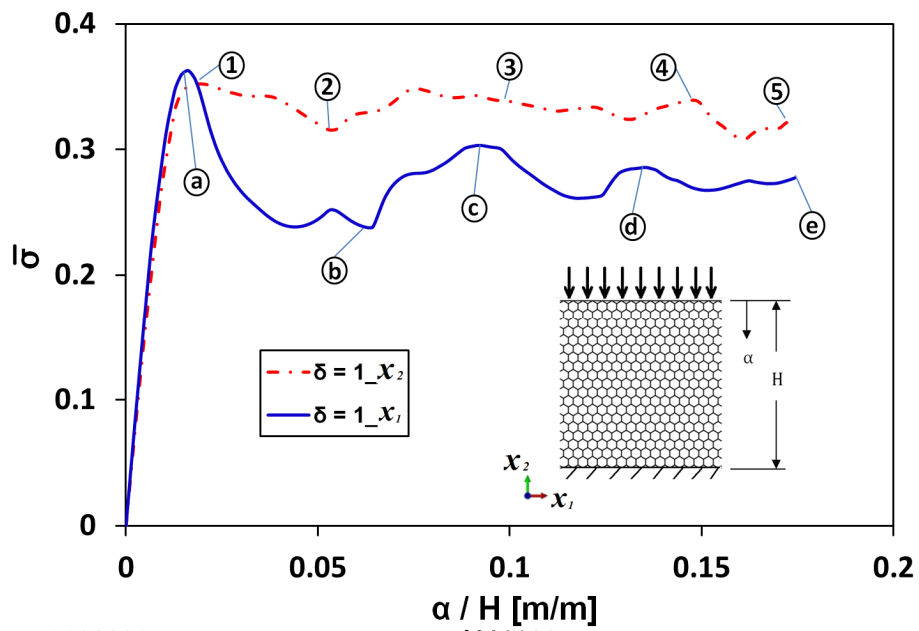
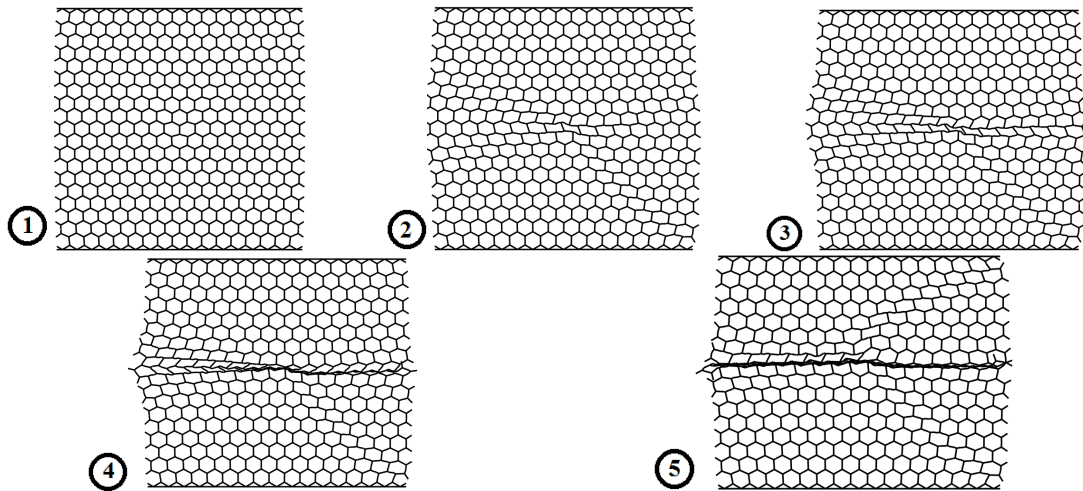


Figure 4.9: Stress-Strain curves for a 9% Al Voronoi honeycomb of 40 ppi and $\delta = 1$.

Regarding the plateau region, the characteristic oscillations are present in all the simulations. The variation in the magnitude of plateau strength for different regularities is analyzed in section 4.3. As can be seen in Fig. 4.5 to 4.8 the plateau strength is comparable for geometries with $\delta = \{0, 0.5, 0.7, \text{ and } 0.8\}$ in the x_1 and x_2 directions. The small variations are attributed to the random of generating the Voronoi honeycombs. For example, two geometries generated with the same regularity and same number of nuclei will not have the same morphology due to the fact that nuclei are generated randomly generated in the control area. Indeed, each time the SSI algorithm is run, it will generate a different pattern of points even if the initial parameters do not change. However, for a given pattern of points, the Voronoi diagram is unique; the variation is just a matter of different seed points. Consequently, simulations suggest that Voronoi honeycombs generated from a SSI have essentially an isotropic behavior in the elastic and plastic regimes. From Fig. 4.9 ($\delta = 1$), it is clear that isotropy seen in terms of the elastic modulus and plastic-collapse strength is lost for the plateau strength. This difference has also been observed experimentally [13, 60]. The difference is attributed to the double wall characteristic of hexagonal honeycombs due to the manufacturing process [2]. However, the current results suggest that a modest difference in the plateau strength for hexagonal honeycombs with a bilinear stress-strain response is present for regular honeycombs with cell walls of the same thickness. Recall from the previous chapters that regular honeycombs with cell walls of the same thickness were generated in order to make the geometries comparable with the irregular counterparts. Likewise, Cricri et al., [13] have also simulated crushing response of a regular assembly of hexagonal cells. They too obtain an anisotropic response in the plateau strength although they have not explicitly made this observation. The present results indicate that the difference in terms of plateau strength does not exceed $\sim 12\%$, and it is even smaller for lower relative

densities. For example, the difference between the plateau strength in the x_1 and x_2 directions in regular honeycombs with $\bar{\rho} = 3\%$ is just 2.3%.

The deformed shapes of Voronoi honeycombs present a behavior homologous to regular honeycombs. First, the elastic response does not show any localization of the deformations. When the plastic-collapse strength is reached, a drop in the stress-strain curve is observed. Subsequently, the deformation begins to localize when the weakest cell of the Voronoi honeycomb collapses. In regular honeycombs, the first cells to collapse are located close to the center of the structure. However, in case of irregular honeycombs, the first cells to collapse are more randomly located within the control area. In regular honeycombs compressed in the x_2 direction, after the first cell collapses, all other cells in the horizontal row collapse. Apparently, the horizontal row is the weakest path for the collapse event. On the other hand, in irregular honeycombs, the weakest path tends to be horizontal (vertical for the case of compression in the x_1 direction) but not necessarily straight. Once the first cell collapses, the deformation localizes along a diagonal or a curved path passing through this first collapsed cell. Essentially, when the collapsed path is completely closed, opposite cell walls touch each other and the structure stiffens again. This causes the oscillations seen in the plots. The instability originated by the first crushing path causes a collapse in the neighboring cells localizing the deformation close to the original path. Nevertheless, new independent paths at other locations of the structure can also appear but they can be traced back to the original disturbance (see Fig 4.8(5)).

A similar analysis can be performed for deformed shapes of Voronoi honeycombs compressed in the x_1 direction. Essentially, the response is comparable with the ones observed in the x_2 compression cases for all the Voronoi honeycombs with the exception of $\delta = 1$. For regular honeycombs compressed in the x_1 direction, the collapse path follows a diagonal path originated at the corners of the control area. The corners where the diagonal

collapsing paths originates are the ones corresponding to the displacement applied (see Fig. 4.9). The collapsing paths localized the deformation along two diagonals forming an “x” shape. Such a pattern has been observed experimentally although natural imperfections present in experiments cause asymmetric collapse.

The effect of generating two geometries with the same regularity but in different trials can be observed in Fig. 4.10. Figure 4.10 presents results shown in Fig 4.8 along with an additional geometry generated with the same regularity ($\delta = 0.8$) in a different trial and compressed in the x_2 direction.

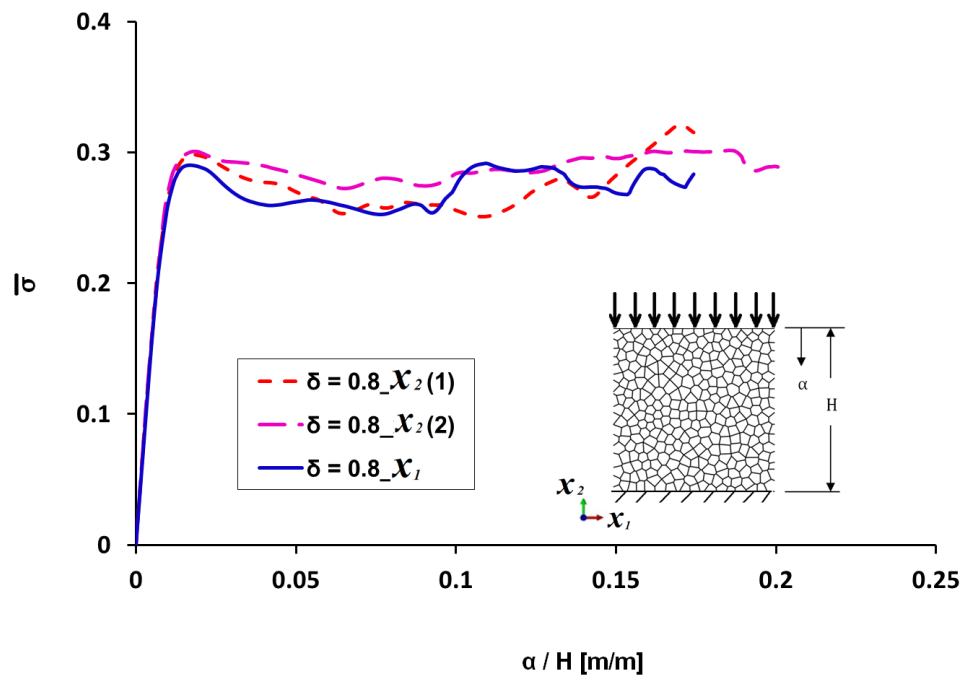


Figure 4.10: Al Voronoi honeycomb response with $\bar{\rho} = 9\%$ for $\delta = 0.8$ compressed in the x_2 . The two broken lines correspond to two separate sets of nuclei.

As observed in Fig. 4.10, the effect of generating two different geometries configurations with the same regularity but in a different trial (using a different set of nuclei) does not affect the prediction of elastic modulus and introduce a minor variation in terms of oscillation in the plastic region. Indeed, the oscillations are not exactly similar for the two

Voronoi honeycombs even though the regularity parameter δ is the same. Moreover, the variation of oscillations in the plastic regime is comparable to the oscillation observed for compression in the x_1 direction. For that reason, simulations of geometries generated with a SSI process and compressed in the x_1 can be considered as simulations performed over a new Voronoi honeycomb configurations with the same regularity but in a different trial (or a different set of nuclei points).

In summary, the analysis of the crushing response of Voronoi honeycombs suggests isotropic behavior in the elastic and plateau regimes for regularities in the range of 0 to ~ 0.8 . For Voronoi honeycombs with $\delta = 1$, the isotropic behavior has been observed in the elastic region while the plateau strength presents a modest difference depending on the loading direction. Nevertheless, this variation does not exceed $\sim 12\%$ for $\bar{\rho} = 9\%$ and is even smaller for lower relative densities. For example, the difference between the plateau strength in x_1 and x_2 directions in regular honeycombs with $\bar{\rho} = 3\%$ is just 2.3%. The influence of the relative density in the crushing response of Voronoi honeycombs is further analyzed in section 4.4. Previously, the influence of the regularity parameter on the crushing response of Voronoi honeycombs is studied in section 4.3.

4.3. Role of regularity

Stress-strain responses for compression in the x_2 direction of different Voronoi honeycombs are superimposed in the Figs. 4.11 and 4.12 for the case of $\bar{\rho} = 9\%$. In order to appreciate the effect of regularity on the elastic modulus and plastic-collapse strength, Fig 4.11 shows the response only in the strain range 0 to 0.025.

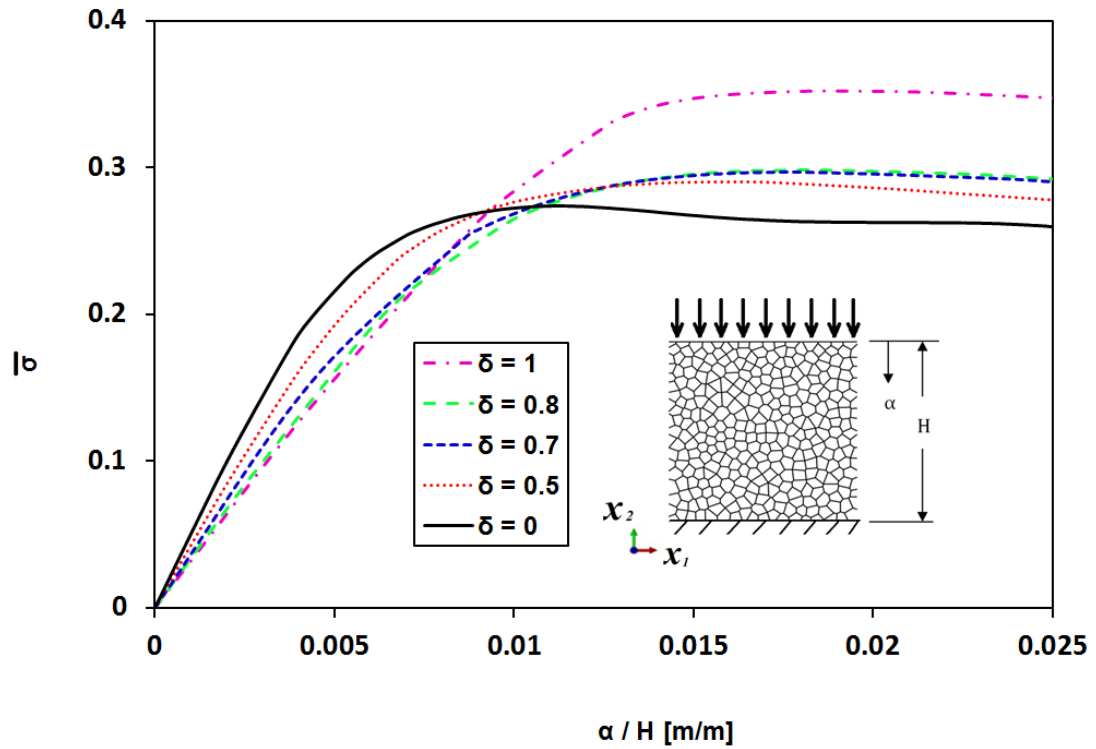


Figure 4.11: Al Voronoi honeycomb response with $\bar{\rho} = 9\%$ for different regularities compressed in the x_2 direction.

Figure 4.11, suggests an inverse relationship between regularity and stiffness at low strains. Consequently, highly irregular Voronoi honeycombs have higher values of elastic modulus than their regular counterparts. Zhu et al., [17] and Silva et al., [15] have also suggested that irregular 2D Voronoi honeycombs are stiffer than the regular honeycombs. As shown in Fig. 4.11, an inflection point can be identified around a strain of ~ 0.01 for the case of $\bar{\rho} = 9\%$. On the other hand, plastic-collapse strength and plateau strength show a direct relation with the regularity parameter as see in Fig. 4.11 and 4.12.

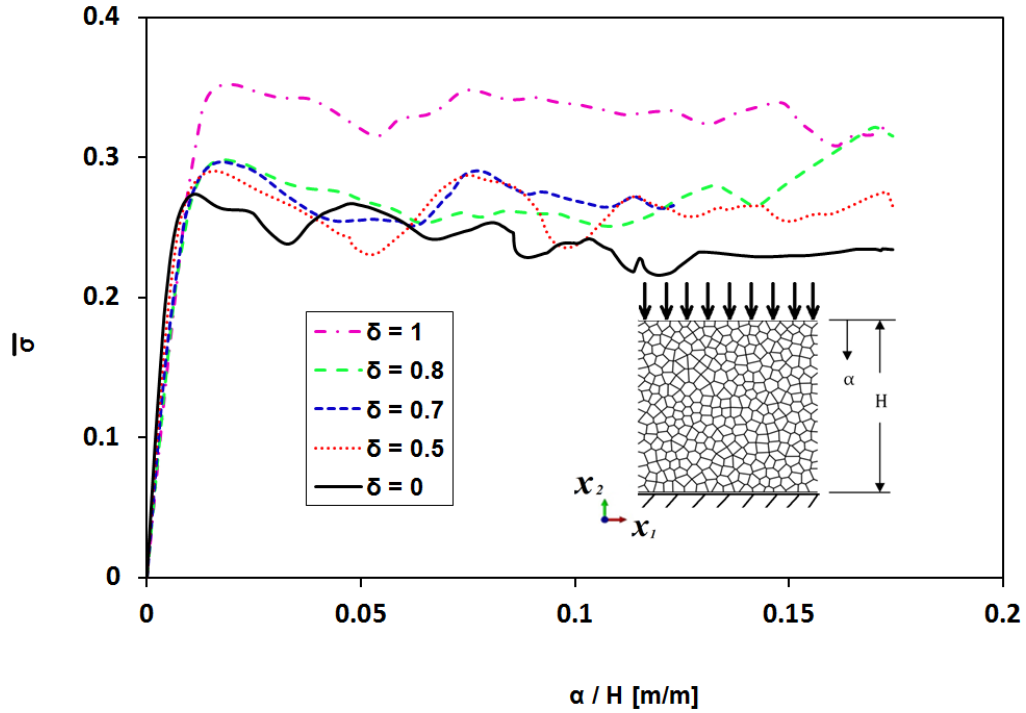


Figure 4.12: Stress-strain curves for Al Voronoi honeycombs with a $\bar{\rho} = 9\%$ for different levels of randomness compressed in the x_2 direction.

Even though details of the oscillatory nature of the response in the plateau regime are difficult to interpret, the average plateau strength values show the influence of regularity. Comparable results similar to the ones in Fig. 4.11 and 4.12 are observed for the remaining densities (7%, 5% and 3%). A summary of key characteristics such as elastic modulus, plastic-collapse strength and plateau strength are presented in Figs. 4.13, 4.14, and 4.15 for quantitative analysis. Recall from the previous sections that plastic-collapse strength is calculated as the maximum value of stress reached before the cells start collapsing due to formation of plastic hinges while plateau strength is calculated by averaging the stress value after the plastic-collapse strength has been reached. The difference between plastic-collapse strength and plateau strength is not very significant for most of the simulations. However, the differentiation has been included due to the fact that this difference is modest in geometries with a regularity equal to 1 and relatively higher density (see Fig 4.8). Moreover, due to the

isotropic response of all the Voronoi honeycomb configurations in the elastic range, the measurement of elastic modulus and plastic-collapse strength has been averaged between x_1 and x_2 directions for calculations presented in Figs. 4.13 and 4.14. On the other hand, plateau strength is averaged in the x_1 and x_2 direction in the range from $\delta = 0$ to $\delta = 0.8$ since $\delta = 1$ cannot be considered completely isotropic particularly for higher densities.

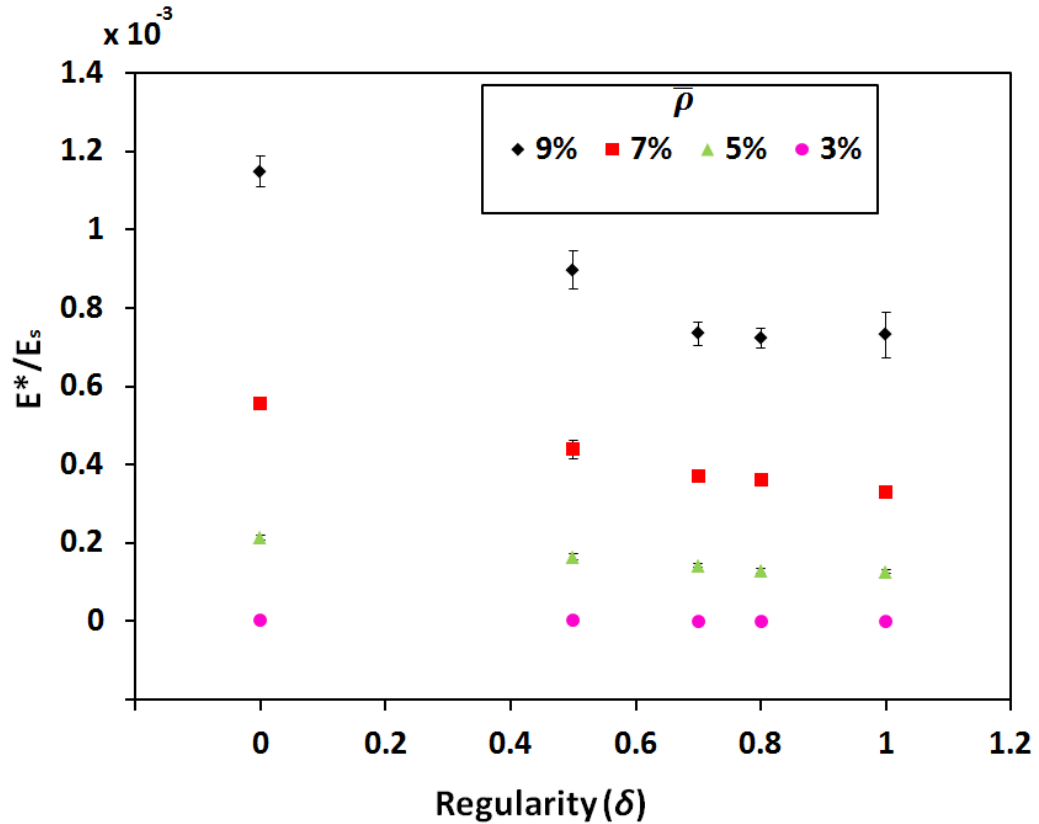


Figure 4.13: Effect of regularity on elastic modulus of Voronoi honeycombs of different relative densities.

As suggested by Fig. 4.13, the general trend of stiffer response of irregular structures is common for all the relative densities. Silva et al., [15] also compare elastic response of irregular honeycombs with regular ones although the comparison was limited to honeycombs of $\delta \sim 0.7$ and regular ones, $\delta = 1$. In the present thesis the difference, in terms of elastic

modulus, between honeycombs with $\delta \sim 0.7$ and $\delta = 1$ is $\sim 8\%$ while Silva et al., found a difference of $\sim 6\%$. However, a wider view suggests a sharp rise of elastic modulus for Voronoi honeycombs with regularity $\delta < 0.7$. Indeed, the data suggest that a fully irregular Voronoi honeycomb ($\delta = 0$) is $\sim 66\%$ stiffer than a regular honeycomb.

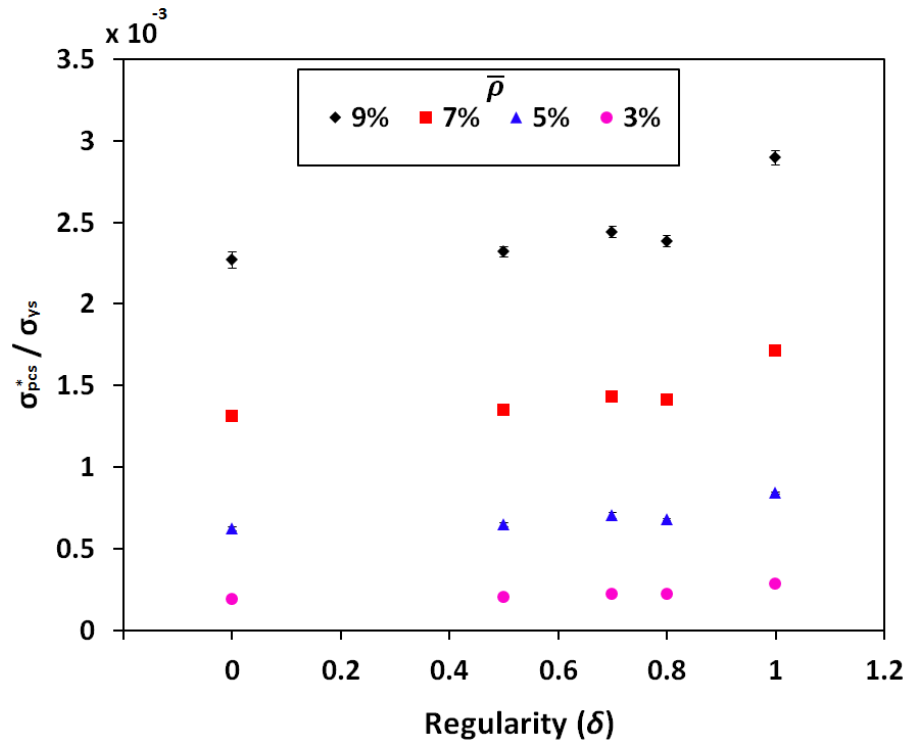


Figure 4.14: Effect of regularity on plastic-collapse strength of Voronoi honeycombs for different relative densities.

As can be seen in Fig. 4.14 and 4.15, the plastic-collapse strength and plateau strength increase with regularity. Indeed, plastic-collapse strength of regular honeycombs is {28%, 31%, 35% and 50%} higher than a fully irregular honeycombs for relative densities of $\bar{\rho} = \{9\%, 7\%, 5\%, 3\%\}$, respectively. For plastic-collapse strength, the trend is relatively constant between $\delta = 0$ and $\delta = 0.8$ with a considerable improvement in the range of $\delta = 0.8$ to $\delta = 1$. Similarly, plateau strength of Voronoi honeycombs with $\delta = 0.8$ are {10%, 8%, 11%, and 20%} higher than the Voronoi honeycombs with $\delta = 0$ for $\bar{\rho} = \{9\%, 7\%, 5\%, 3\%\}$, respectively (see Fig. 4.15). Although the values of plateau strength for $\delta = 1$ have not been

included in Fig. 4.15 since they are not isotropic, the data suggests an improvement in plateau strength of {33%, 15%, 21%, and 28%} for Voronoi honeycombs compressed in the x_2 direction compared to a fully irregular Voronoi honeycomb ($\delta = 0$).

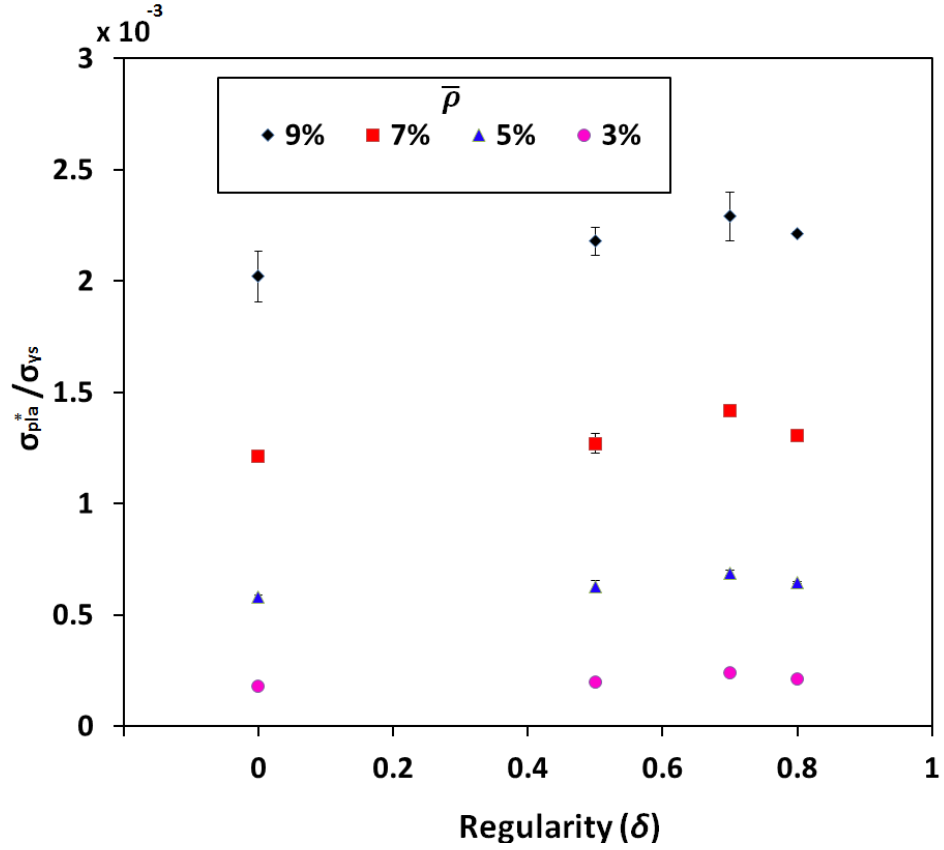


Figure 4.15: Influence of regularity parameter on plateau strength of Voronoi honeycombs of different relative densities.

4.4. The effect of relative density

Numerical simulations confirm that the reduction of the elastic modulus scales with $(\rho^* / \rho_s)^3$ [61, 62]. Table 4.2 fits the data to a curve of the form,

$$\frac{E^*}{E_s} = C1 \left(\frac{\rho^*}{\rho_s} \right)^3$$

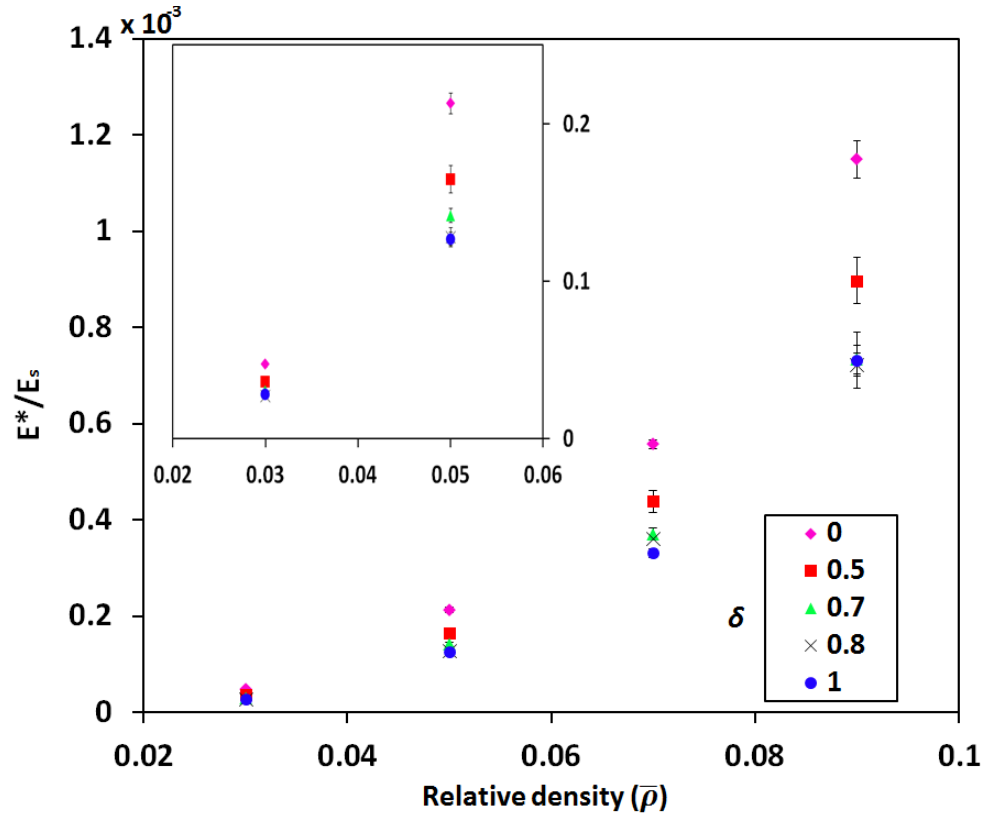


Figure 4.16: Variation of elastic modulus of Voronoi honeycombs with relative density for different regularities.

Regularity	C1	Coefficient of determination
0	1.587	0.9993
0.5	1.241	0.9993
0.7	1.023	0.9975
0.8	1.003	0.9988
1	0.9962	0.9995

Table 4.2: Elastic modulus data fitting for Voronoi honeycombs with different regularities.

Similarly, numerical simulations of Voronoi honeycombs confirm that the reduction of the plastic-collapse strength depends on $(\rho^*/\rho_s)^2$ [61, 62]. Table 4.3 fits the data to a curve of the form,

$$\frac{\sigma_{pcs}^*}{\sigma_{ys}} = C2 \left(\frac{\rho^*}{\rho_s} \right)^2$$

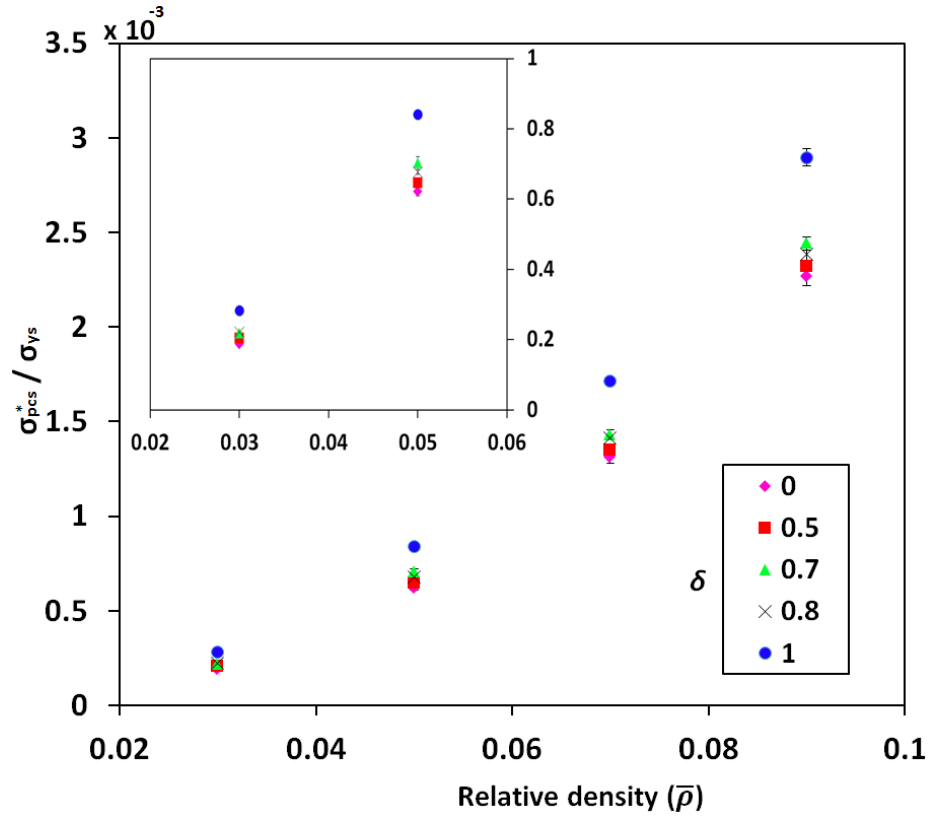


Figure 4.17: Plastic-collapse strength vs. relative density for different regularities.

Regularity	C2	Coefficient of determination
0	0.2741	0.9955
0.5	0.2814	0.9967
0.7	0.2972	0.9979
0.8	0.2909	0.9981
1	0.3538	0.9988

Table 4.3: Plastic-collapse strength data fitting for Voronoi honeycombs with different regularities.

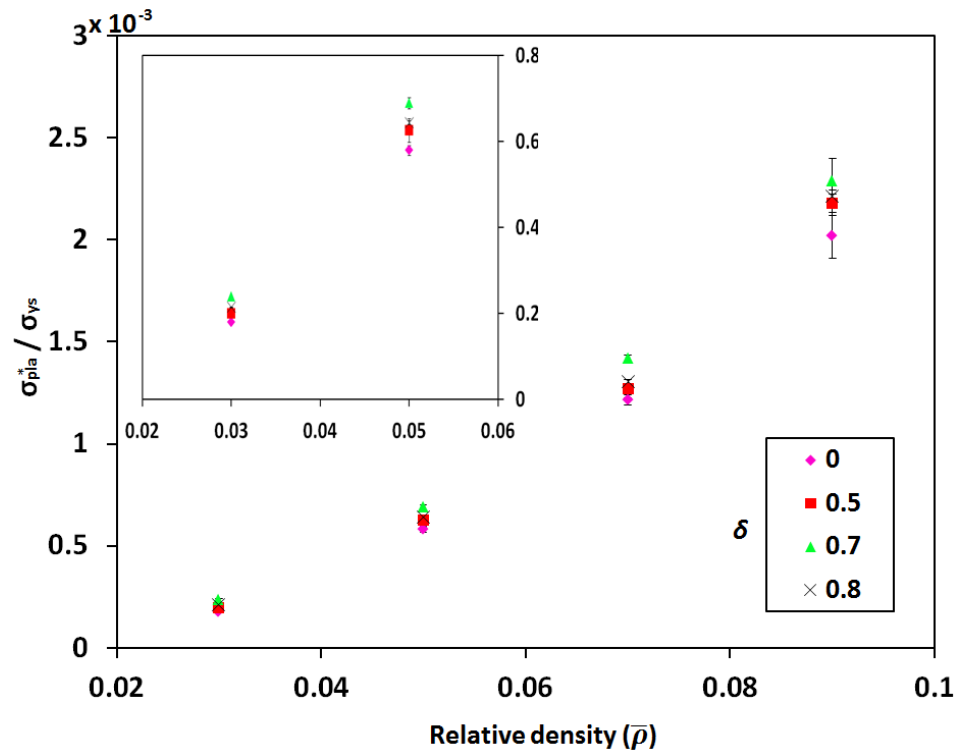


Figure 4.18: Plateau strength vs. relative density for different regularities.

The plateau stress also varies with respect to $(\rho^*/\rho_s)^2$ with similar characteristics of the plastic-collapse strength since the difference is just important in Voronoi diagrams with regularity ($\delta = 1$) and high levels of relative density.

CHAPTER 5

FINITE ELEMENT MODELING OF FOAM-FILLED VORONOI HONEYCOMBS

The influence of regularity on the mechanical response of foams has been studied whereas a lack of research is evident for the case of foam-filled Voronoi honeycombs (2D) or interpenetrating phase composites (3D). This chapter describes modeling and simulation of the compressive behavior of foam-filled Voronoi honeycombs. A detailed description of modeling is presented in this chapter. While chapter 4 described the procedure to simulate Voronoi honeycombs with a single phase material, in the present chapter interaction of two phases are considered. The main objective is studying the effect of regularity of foam-filled Voronoi honeycombs and their comparison with unfilled counterparts. Consequently, simulations were carried out on the same Voronoi 2D configuration of $\delta = \{0, 0.5, 0.7, 0.8$ and $1\}$ as in chapter 4. However, this time the geometries are represented in the context of wet configurations. Recall from the previous chapters that a wet configuration has a thickness associated with the Voronoi honeycomb in the part geometry. Basically, the wet Voronoi honeycomb configuration divides the control area into two regions. A continuous region that represents the (first) aluminum foam phase and a complementary area that represents the (second) syntactic foam phase. The aluminum phase has the same characteristics described in chapter 4 (see also, Appendix A). The syntactic foam phase used in these analyses were assumed to contain 40% hollow glass spheres dispersed in an epoxy matrix and is identified as “SF-40” in the present thesis. The effect of volume fraction of spheres on the quasi static compression response of syntactic foams has been studied previously by Periasamy and Tippur [56] and their results are utilized in the present work. In section 5.1, the approach followed during modeling is detailed in a chronological order (following Abaqus/CAE model tree). Subsequently, the effect of loading direction is studied in section 5.2. Section 5.3 deals

with the influence of regularity. All the numerical simulations are carried out using Abaqus/Standard® v 6.10-2 software in a parallel processing environment.

5.1. Finite Element Modeling of Voronoi Aluminum-Syntactic foam composites.

In the pre-processing stage, the geometry of the 2D Voronoi configurations were developed by applying the method described in section 3.2. Five types of geometries with randomness of $\delta = \{0, 0.5, 0.7, 0.8 \text{ and } 1\}$ were generated. Subsequently, in order to develop wet geometries, the flowchart steps presented in Fig. 3.2 are followed until the level (e). The other detailed procedures are presented in section 3.2. Based on the Voronoi wet configuration, the two phases required for the simulation are created in AutoCAD®. The value of the strut thickness (h_i) depends on the density of the foam. Hence, the thickness of each Voronoi configuration varies depending on the level of randomness as a consequence of the variation of the length of ligaments and the value of relative density of the foam ($\bar{\rho}$) (see table 4.1). Basically, the wet Voronoi honeycomb configuration divides the control area in two regions. A continuous region that represents the aluminum phase and a complementary region that represents the syntactic foam phase. Additionally, two aluminum (AL-6061) face sheets (0.813mm thick) were merged with the aluminum phase to simulate a sandwich structure. The two phases are imported into Abaqus® to generate 2D parts through ACIS SAT (*.sat) files.

Next, the same material model used in chapter 4 and presented in Fig. 4.2 is applied for simulating the response of aluminum in the elastic and plastic regimes. The material model used for the case of syntactic foam with 40% volume fraction of hollow microballons is based on the work of Periasamy et al., [56]. They performed quasi static compression tests on syntactic foam specimens according to ASTM D-695 standard. The two components of the syntactic foam contained a low viscosity epoxy (Epo-Thin and produced by Beuhler, Inc. USA) and hollow glass microballons (K-1™ from 3M corp). of approximately 60 μm

average diameter and wall thickness of $\sim 0.6 \mu\text{m}$ [56]. Properties of the constituents are presented in Table 5.1.

Properties	Neat Epoxy	Microballons
Elastic Modulus (MPa)	3200	-
Bulk Density (Kg/m^3)	1175	125
Poisson's ratio	0.34	-

Table 5.1: Properties of the constituents of syntactic foam constituents.

Periasamy et al., studied the effect of varying the volume fraction of microballons. Quasi static compression response of specimens with 10%, 20%, 30%, 40% volume fraction of microballons were analyzed. The authors concluded that the mechanical properties vary in an inverse monotonic fashion with the volume fraction of microballons. The data for compression response of 40% volume fraction of microballons presented by Periasamy et al., [56] is shown in Fig. 5.1 and is used as an input for FE simulations throughout this thesis. The compression and tension response is assumed to be comparable in an elasto-plastic model with ten piecewise linear sections in the plastic regime. Modulus of elasticity for SF-40 calculated from the data provided by Periasamy and Tippur [56] is equal to 1260.5 MPa with a Poisson's ratio of 0.34 (see also [8]). Next, solid homogeneous sections were created for both the aluminum and syntactic foams phases. Subsequently, sections were assigned to the respective parts which were merged in the assembly simulating a perfectly bonded condition between the two phases. In the assembly module of Abaqus, three horizontal and three vertical partitions were generated within the control area in order to track stress and strain values far from the boundaries. Assuming a control area of sides $2l \times 2l$ with the origin at the center of the control area, the horizontal partitions are generated at 0 and $\pm \frac{1}{2} l$. Similarly, the vertical partitions were generated at 0 and $\pm \frac{3}{4} l$ as shown in Fig. 5.2. Three

control sets of nodes were created at the intersection of the partitions. The three sets created are depicted in Fig. 5.2 as thick red lines.

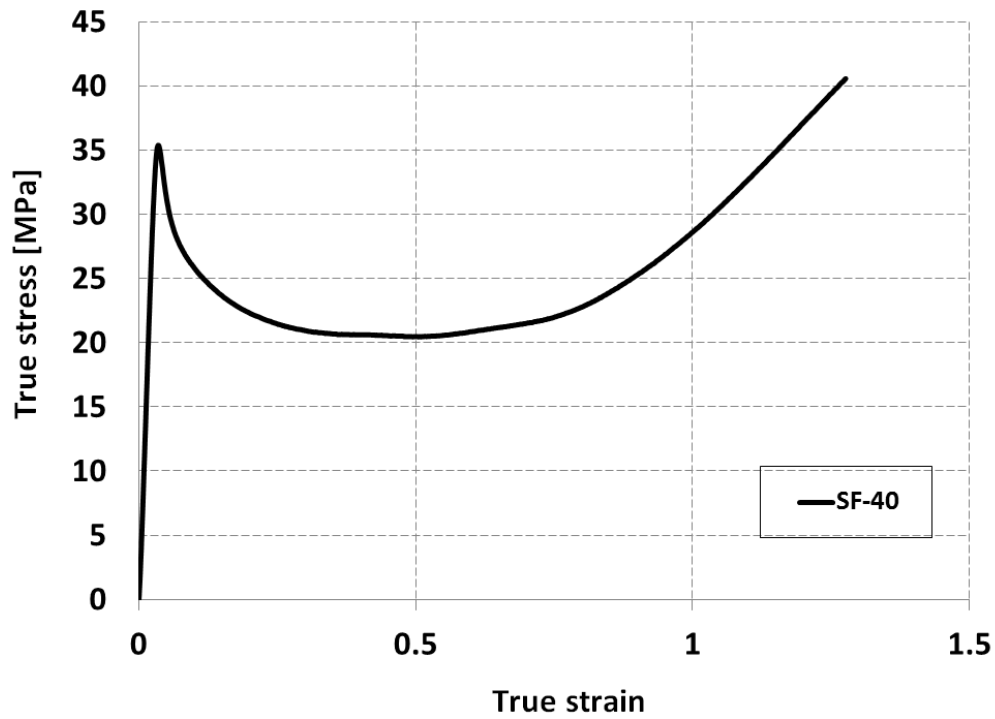


Figure 5.1: Experimental obtained compression response of syntactic foam with 40% volume fraction of hollow microballons in epoxy matrix.

Stress and strain data along the three sets shown in Fig. 5.2 were extracted for further analysis. A comparable technique was used for the case of compression in the x_l direction. The corresponding sets created were oriented vertically and are not shown in Fig. 5.2.

Next, the nonlinear effects due to large deformations were activated in a general static analysis performed in ABAQUS/Standard module. Moreover, unstable nonlinear problems require an adaptive automatic stabilization scheme [10, 57]. Values of 2×10^{-4} and 0.05 for dissipated energy fraction and ratio of stabilization to strain energy were used in in the

present work. Furthermore, the number of attempts per increment is set to 10 and the allowable time increment was reduced to $1 \times 10^{-8} s$ for stability.

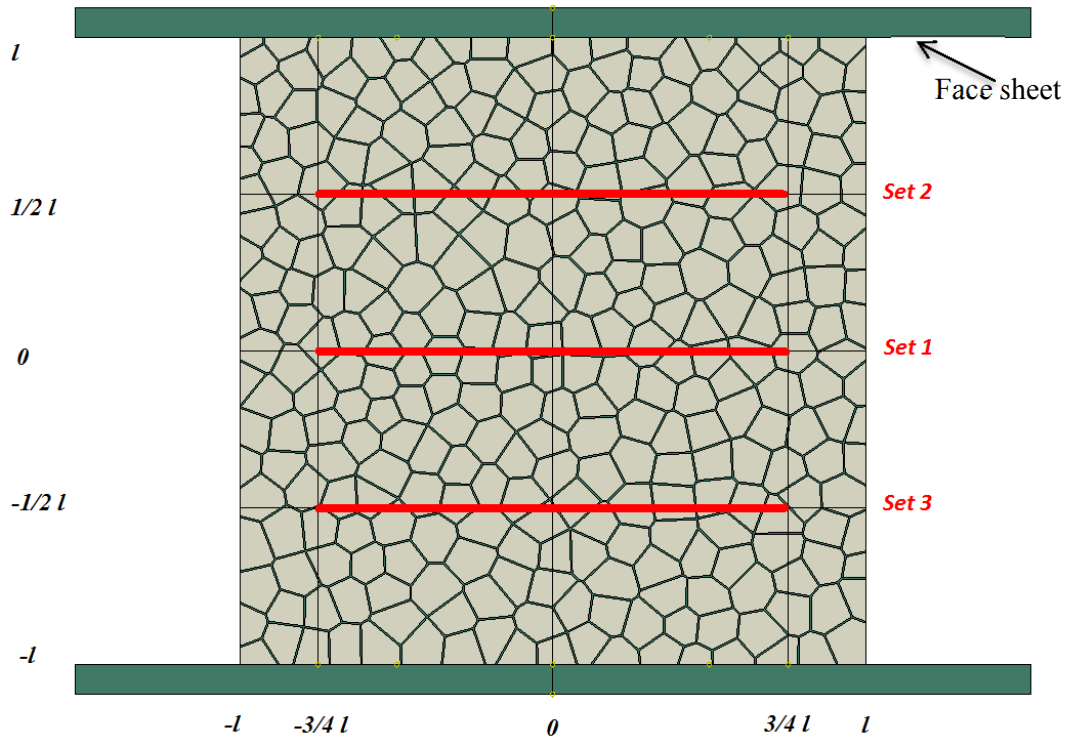


Figure 5.2: Partitions on a two-phase composite and the corresponding sets created (example shown $\delta = 0.8$, compression in the x_2 direction)

In order to prevent interpenetration of nodes into the face sheets at the corners of the control area, a surface along the border of the whole structure was created and a frictionless interaction of the self-contact type was stipulated for this surface.

A smoothed step displacement boundary condition (instead of boundary forces) was applied at the top and bottom surfaces of the model. As in Voronoi honeycombs, a restriction for displacement in the x_1 direction was imposed to a single point at the top and bottom surfaces. For example, Fig. 5.3 illustrates the boundary conditions applied over a two-phase composite with a regularity of $\delta = 0.8$ compressed in the x_2 direction. In order to understand

the directional dependency, the 2D two phase-composite was loaded in both x_2 and x_1 directions. The boundary conditions differ for the 2D two phase-composite compressed in the x_1 direction. In this case, boundary conditions were rotated by 90 degrees without rotating the 2D cellular material.

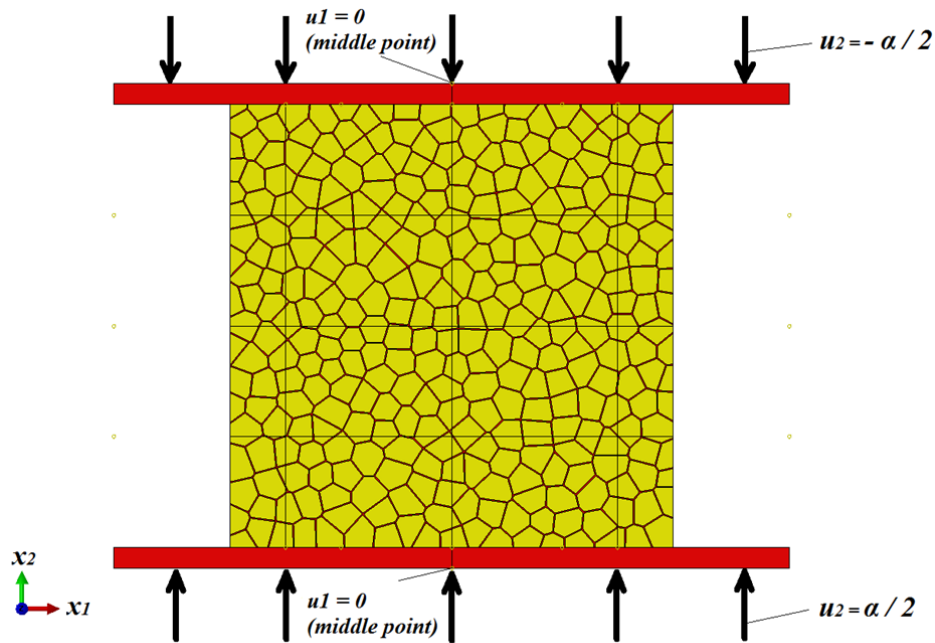


Figure 5.3: Boundary conditions for the two phase composite simulation (example shown $\delta = 0.8$ loaded in x_2 direction).

Four-node, bilinear, plane strain quadrilateral, reduced integration elements with two active degrees of freedom per node and a linear interpolation within the domain were the elements selected for FE discretization. Plane strain elements assume the out of plain strain to be zero and are suitable for simulating thick structures [57]. The elements are identified as CPE4R in Abaqus® where ‘C’ stands for continuum element, ‘PE’ means plain strain, ‘4’ indicates the number of nodes of the element and the ‘R’ indicates a single point used for integration. A quadrilateral dominated mesh control was stipulated for controlling the mesh generation. The number of elements generated was controlled by setting an approximate element size. The ratio of the element size to the area size with tolerable geometric

characteristics and good convergence is 0.01. If elements with poor shape were generated with the stipulated element size, the approximate element size was changed by of $\pm 5\%$ until no element had a poor shape. The number of elements generated was in the range of 16628 and 17403. Fig. 5.4 illustrates the mesh used for a typical two phase composite.

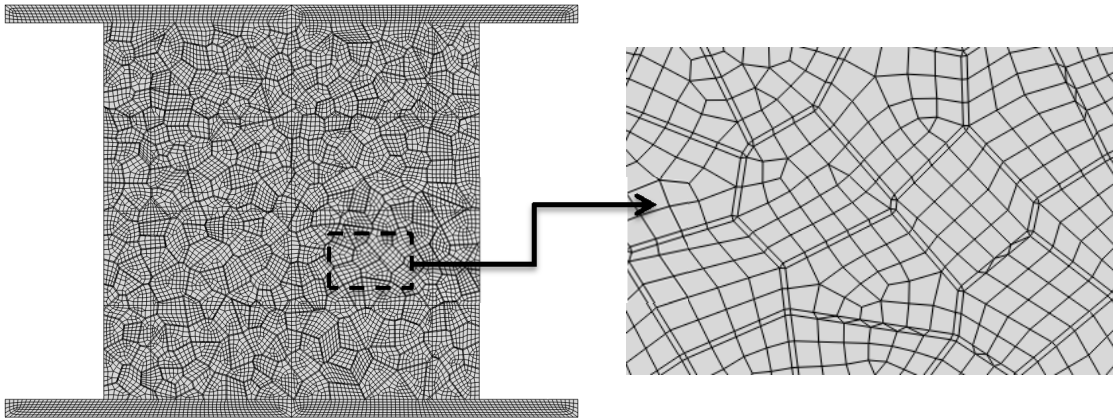


Figure 5.4: Typical mesh configuration for a two phase composite ($\delta = 0.5$ loaded in the x_2 direction).

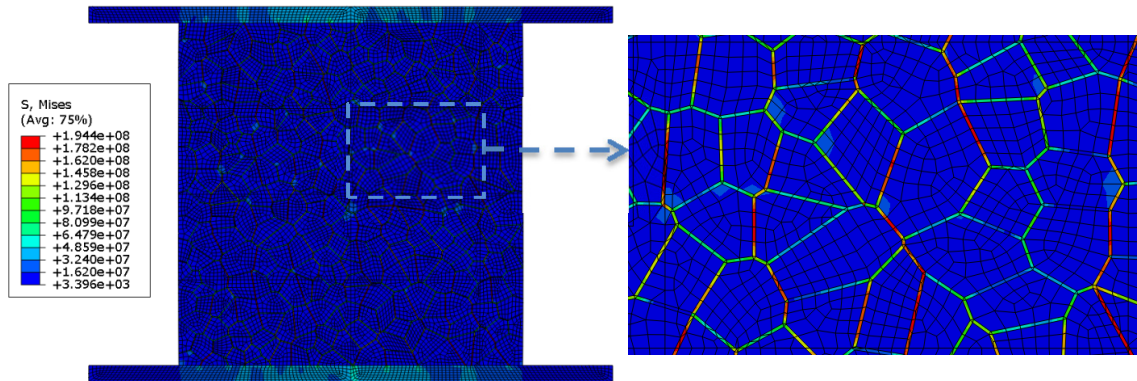
As seen in Fig. 5.4, the majority of elements generated are quadrilateral. However, some triangular elements were also generated in order to complete the mesh in complex regions such as junctions of aluminum Voronoi honeycombs.

In the processing stage, simulations were run as a batch job in a parallel processing environment. The Samuel Ginn College of Engineering High Performance Computer Cluster (HPCC) was used for this purpose.

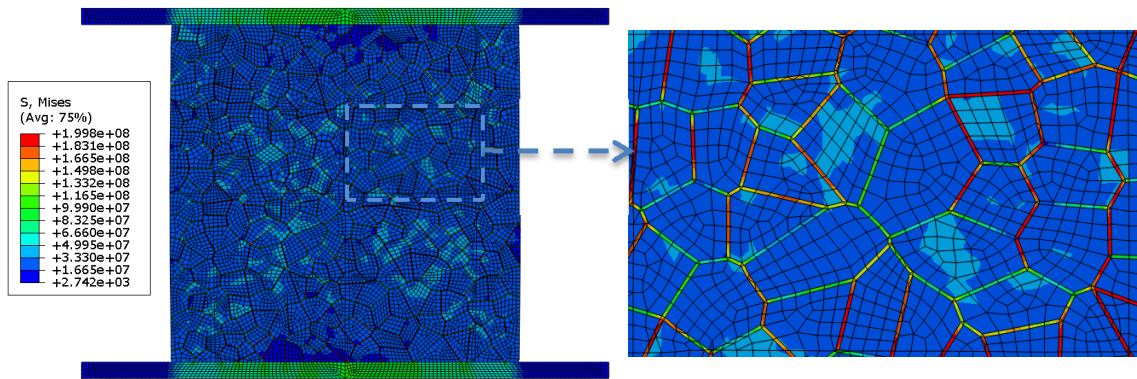
In the post-processing stage, stresses at the integration point of all the elements located in the control sets (presented in Fig. 5.2) were averaged to get one value of stress per control set. The value of stress at locations 0 and $\pm \frac{1}{2} l$ (see fig. 5.2) were averaged again to obtain the stress for the structure. The average strain for the structure was obtained in a

similar way as in Voronoi honeycombs structures. A comparable process was adopted when the imposed displacement was in the x_1 direction. All these calculations were accomplished for every loading increment in order to get continuous mechanical responses.

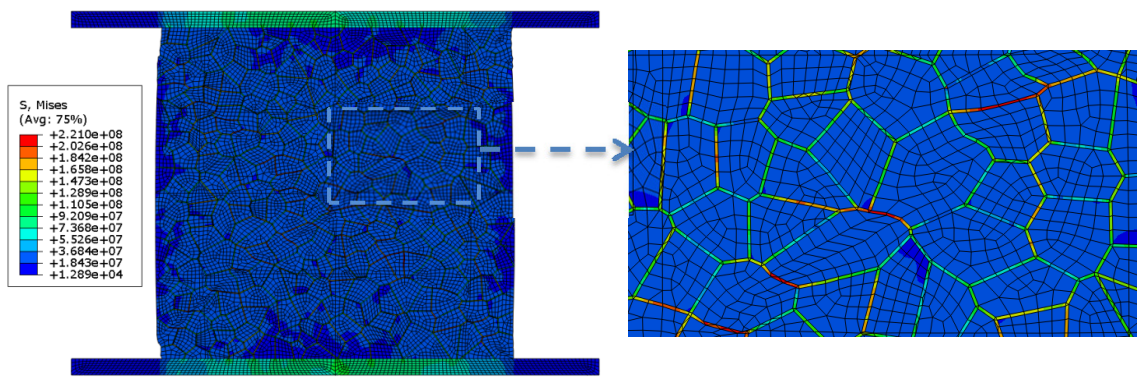
Figure 5.5 presents a typical sequence of deformation observed. In Figure 5.5 and 5.6, contour plots for von Mises stress and maximum in-plane strain, respectively, are plotted for $\delta = 0.5$ case. Results suggest that the metallic Voronoi honeycomb ligaments aligned with the x_2 direction experience higher level of stress at the early stages of the simulation (see Fig. 5.5(a)) while levels of stress in the ligaments aligned with the horizontal direction present a lower value. This is expected since the applied strain is in x_2 direction. On the other hand, stresses in the syntactic foam show lower values compared to that in the metal phase at the early stages. As the simulation progresses, the value of stress in the syntactic foam increases but its value continues to remain lower than that of the metallic ligaments throughout the simulation. Within the control area, four regions show the lowest values of stress as a consequence of being located near to the boundaries. These regions are located in the middle of the sides of the control area (see blue regions inside the control area in Fig. 5.5(c, d, e, and f)). Hence, the three control sets used to average the stress are able to avoid these regions. Additionally, the self-contact interaction condition stipulated at the perimeter of the sample successfully prevented interpenetration of nodes at the intersection of the control area and the face sheets at higher levels of strain. In Fig. 5.6, a uniform deformation of the specimen can be observed at relatively low strains (see Fig. 5.6(a)). Subsequently, deformation localizes along a diagonally oriented narrow band that initiated at the corners of the control area, as in Fig. 5.6(b). When the applied strain is $\sim 5\%$, localization along the two shear bands, can be seen in Fig. 5.6(c). At this stage, barreling in the sample that has also been observed experimentally [8] is evident. Further, deformation spreads to the neighboring cells and shear bands widen.



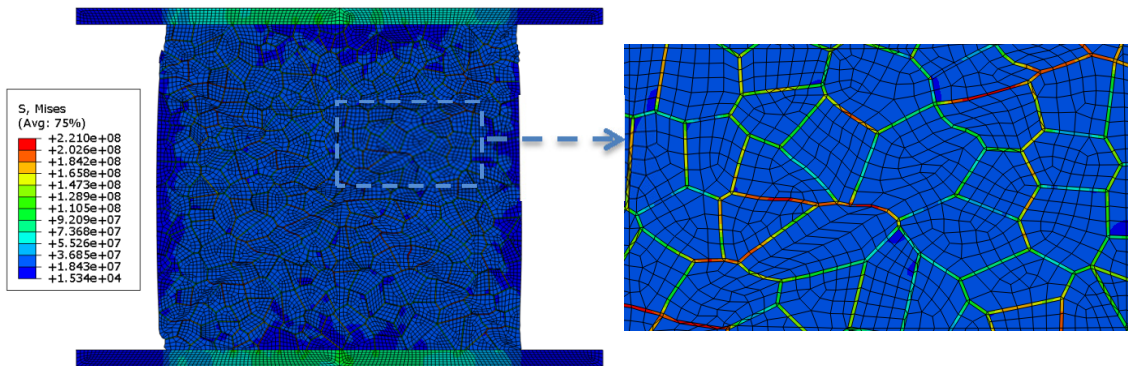
(a)



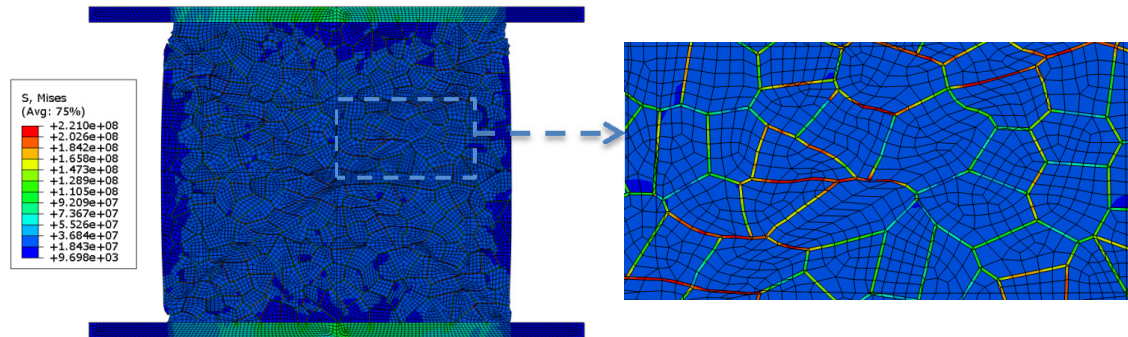
(b)



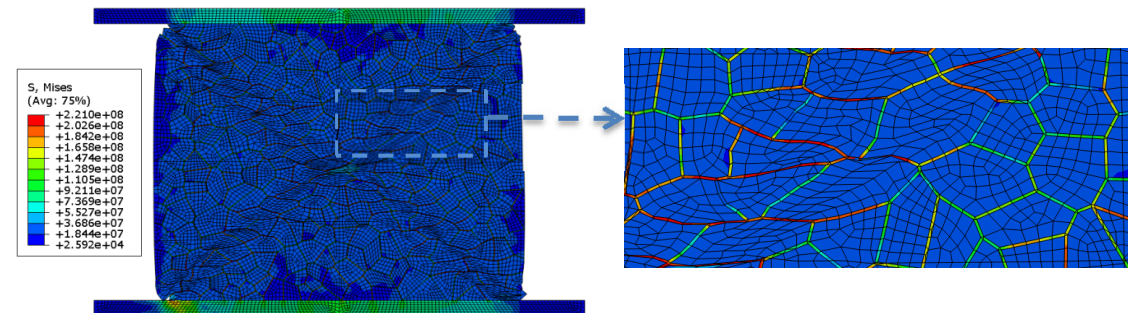
(c)



(d)



(e)



(f)

Figure 5.5: Von Mises stress for applied strains of: (a) 0.5%, (b) 0.7%, (c) 5.03%, (d) 7.06%, (e) 12.02% and (f) 16.06% for $\delta = 0.5$.

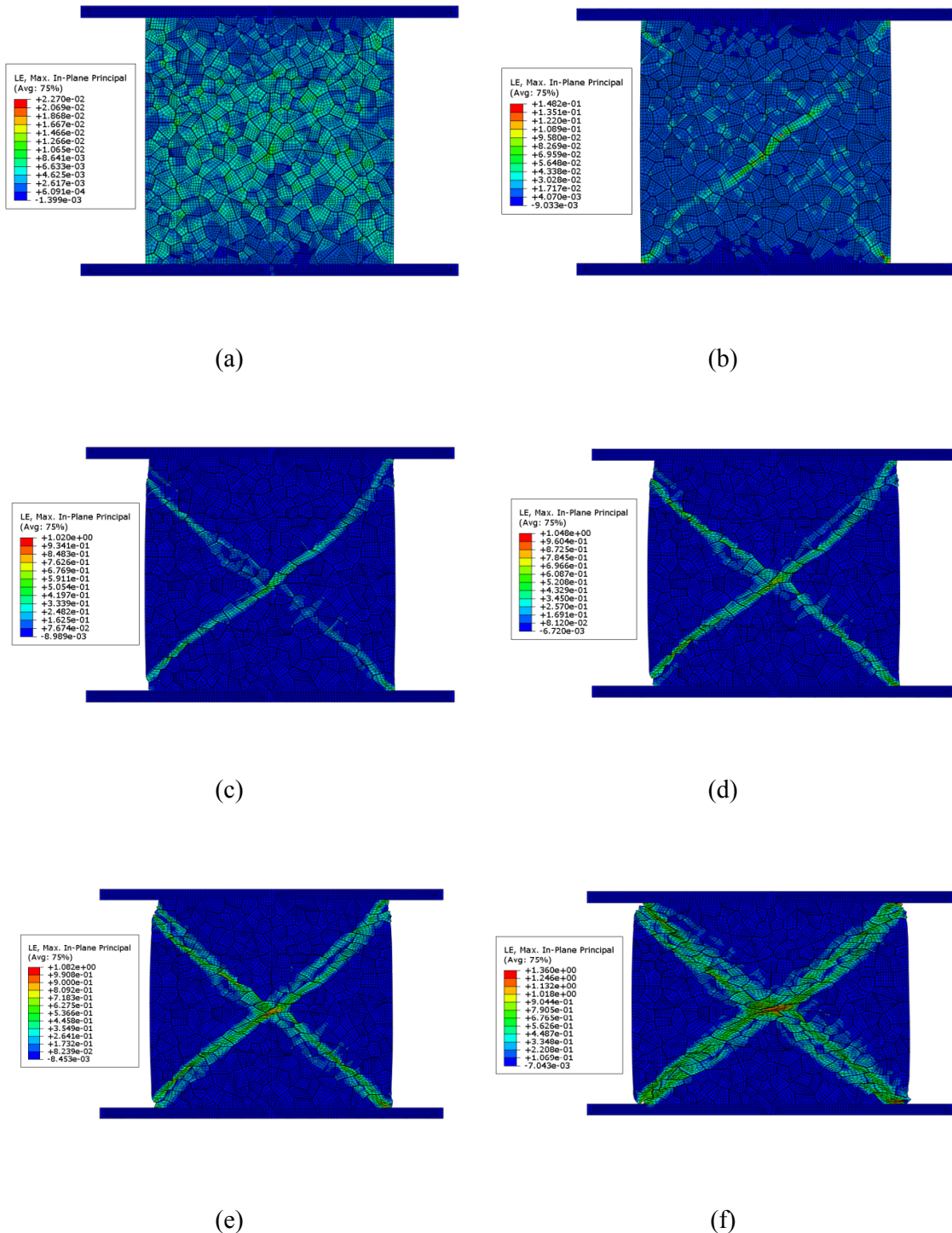


Figure 5.6: Maximum in-plane strain contours at: (a) 0.5%, (b) 0.7%, (c) 5.03%, (d) 7.06%, (e) 12.02% and (f) 16.06% strain for $\delta = 0.5$. (units of stress in the color bar Pa)

Near the center of the sample, the shear bands combine their effects generating high levels of deformation, that can lead to debonding of the two phases as observed by Jhaver [8] (see Fig. 5.6(f)). The observed sequence of deformation is in good agreement with the experimentally observed counterpart in foam-filled honeycombs (see [8]). Comparable results have been observed for $\delta = \{0, 0.7, 0.8, 1\}$ and for geometries compressed in the x_1 direction. The stress-strain response for the example shown in Fig. 5.5 and 5.6 is presented in Fig. 5.10. Previously, the stress-strain response for foam-filled Voronoi honeycombs with $\bar{p} = 9\%$ for different regularities is presented in section 5.2 (see Fig. 5.7 through 5.11) with a direct comparison between the responses in the x_1 and x_2 directions. In section 5.3 the effect of regularity parameter is analyzed.

5.2. The effect of loading direction

In this section a comparison between the compression responses of foam-filled Voronoi honeycombs (with AL-9% and SF-40) subjected to displacement controlled loading in the x_2 and x_1 directions is presented. Figures 5.7 through 5.11 show the responses in the x_2 and x_1 direction for different regularity parameters. Results show that the simulations are able to capture the two initial regimes (elastic and plateau). The foam filling of the empty spaces of the Voronoi honeycombs have reduced the oscillations present in the plateau regime of dry/empty Voronoi honeycombs. Regarding the elastic regimes, all the configurations exhibit a nearly linear variation whose value depends on the level of regularity. In the present section the focus is on the directional response of the foam-filled Voronoi honeycombs. The variation in the elastic modulus for different regularities is analyzed in section 5.3. Essentially, the elastic responses are independent of loading direction in all configurations except $\delta = 1$ where compression along x_2 presents a 44% stiffer response, as shown in Fig. 5.7.

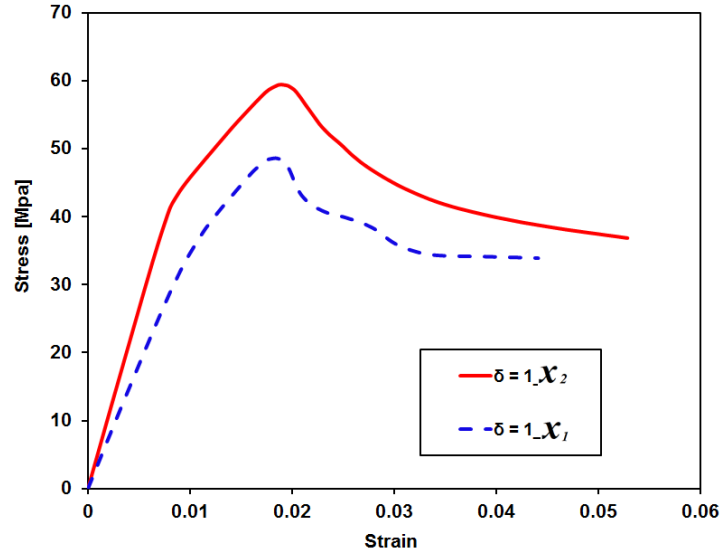


Figure 5.7: Stress-Strain curves of foam-filled Voronoi honeycombs (AL-9% and SF-40),

$$\delta = 1.$$

Similar to Voronoi honeycombs, foam-filled Voronoi honeycombs present improved mechanical characteristics when compressed in the x_2 direction. However, in contrast to the unfilled Voronoi honeycombs, superior mechanical characteristics are present here in both the elastic and plastic regimes while in Voronoi honeycombs the improvement was only evident in the plastic regime for geometries with higher levels of relative density.

For the rest of regularities, results suggest isotropic response. The small variations in stress-strain response for the regularities in the range of 0 to 0.8 are attributed to the random nature of the construction process used to generate the Voronoi geometries. In the plateau region, simulations present a comparable response in terms of plastic-collapse strength and plateau strength in the x_1 and x_2 directions for geometries in the range of $\delta = 0$ to 0.8 while differences of $\sim 22\%$ and $\sim 11\%$ is observed for $\delta = 1$, respectively.

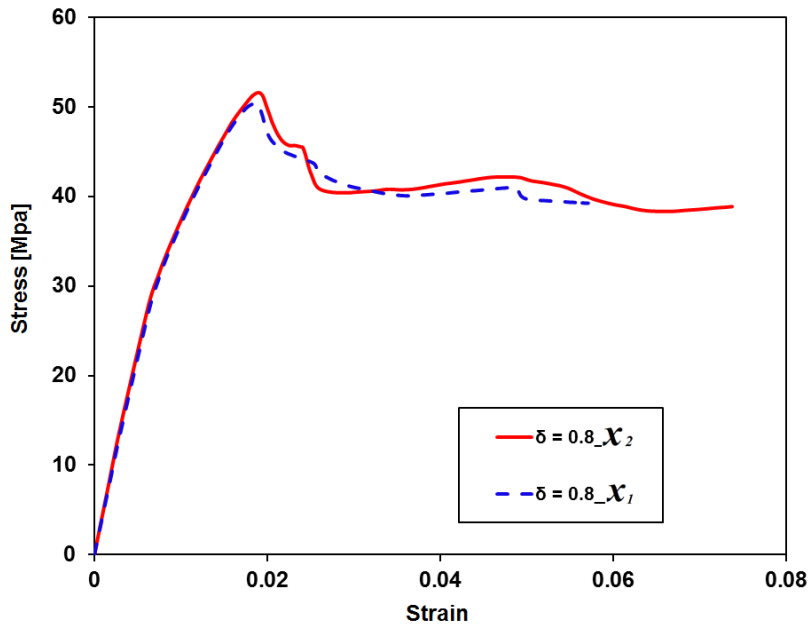


Figure 5.8: Stress-Strain curves of foam-filled Voronoi honeycombs (AL-9% and SF-40), $\delta = 0.8$.

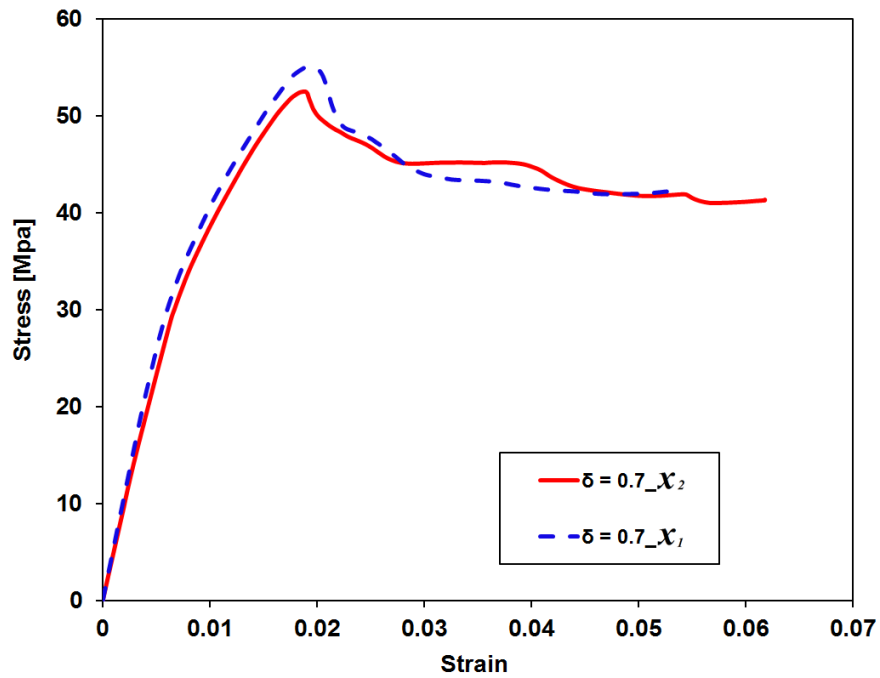


Figure 5.9: Stress-Strain curves of foam-filled Voronoi honeycombs (AL-9% and SF-40), $\delta = 0.7$.

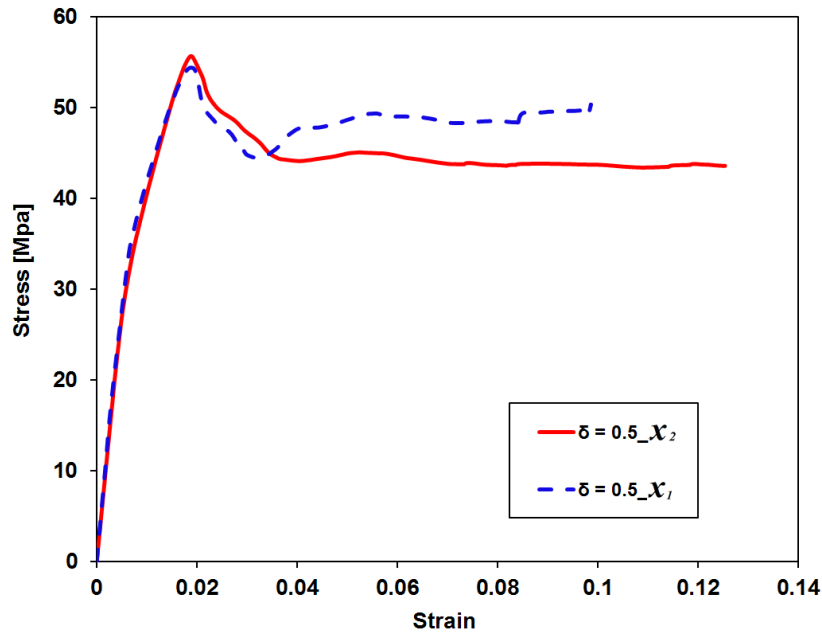


Figure 5.10: Stress-Strain curves of foam-filled Voronoi honeycombs (AL-9% and SF-40), $\delta = 0.5$.

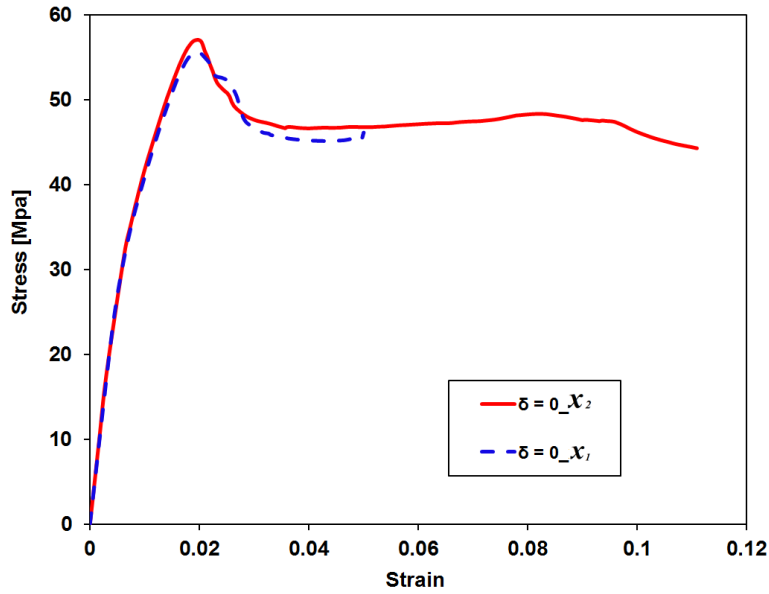


Figure 5.11: Stress-Strain curves of foam-filled Voronoi honeycombs (AL-9% and SF-40), $\delta = 0$

5.3. Dependency on regularity

Stress-strain responses in the x_2 direction of different foam-filled Voronoi honeycombs are superimposed in Figs. 5.12 and 5.13 for $\bar{\rho} = 9\%$. The stress strain response of foam-filled Voronoi honeycomb for $\delta = 1$ but compressed in the x_1 direction has also been included in Fig. 5.12 and 5.13 for comparison. In order to appreciate the role of regularity on the elastic modulus and plastic-collapse strength, Fig 5.12 shows the response only in the strain range of 0 to 0.02. Figure 5.12, suggests an inverse relationship between regularity and stiffness at low strains. Consequently, highly irregular foam-filled Voronoi honeycombs generated with a SSI process have higher values of elasticity modulus. Additionally, results suggest that compression response for geometries generated with a SSI process are nearly bounded between the compression response for regularities with $\delta = 1$ in the x_2 and x_1 directions, as shown in Fig. 5.12.

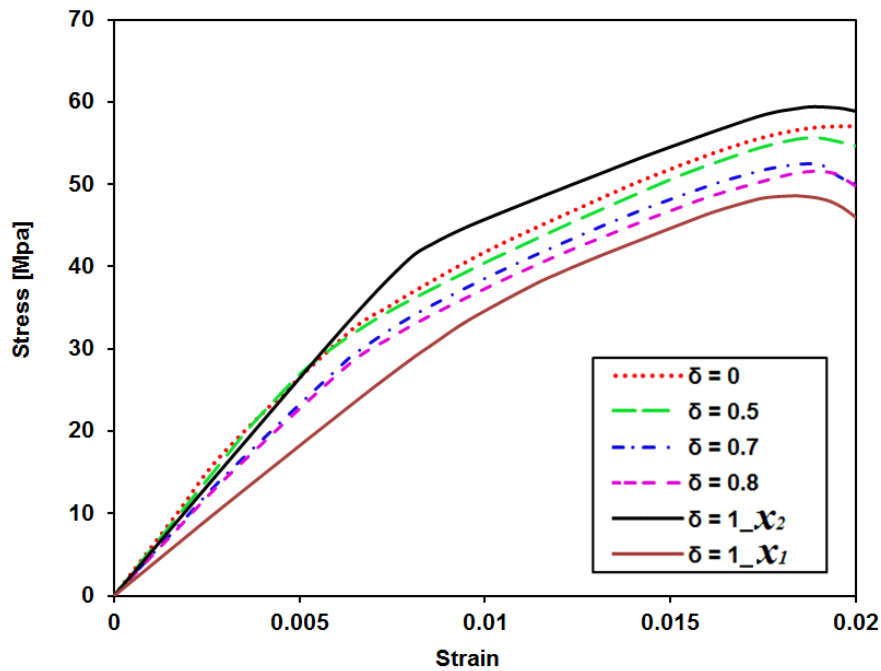


Figure 5.12: Stress-Strain curves of foam-filled Voronoi honeycombs (AL-9% and SF-40) for different regularities in the strain range of 0 to 0.02.

In the plateau region, the drop observed after attaining the plastic-collapse strength is more abrupt for the regular cases, as shown in Fig. 5.13. Hence, the plateau strength for $\delta = 0$ is ~22% and ~26% higher than in regular geometries compressed in the x_2 and x_1 directions, respectively. The influence of regularity on elastic modulus, plastic-collapse strength and plateau strength for geometries generated with a SSI process is presented in Figs. 5.14 to 5.16. Due to the near isotropic response of geometries in the range of 0 to 0.8, the mechanical response in the x_1 and x_2 direction has been averaged in Figs. 5.14 to 5.16. Fig. 5.14 shows the increasing trend in the elastic modulus as the geometries are more irregular akin to unfilled Voronoi honeycombs. Hence, a configuration with $\delta = 0$ is ~26% stiffer than a $\delta = 0.8$ configuration.

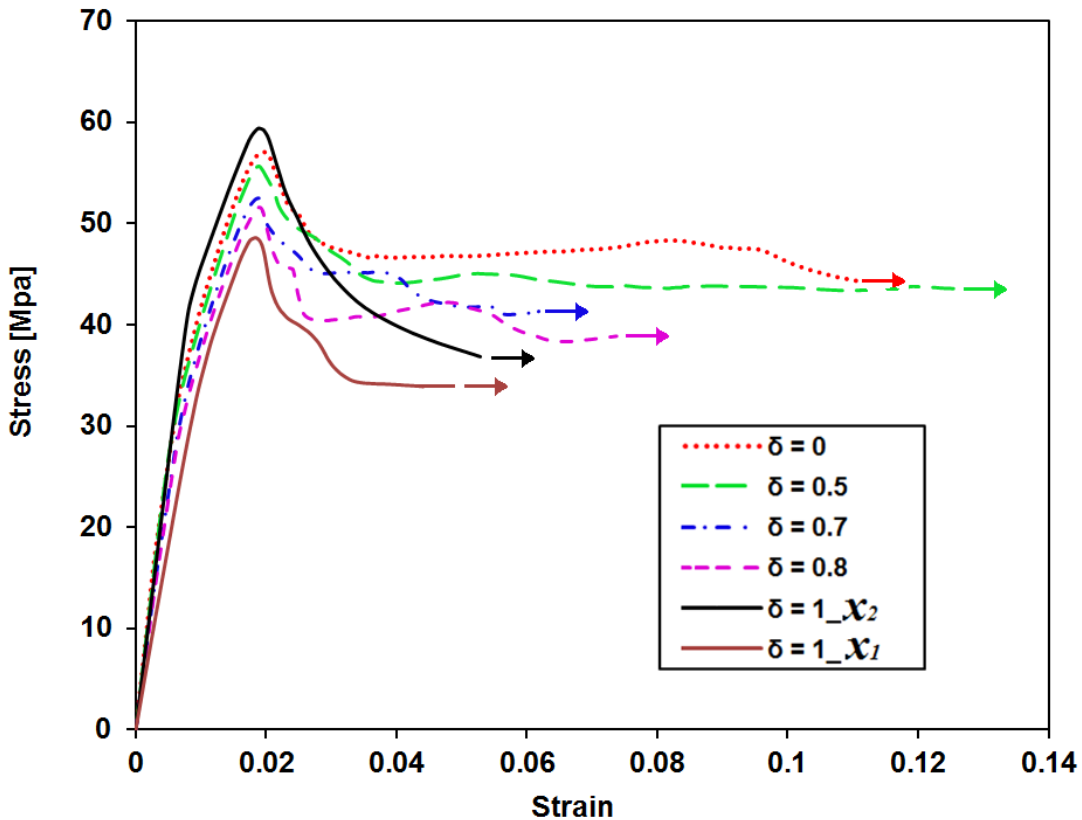


Figure 5.13: Stress-Strain curves of foam-filled Voronoi honeycombs (AL-9% and SF-40) for different regularities.

Unlike unfilled Voronoi honeycombs, Figs. 5.15 and 5.16 suggest an indirect relation between plastic-collapse strength and plateau strength with regularity parameter for foam-filled configurations generated using a SSI process (geometries in the range of 0 to 0.8). Indeed, the plastic-collapse strength of fully irregular configurations is $\sim 10\%$ higher than that for $\delta = 0.8$. Similarly, plateau strength of Voronoi honeycombs with $\delta = 0$ are $\sim 16\%$ higher than the $\delta = 0.8$ counterparts (see Fig. 5.16).

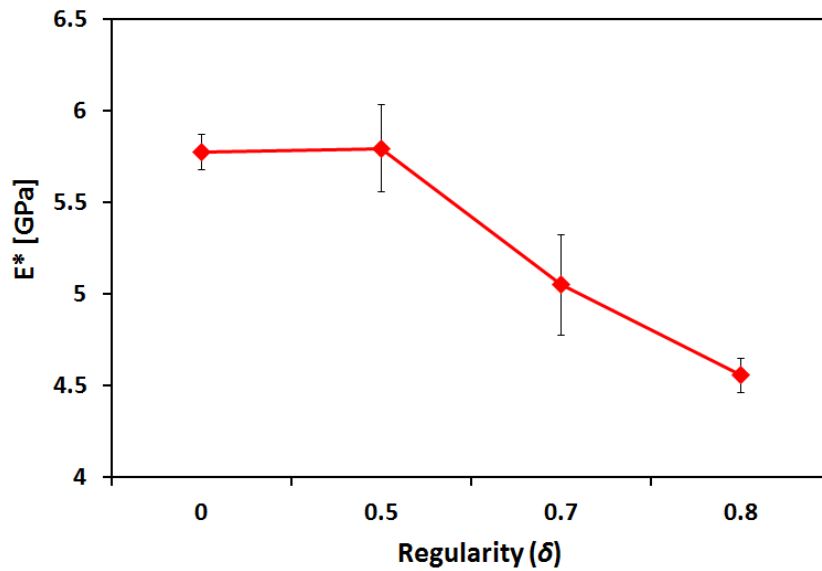


Figure 5.14: Effect of regularity on elastic modulus of foam-filled Voronoi honeycombs generated using SSI process.

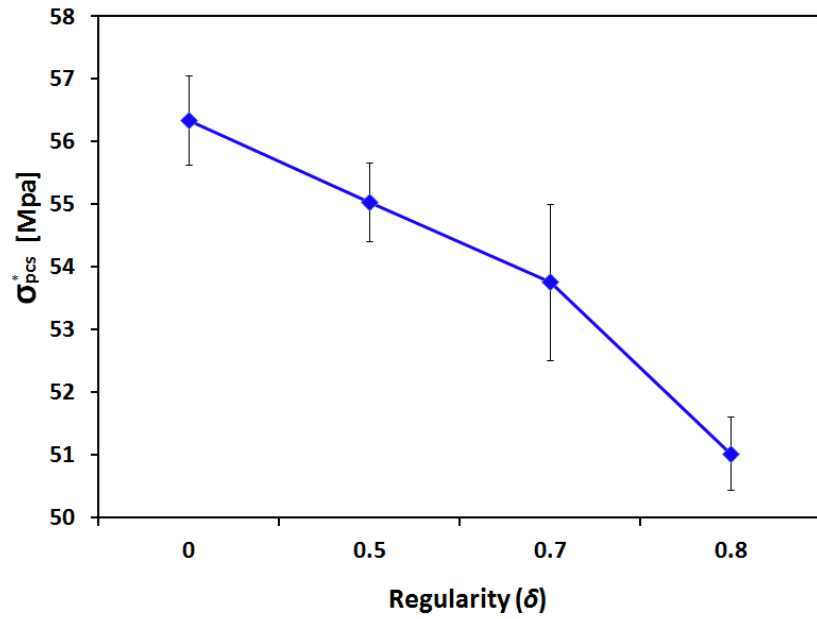


Figure 5.15: Effect of regularity on plastic-collapse strength of foam-filled Voronoi honeycombs generated using SSI process.

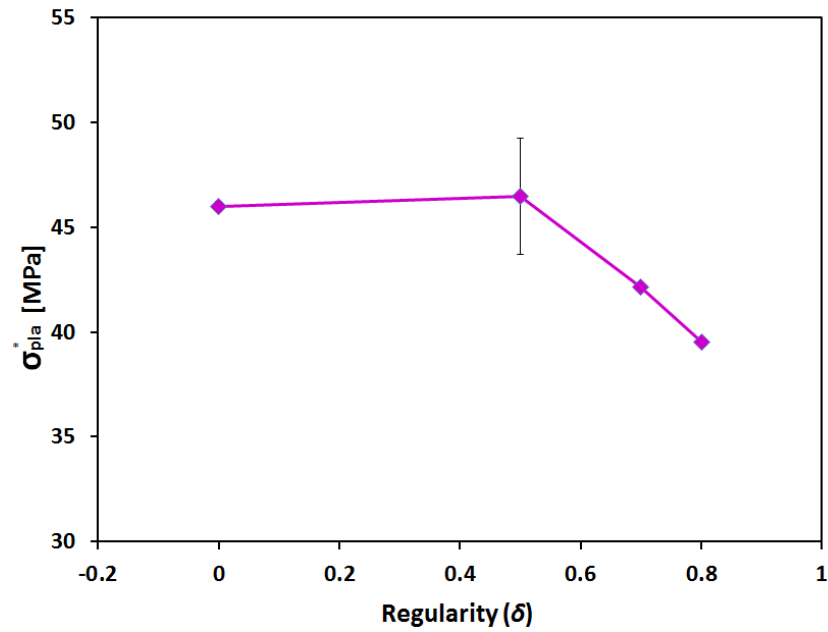


Figure 5.16: Influence of regularity on plateau strength of foam-filled Voronoi honeycombs generated using SSI process.

CHAPTER 6

FINITE ELEMENT MODELING OF 3D VORONOI FOAMS

In chapter 4, the effect of regularity on the compression response of Voronoi honeycombs was analyzed. In that chapter, it was found that a fully random Voronoi honeycomb is stiffer than a regular Voronoi honeycomb at low strains. On the other hand, plastic-collapse and plateau strengths were appreciably higher in regular honeycombs than their irregular counterparts. The conclusions reached in chapter 4 are exclusively applicable to honeycombs (2D) and comparable conclusions should be inferred for 3D foams only after further study. A 2D simulation cannot fully capture the complex interaction between struts in 3D foams. For instance, a 2D simulation successfully captures bending in struts which is an important mode of deformation in foams. However, torsion conjointly present in real experiments [63] cannot be fully captured by a 2D simulation. Hence, a 3D structure can be used to represent foams in order to capture the majority of mechanisms governing deformation in real foams. Periodic simulations of standard unit cells have proven to be an efficient technique to represent foams. Different types of geometries have been proposed as standard unit cells. For instance, cube, tetrahedron, sphere, dodecahedron, rhombic dodecahedron, tetrakaidecahedron are among the ones used as standard unit cells in order to represent foams. The mechanical response is highly dependent on the standard unit cell microstructure, base material properties and the relative density. Among the different standard unit cells, the tetrakaidecahedron has been widely used to represent foams generated from gas bubbles growing in a liquid matrix. A tetrakaidecahedron dry foam captures the majority of the characteristics observed in soap bubbles. For instance, the average number of faces in a cell is 14, the average number of edges per face is ~ 5 . Hence, by making use of a tetrakaidecahedron representation Zhu et al., [64] derived analytical results for estimating the elastic properties of foams as a function of the relative density. However, a

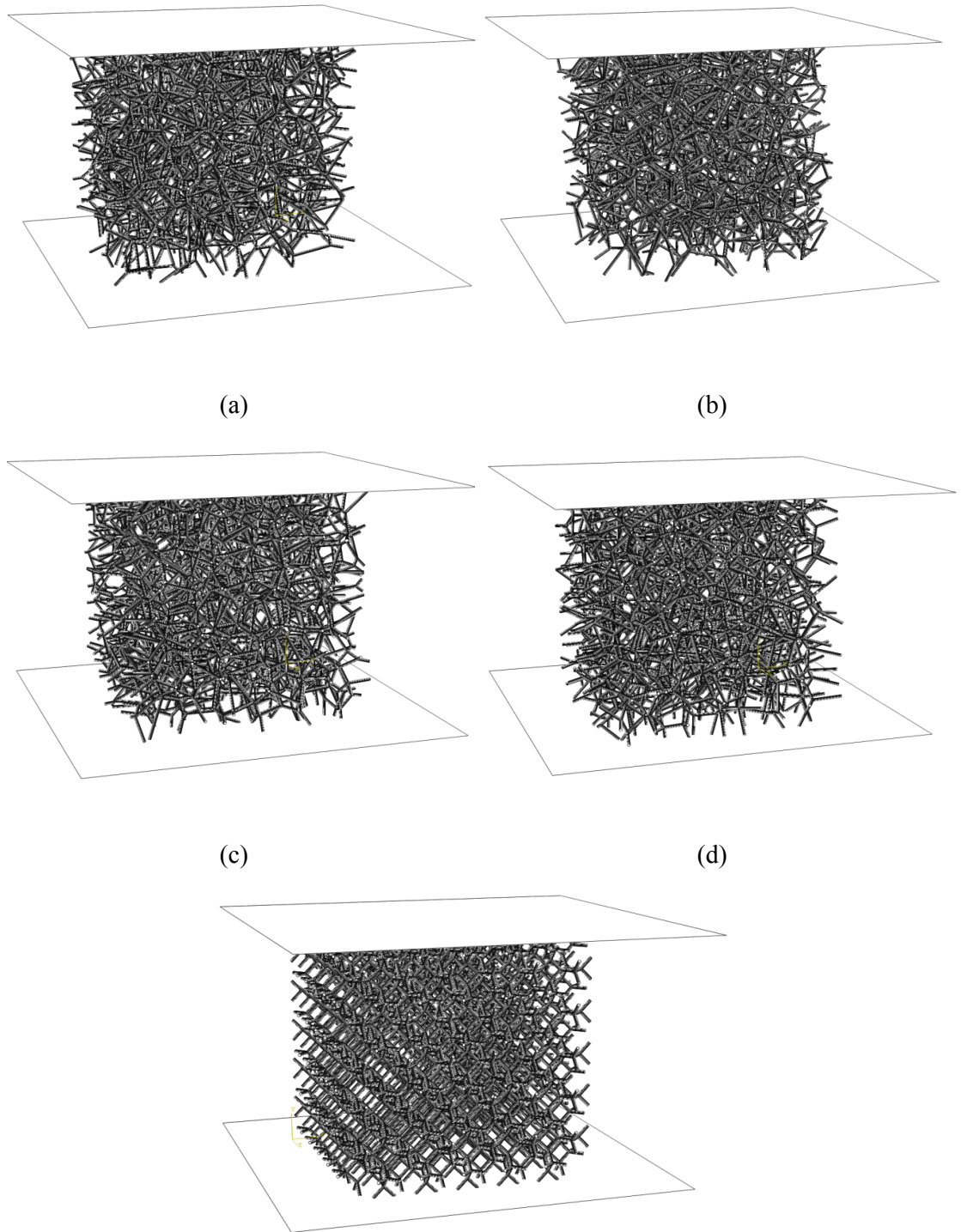
tetrakaidecahedron foam possess characteristics that have not been observed in real foams [23, 65]. For example, the bulk modulus in tetrakaidecahedron foams varies linearly with density while a quadratic variation has been experimentally observed in foams [65]. Moreover, the most common polygon forming the cell faces in real foams has five edges while none of the faces in a tetrakaidecahedron representation has that configuration [23]. Further, most foams are non-periodic; hence, a foam represented with a periodic unit cell does not completely capture the random morphology observed in real foams. In order to better represent foams, the Voronoi approach has been used as an efficient way to represent the majority of features of foams in a 3D space [20, 27, 55, 65]. Most of the research attention is on the dependency of mechanical properties on density. However, a lack of research about the role of regularity of 3D foams is evident. This is partially explained because the density is one of the variables that can be controlled during foam production. On the other hand, controlling the regularity parameter as defined in section 2.1(f) is difficult if not impossible with the current methods of foam production. As explained in chapter 3, the initial step in the process of representing foams with Voronoi diagrams begins with the generation of nuclei in a Euclidean space. In 3D, if nuclei are regularly placed in a face centered arrangement of points, a foam based on a rhombic dodecahedron cell is formed. Alternatively, a tetrakaidecahedron foam is generated if the nuclei are regularly placed in a body centered arrangement of points (see Fig. 2.3 (a)). Random foams are generated if points are randomly generated in a 3D space. The level of randomness as defined in section 2.1(f) has a profound impact on the final shape of the Voronoi foam, akin to the one observed in the 2D case (see Fig. 3.5). A wide distribution of cell sizes is produced if a random distribution of points is used. Eliminating points that are too close reduces the distribution of cell sizes and increases the regularity of the foam (as in the 2D case, see Fig. 3.5). In the most extreme case, all the cells will have the same size. Motivated by the possibility of controlling the

regularity during foam production, it is of particular interest to the present chapter to study the effect of regularity on the compression response of 3D Voronoi foams. Due to the fact that the influence of density has attracted the majority attention of research, geometries with different relative densities in the range of 3% to 9% has also been generated in order to compare with the theoretical and empirical models available in the literature and validate the FE approach. Section 6.1 presents an overview of the key considerations involved during FE modeling, focusing primarily on the FE modeling. For geometry construction details, the reader is referred to chapter 3. The stress-strain curves for different configurations in the regularity range of 0 to 1 and density range of 3% to 9% are presented. In section 6.2, a comparison of the density dependency of the current simulation with theoretical and empirical models available in literature in order to validate the FE approach is made. Finally, the primary interest of the chapter is discussed in section 6.3 where the influence of regularity is analyzed by comparing the results with the 2D cases.

6.1. Finite element modeling

Geometries for 3D space were generated according to the process discussed in chapter 3. An important aspect to be defined is the minimum control volume size relative to cell size of a representative spatial region. In other words, the number of cells that a representative geometry requires in order to accurately simulate a continuum foam. A geometry with only a few cells cannot be considered a representative sample of a continuum foam while computational costs increase exponentially for geometries with a large number of cells. Geometries with cells in the range of 50 to 100 are normally used in the literature (see for instance [65, 66]). A few studies analyze the effect of the specimen size relative to the cell size in the compression response of foams. Among them, Andrews et al., [45] have experimentally studied the effect of the specimen size on the compression response of aluminum foam. They suggest that a ratio of the specimen size to cell size equal to ~ 6

accurately predicts elastic modulus and presents a tolerable difference in the prediction of plastic-collapse strength of aluminum foams. For a tetrakaidecahedron foam, a ratio of the specimen size to cell size equal to 6 corresponds to $n = 559$ nucleus points and 341 cells as explained in section 3.3(a). Thus, $n = 559$ was used to generate geometries in 3D space through a SSI process for the same regularity parameters studied in chapters 4 and 5 ($\delta = \{0, 0.5, 0.7, 0.8\}$). Additionally, a geometry with $n = 559$ nuclei arranged in a regular body centered arrangement ($\delta = 1$) was generated through the process described in section 3.3. Only dry configurations were required to model Voronoi foams. Hence, the flowchart presented in Fig. 3.2 was executed until the level “d”. Geometries were then imported from AutoCAD to Abaqus® through *.iges files. The geometries were the basis for creating 3D deformable wire structures in Abaqus®. Plates of thickness equal to 1% of the sample size were added as the top and bottom to simulate sandwich structural configurations. The imported geometries into Abaqus® are shown in Fig. 6.1 rendering the beam profiles for the case of $\bar{\rho} = 3\%$. The material model used for the aluminum base material had the same characteristics as the 2D case (see Fig. 4.2).



(e)
 Figure 6.1: Geometry of 3D Voronoi foams for: (a) $\delta = 0$, (b) $\delta = 0.5$, (c) $\delta = 0.7$, (d) $\delta = 0.8$, (e) $\delta = 1$.

Next, a beam section with a solid circular profile was assigned to all the line features created. As explained in chapter 3, cross-section of all the struts is idealized to be circular although in reality the diameter varies along the length [20]. Such an idealization is acceptable for relative densities below 10% [55]. Moreover, as established by Zhu et al. [27], the value of the strut area (A_i) depends on the density of the foam. Hence, in 3D it can be estimated by,

$$\bar{\rho} = \rho^* / \rho_s = \left(\frac{1}{V}\right) \sum_{i=1}^N A_i l_i$$

where $\bar{\rho}$ is the relative density of the foam, ρ^* is the density of the cellular material, ρ_s the density of the solid, N the number of struts, A_i the cross sectional area of struts, l_i the cell wall length and V the control volume. The sum of all the ligament lengths of the Voronoi foam can be evaluated in AutoCAD through the transformation of lines into a single polyline. The properties of the polyline stored the information of the total length. Hence, the thickness of struts (or diameter of circular sections) can be calculated. The corresponding results are presented in Table 6.1. As observed in the Table 6.1, the variation of thickness is relatively small for a given value of relative density. The variation is essentially a consequence of length differences.

Nonlinear effects due to large deformations are activated in a general static analysis performed in ABAQUS/Standard module. Moreover, unstable nonlinear problems require an adaptive automatic stabilization scheme [10, 57]. Values of 2×10^{-4} and 0.05 for dissipated energy fraction and ratio of stabilization energy to strain energy are used by default in ABAQUS/Standard. Furthermore, the number of attempts per increment is set to 10 and the allowable time increment is reduced to $1 \times 10^{-8} s$ for stabilizing the simulation.

Relative density ($\bar{\rho}$)	Regularity (δ)	Strut area (A_i [m ²])	Strut diameter (d_i [m])
9%	0	1.1425×10^{-8}	1.2061×10^{-4}
	0.5	1.1346×10^{-8}	1.2019×10^{-4}
	0.7	1.1818×10^{-8}	1.2267×10^{-4}
	0.8	1.2065×10^{-8}	1.2394×10^{-4}
	1	1.3161×10^{-8}	1.2945×10^{-4}
7%	0	8.8861×10^{-9}	1.0637×10^{-4}
	0.5	8.8249×10^{-9}	1.0600×10^{-4}
	0.7	9.1915×10^{-9}	1.0818×10^{-4}
	0.8	9.3840×10^{-9}	1.0931×10^{-4}
	1	1.0236×10^{-8}	1.1416×10^{-4}
5%	0	6.3473×10^{-9}	8.9898×10^{-5}
	0.5	6.3035×10^{-9}	8.9587×10^{-5}
	0.7	6.5653×10^{-9}	9.1429×10^{-5}
	0.8	6.7028×10^{-9}	9.2381×10^{-5}
	1	7.3115×10^{-9}	9.6485×10^{-5}
3%	0	3.8084×10^{-9}	6.9634×10^{-5}
	0.5	3.7821×10^{-9}	6.9394×10^{-5}
	0.7	3.9392×10^{-9}	7.0821×10^{-5}
	0.8	4.0217×10^{-9}	7.1558×10^{-5}
	1	4.3869×10^{-9}	7.4737×10^{-5}

Table 6.1: Struts properties for different configurations of Voronoi honeycombs.

As observed in the 2D case, the contact interaction between ligaments begins at a strain $\sim 10\%$ (see Fig. 4.5 to 4.9). Due to the fact that the interactions between the whole set of ligaments cannot be automatically simulated in Abaqus/Standard, confidence in the results presented is considered accurate up to $\sim 10\%$.

In the 2D simulation, a displacement boundary condition is applied to the top surface while the bottom surface was constrained for displacement in the x_2 direction. For the 3D case, the top and bottom surfaces were displaced equally in order to maintain symmetry during simulation. Similar to the 2D case, one point in the center of the top and bottom surfaces was restrained for displacement in the plane perpendicular to the displacement applied.

A 3-node spatial beam with six degrees of freedom per node and a quadratic interpolation within the domain were selected for FE discretization. Three translational degrees of freedom and three rotational degrees of freedom are the active degrees of freedom in the nodes. Beam elements are suitable for simulating geometries with one of the dimensions significantly greater than the other two [57]. The elements are identified as B32 in Abaqus® where ‘B’ stands for beam, the ‘3’ indicates the dimensionality, and the ‘2’ indicates the interpolation formulation (quadratic in this case). B32 elements base their formulation on Timoshenko’s beam theory, so they take into account shear deformation which is significant in short beams. The number of elements per wall needs to be sufficiently small in order to assure convergence, but sufficiently high to minimize the creation of extremely short ligaments due to the fact that short ligaments cannot be accurately modeled using beam elements. Hence, two elements per edge were used for meshing. Additionally, the top and bottom plates were discretized with four node shell elements discretized in such a way that nodes in the beams coincide with nodes of the shells. The number of elements in a typical simulation was in the range of 11114 to 11860.

In the processing stage, simulations were run as a batch job in a parallel processing environment. The Samuel Ginn College of Engineering High Performance Computer Cluster (HPCC) was used for this purpose.

In the post-processing stage, the reaction forces on the top and bottom surface of the model were added in order to get the total reaction force (F). The average stress over the Voronoi foam was obtained as a ratio of the force (F) to the apparent area of the sample. Next, in order to get the average strain of the sample, displacements of the top and bottom surface (α) was divided by the length of the control volume (H). All these calculations were

accomplished for every load increment in order to get continuous curves. Results for Voronoi foams with $\bar{\rho} = \{9\%, 7\%, 5\%, \text{ and } 3\%\}$ are presented in section 6.2 (see Fig. 6.2 to 6.9) and a comparison of critical characteristics for different densities and regularities are presented in Fig. 6.11 to 6.16. Validation of results have been performed by comparing simulation of Al Voronoi foams with analytical and empirical models available in literature and are presented in section 6.3.

6.2. Results

In the present section, results for 3D Voronoi foams with $\bar{\rho} = \{9\%, 7\%, 5\%, 3\%\}$ displacement controlled loading in the x_2 direction are depicted in Figs. 6.2 to 6.9. In order to make the results more useful, the stress is normalized by the yield stress of the solid material (σ_{ys}) and $\bar{\rho}^{1.5}$. Hence, the formula for calculating the reduced stress $\bar{\sigma}$ is,

$$\bar{\sigma} = \frac{\sigma}{\sigma_{ys} \cdot \bar{\rho}^{1.5}}$$

The quantity $\bar{\rho}^{1.5}$ is used for normalization due to the fact that the foam strength scales with $\bar{\rho}^{1.5}$ as shown in section 6.3. Results presented in Figs. 6.2 to 6.9 show that the simulations are able to capture the two initial regimes (elastic and plateau regions). Regarding the elastic regimes, all the configurations exhibit a nearly linear variation whose slope depends on regularity and density although the normalization process has reduced dependency on density. The variation in the elastic modulus for different regularities is analyzed in section 6.4. In the transition from the elastic to plastic regime, the drop observed after the plastic-collapse strength seems to be more dramatic for the regular configurations with $\delta = 1$, as in Figs. 6.3, 6.5, 6.7 and 6.9. In the plastic region, the oscillations of 2D analysis are less evident in the 3D simulation. This is attributed to the absence of interaction among ligaments

beyond ~10% strain in 3D simulations. Thus, simulations beyond that value have not been attempted.

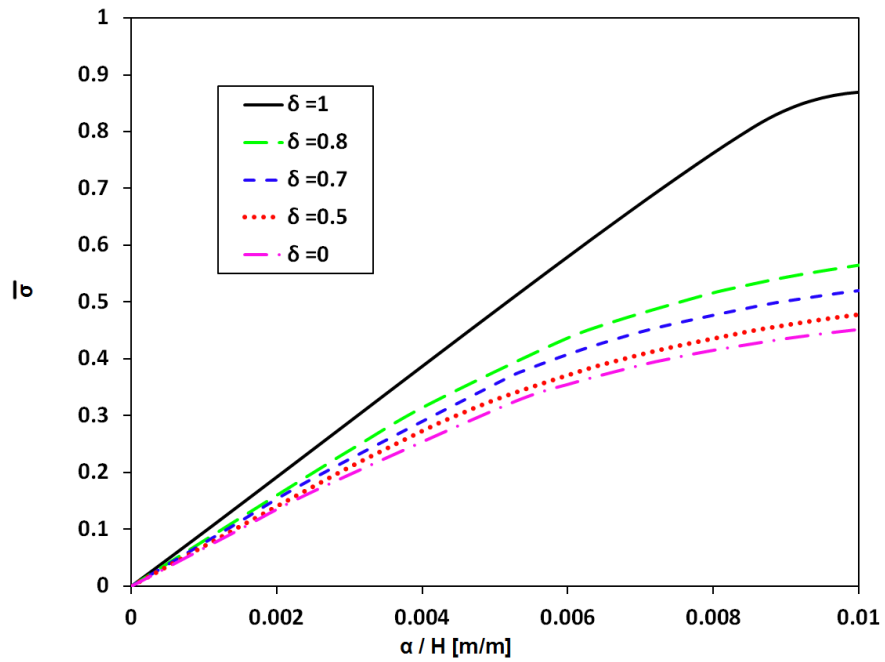


Figure 6.2: 3D Al Voronoi foam response with $\bar{\rho} = 9\%$ for different regularities.

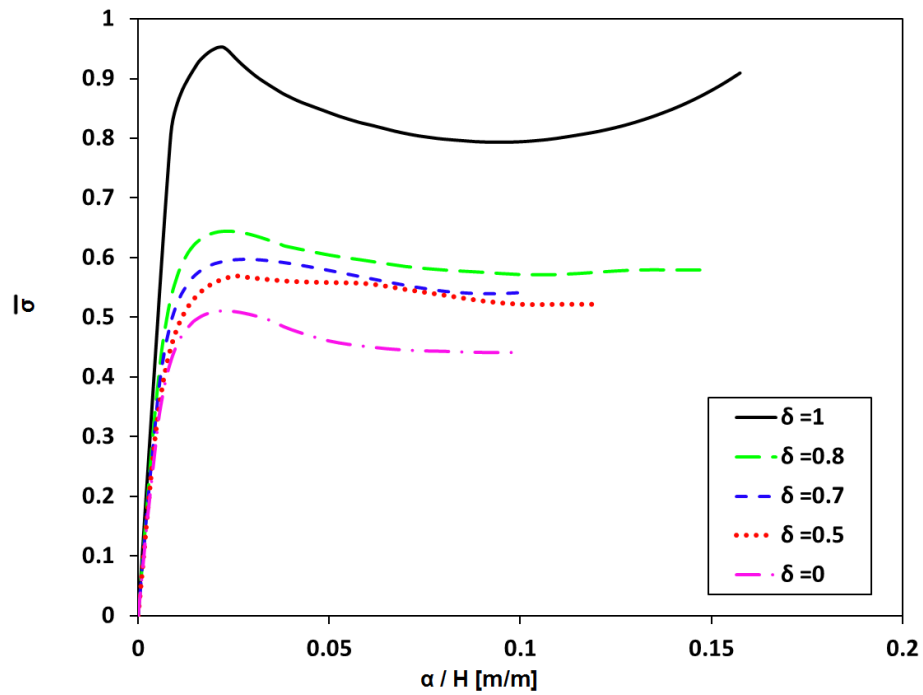


Figure 6.3: 3D Al Voronoi foam response with a $\bar{\rho} = 9\%$ for different regularities.

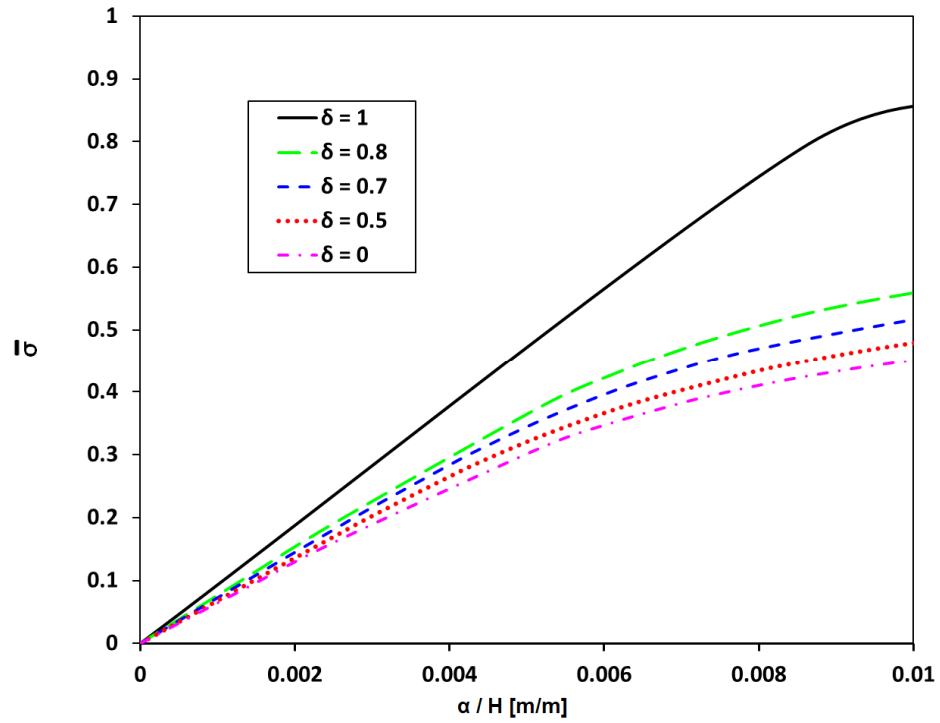


Figure 6.4: 3D Al Voronoi foams response with $\bar{\rho} = 7\%$ for different regularities.

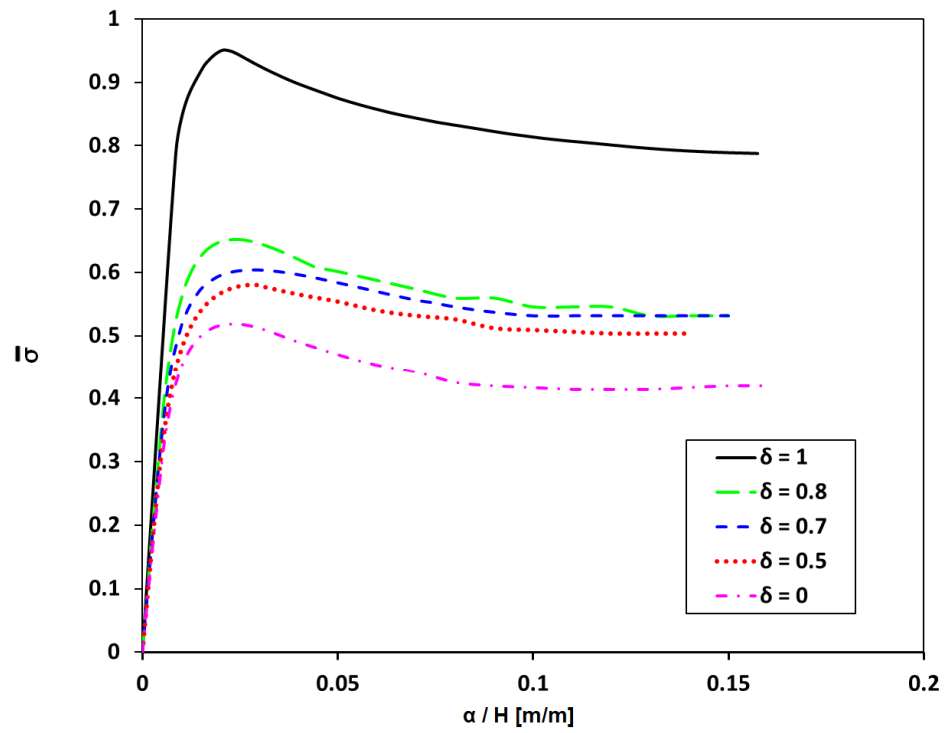


Figure 6.5: 3D Al Voronoi foams response with $\bar{\rho} = 7\%$ for different regularities.

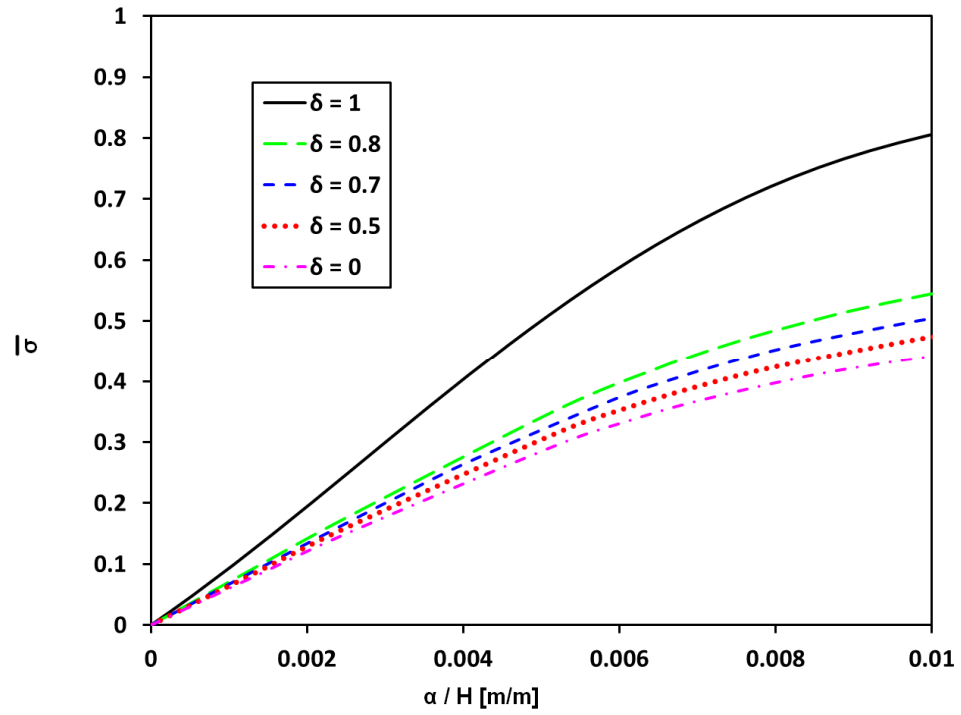


Figure 6.6: 3D Al Voronoi foams response with $\bar{\rho} = 5\%$ for different regularities.

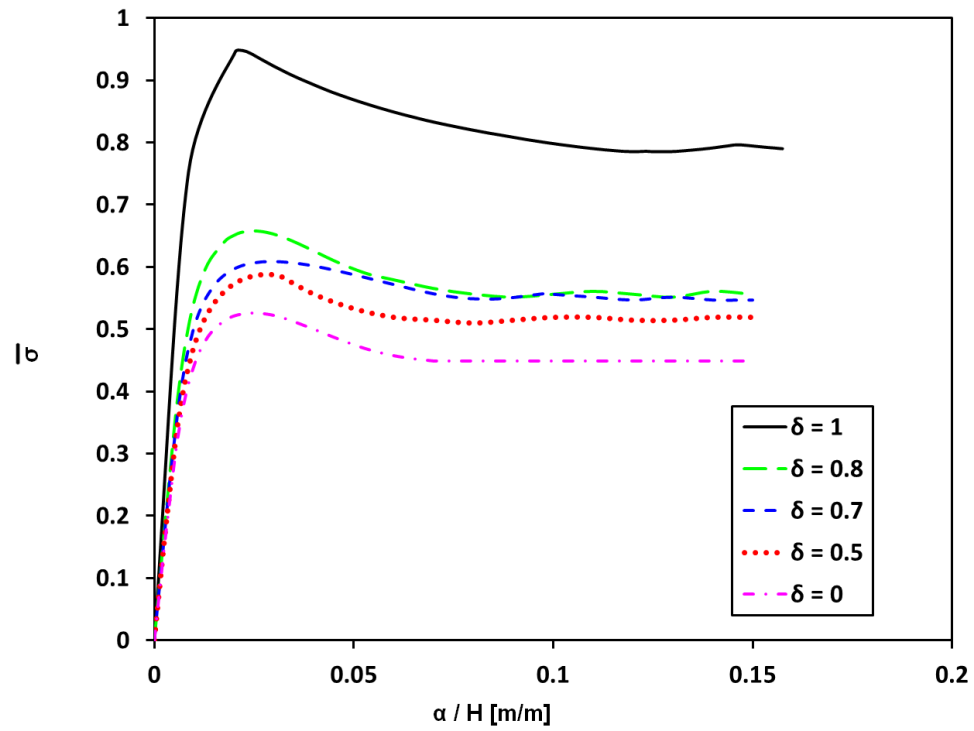


Figure 6.7: 3D Al Voronoi foams response with $\bar{\rho} = 5\%$ for different regularities.

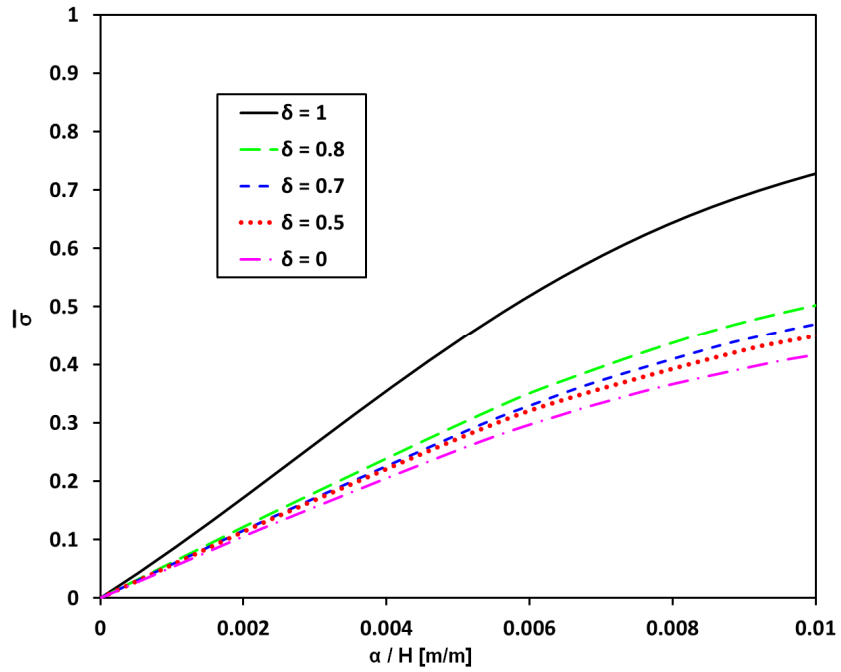


Figure 6.8: 3D Al Voronoi foams response with $\bar{\rho} = 3\%$ for different regularities.

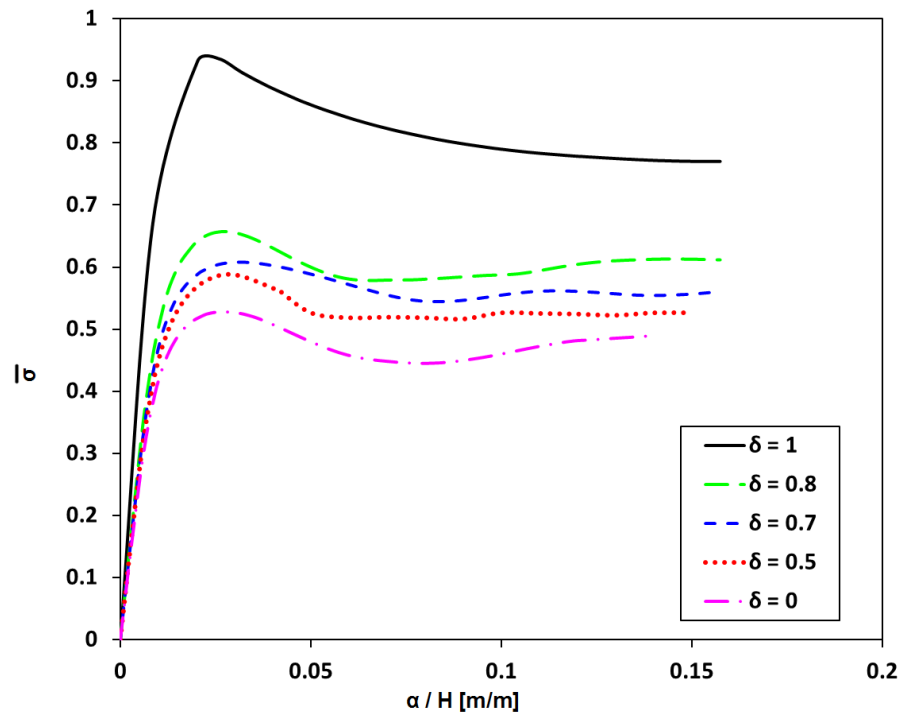
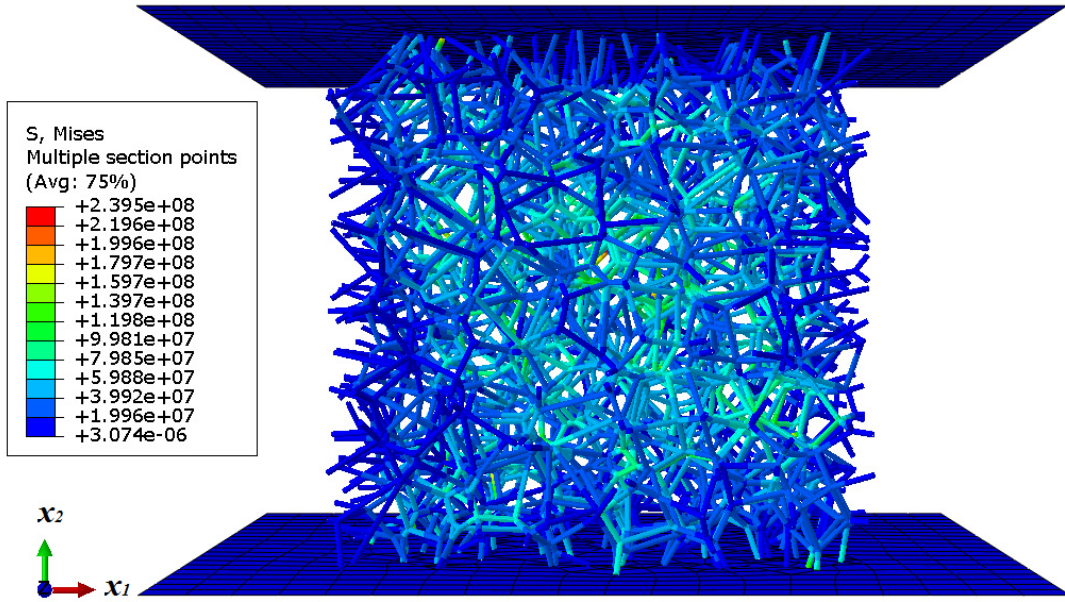
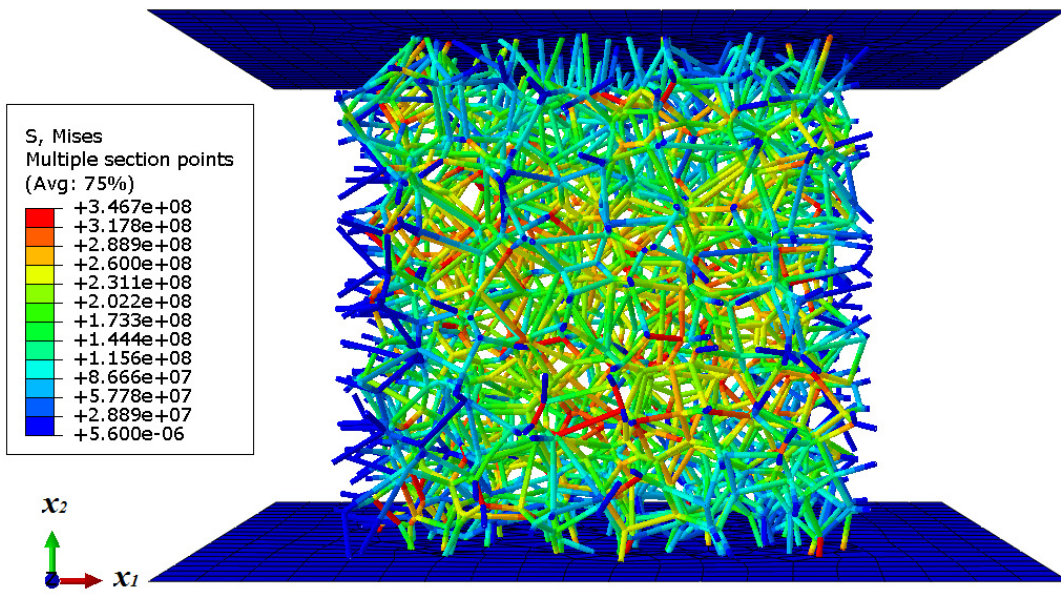


Figure 6.9: 3D Al Voronoi foams response with $\bar{\rho} = 3\%$ for different regularities.

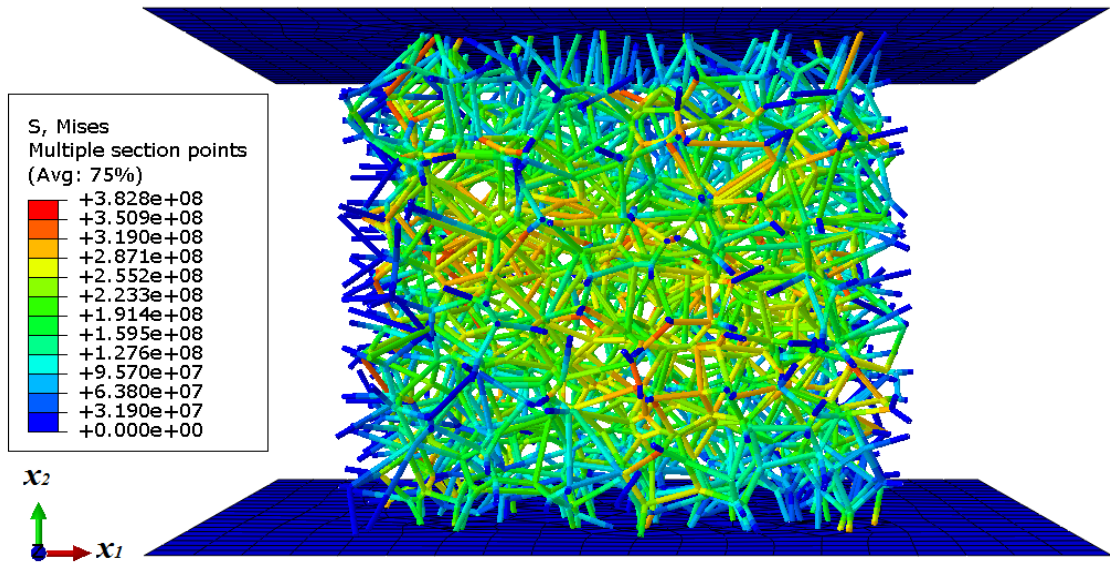
Additionally, the deformed models at four points of interest on the stress-strain curve are shown in Fig. 6.10. First, the elastic response does not show any localization of deformations or barreling of the sample. Ligaments subjected to high levels of stress are located randomly but uniformly in the control volume, as observed in Fig. 6.10. Hence, a random elimination of ligaments has a profound impact on the reduction of effective mechanical properties of foams as observed by Silva and Gibson [14]. On the other hand, ligaments that are located near the border of the control volume are not subjected to high levels of stress. Next, when the plastic-collapse strength is reached, a drop in the stress-strain curve is observed. Subsequently, the deformation begins to localize when the weakest cell of the Voronoi foam collapses. There is a tendency for the first collapsing cell to be localized in the center of the sample although it can vary due to the random morphology of the structure. In 2D, the deformation was localized in a path that was nearly horizontal while in 3D the path can be visualized as a surface. The collapsing surface tends to be nearly horizontal, but not planar, passing through the first collapsed cell. The instability originated by the first collapsed surface causes a collapse in the neighboring cells localizing the deformation close to the original surface. The levels of stress in the face sheets are negligible compared to the stress in the Voronoi foams as shown in Fig. 6.10.



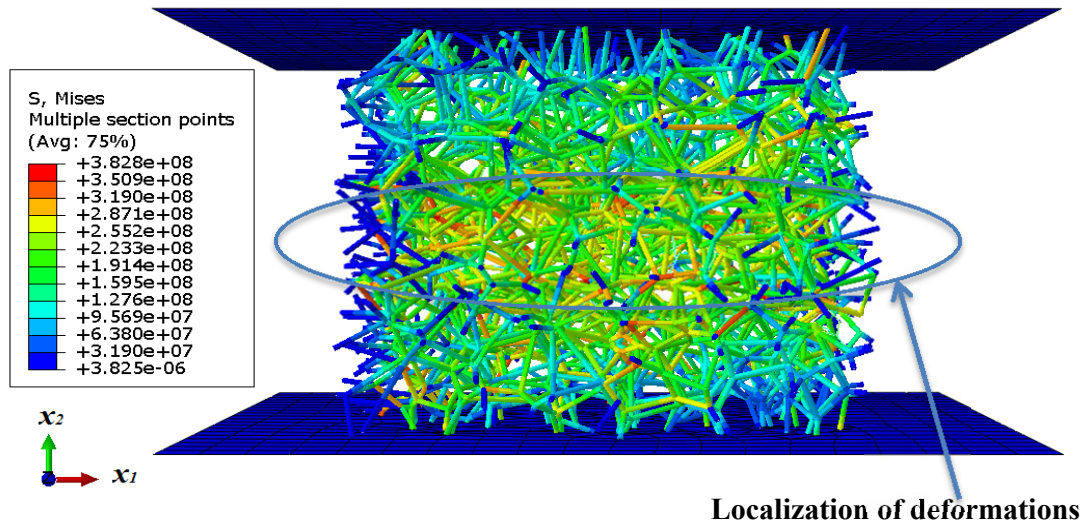
(a)



(b)



(c)



(d)

Figure 6.10: Von Mises stress contour of AL Voronoi foam with $\delta = 0.7$ and $\bar{\rho} = 3\%$ for applied strains of: (a) 1.35%, (b) 2.05%, (c) 8.01%, (d) 15.75%. (units of stress in the color bar are in Pa)

6.3. The effect of relative density

Due to the fact that density is one of the factors that can be controlled during foam production, empirical and analytical studies of the effect of relative density on the elastic response of foams are available in the literature [2, 64, 67]. Hence, the results presented in section 6.2 are compared to analytical and empirical results available in the literature for validation purposes. By making use of a tetrakaidecahedron representation, Zhu et al., [64] derived analytical results for estimating the elastic properties of foams as a function of the relative density. The result for the elastic modulus for the case of foams with a circular cross section as the ones simulated in the present thesis is,

$$\frac{E^*}{E_s} = \frac{3}{5} \frac{\left(\frac{\rho^*}{\rho_s}\right)^2}{\left(1 + 0.9 \frac{\rho^*}{\rho_s}\right)}$$

At low relative densities, a quadratic variation of the elastic modulus with relative density is characteristic of foams where bending is the dominating mechanism while a linear variation is characteristic of stretch-dominated structures [68]. For instance, a stretch-dominated foam can be built with a tetrahedron as a unit base instead of a tetrakaidecahedron as described in [69] or by another unit cell that satisfies Maxwell's criterion of static determinacy [70]. Another model for estimating the elastic properties of open cell foams has been proposed by Warren et al., [67]. In their approach a unit structure formed by struts joining the centroid of a tetrahedron with its vertices was used in order to maintain the 109.5° edge connectivity. Their result for estimating the elastic modulus is,

$$\frac{E^*}{E_s} = \frac{C1 \cdot \bar{\rho}^2 \cdot (11 + 4 \cdot C1 \cdot \bar{\rho})}{10 + 31 \cdot C1 \cdot \bar{\rho} + 4 \cdot C1^2 \cdot \bar{\rho}^2}$$

with $\bar{\rho} = \rho^*/\rho_s$ and $C1 \approx 0.827$ for the case of circular cross sections.

The relation of elastic properties with relative density has not only been studied analytically but experimentally. Gibson and Ashby [2] described approximately the data obtained for different foams with the formula,

$$\frac{E^*}{E_s} = C2 \left(\frac{\rho^*}{\rho_s} \right)^2$$

where $C2 \approx 1$ for the case of open cell foams.

Dependency on relative density for results presented in section 6.2 is depicted in Fig. 6.11 along with analytical and empirical theories.

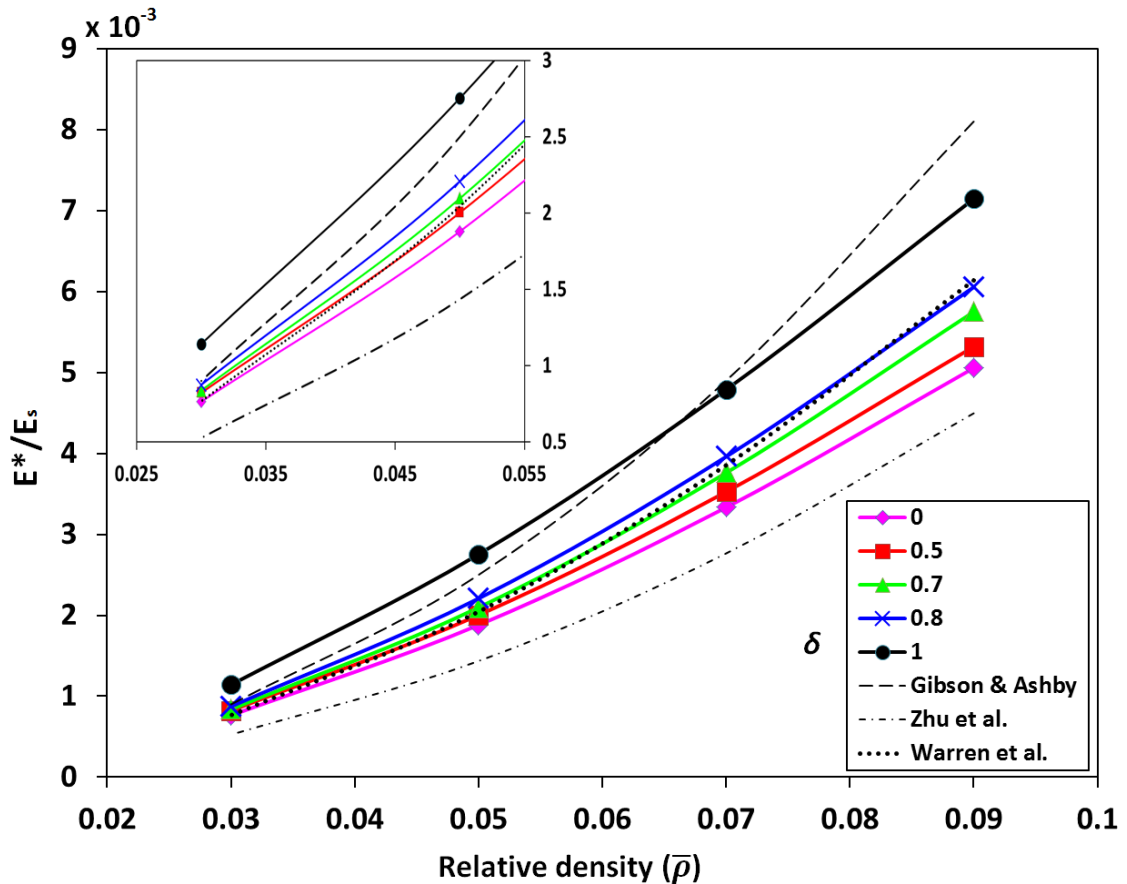


Figure 6.11: Variation of elastic modulus of 3D Voronoi foams with relative density for different regularities.

Numerical simulations show that the elastic modulus scales with a second order polynomial in agreement with experimental and analytical results available in the literature.

Table 6.2 fits the data to a curve of the form,

$$\frac{E^*}{E_s} = C3 \left(\frac{\rho^*}{\rho_s} \right)^2 + C4 \left(\frac{\rho^*}{\rho_s} \right)$$

Regularity	C3	C4	Coefficient of determination
0	0.4826	0.01308	0.9992
0.5	0.4959	0.01483	0.9991
0.7	0.5682	0.01312	0.9993
0.8	0.5998	0.01370	0.9992
1	0.6392	0.02243	0.9989

Table 6.2: Elastic modulus data fitting for Voronoi foams with different regularities.

As shown in Fig. 6.11, simulations are roughly bounded between Gibson and Zhu theories although Zhu's results are consistently lower relative to our simulations in the range of densities presented. Moreover, assuming that metal foams produced with the currently available methods have a regularity in the range of $\delta = \{0.7 \text{ to } 0.8\}$, the theory presented by Warren et al., [67] present good agreement with our simulations for $\delta = \{0.7 \text{ to } 0.8\}$. A good prediction of Warren et al., [67] theory with other FE results has also been reported previously by Roberts and Garboczi [65].

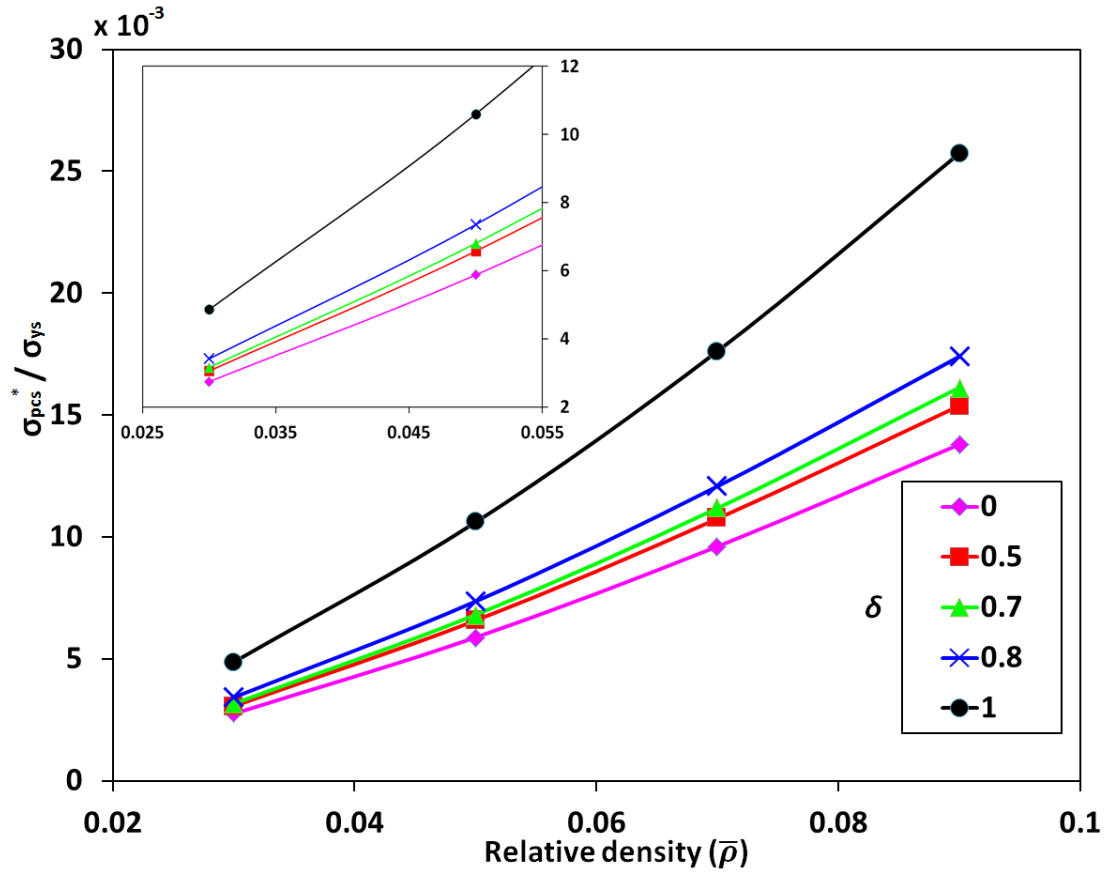


Figure 6.12: Plastic-collapse strength vs. relative density for different regularities.

Similarly, numerical simulations of Voronoi foams show that the plastic-collapse strength depends on $(\rho^*/\rho_s)^{1.5}$ as observed experimentally [68]. Table 6.3 fits the data to a curve of the form,

$$\frac{\sigma_{pcs}^*}{\sigma_{ys}} = C5 \left(\frac{\rho^*}{\rho_s} \right)^{1.5}$$

Regularity	C5	Coefficient of determination
0	0.5150	0.9995
0.5	0.5750	0.9993
0.7	0.6005	0.9998
0.8	0.6482	0.9997
1	0.9516	1

Table 6.3: Plastic-collapse strength data fitting for 3D Voronoi foams with different regularities.

Plateau strength results are also presented in Fig. 6.13. These results should be handled with caution because the interaction between ligaments has not been simulated in 3D Voronoi foams.

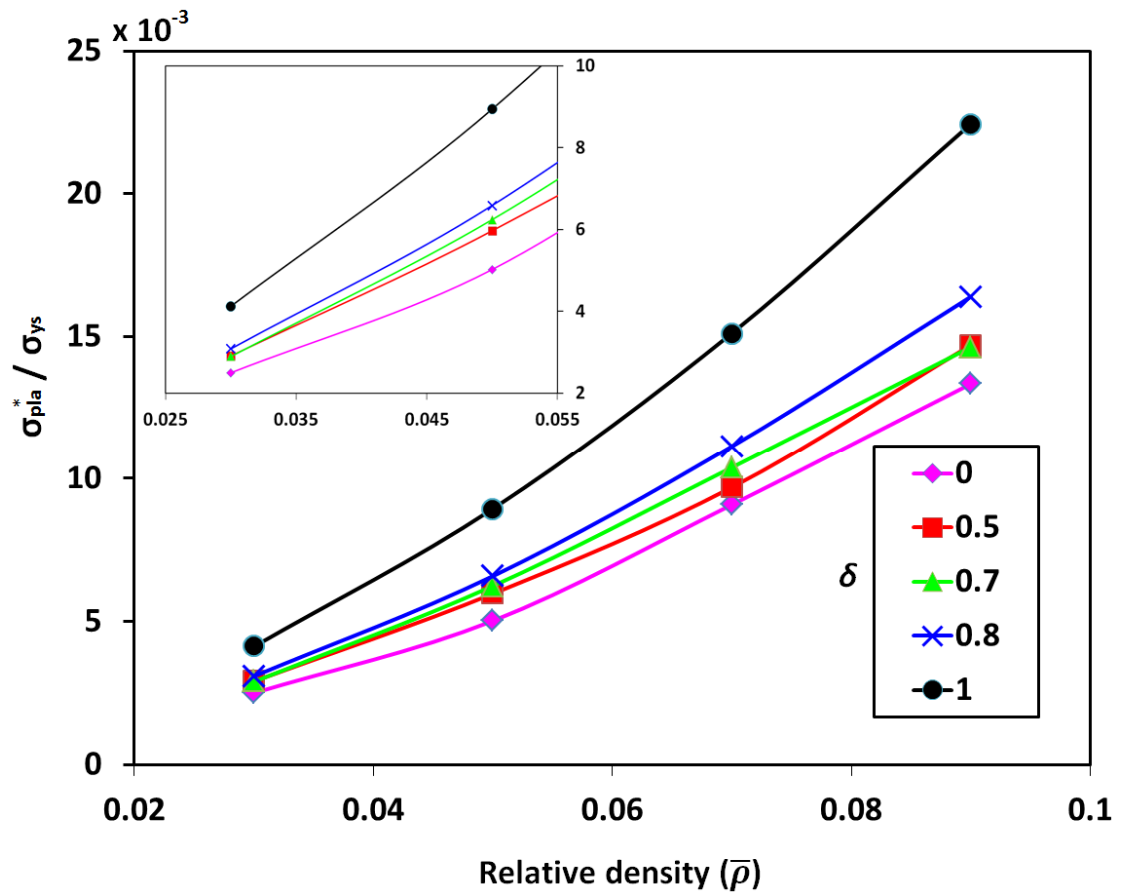


Figure 6.13: The plateau strength variation with relative density for different regularities.

6.4. Role of regularity

In the present section the focus is on the role of regularity on the compression response of Voronoi foams. Figure 6.14 reports the relative elastic modulus of 3D Voronoi foams as a function of regularity used during generation of the structure. The four relative densities used ($\bar{\rho} = \{9\%, 7\%, 5\% \text{ and } 3\%\}$) are depicted in the same graph for comparison. In contrast to the 2D case, a stiffening response is observed as the regularity increases. Data suggests that a regular Voronoi foam is $\{41.3\%, 43.7\%, 46.5\% \text{ and } 49.5\%\}$ stiffer than a fully irregular counterpart for $\bar{\rho} = \{9\%, 7\%, 5\% \text{ and } 3\%\}$, respectively. Further, as can be observed in the Fig. 6.14, the regularity has a modest effect on the relative elastic modulus for geometries in the range of $\delta = \{0 \text{ to } 0.7\}$. Approximately, the improvement in the range of 0 to 0.7 is only $\sim 12\%$. However, regularity has a profound effect in Voronoi foams in the range of $\delta = \{0.7 \text{ to } 1\}$ with the remaining $\sim 30\%$ improvement gained in this range.

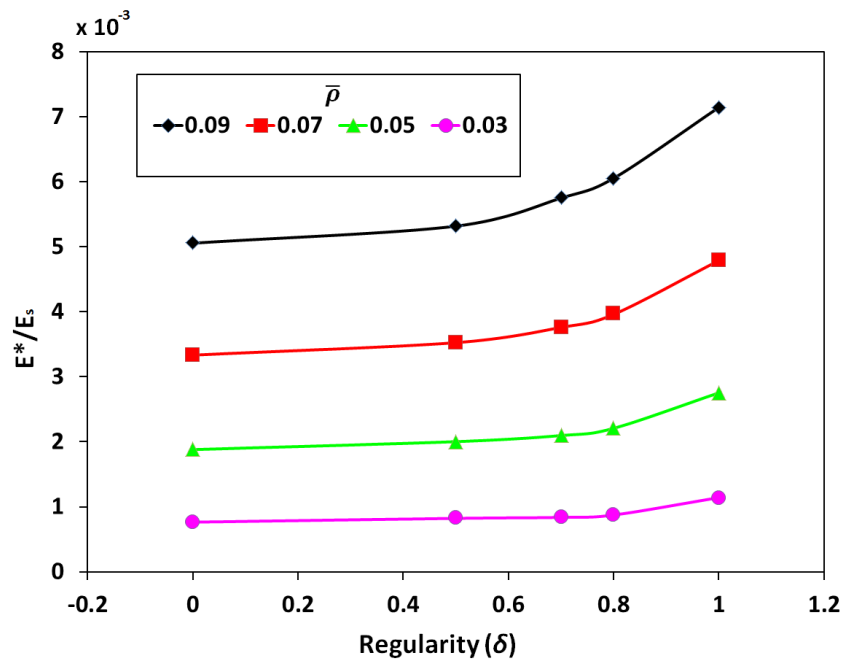


Figure 6.14: Effect of regularity on elastic modulus of 3D Voronoi foams of different relative densities.

Likewise, Figure 6.15 shows the effect of regularity on plastic-collapse strength for different 3D Voronoi foams. Data indicate an increasing trend in the plastic-collapse strength as the regularity increases. The fact that the strength of a tetrakaidecahedron foam is significantly higher than a random foam has also been suggested Zhu et al., [17] although with a linear elastic assumption of the base material. Figure 6.15 also suggests a sharp rise when regularity is more than 0.7, self-evident for higher densities.

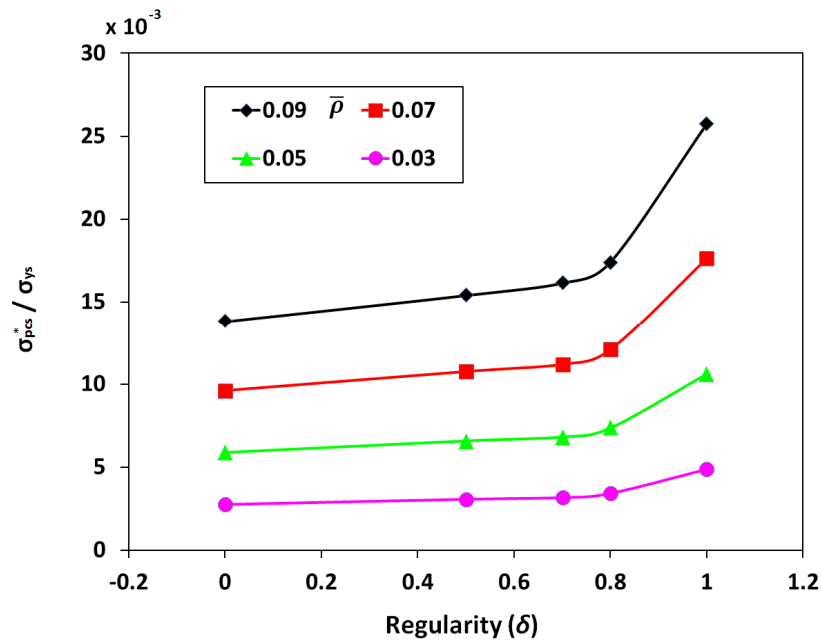


Figure 6.15: Effect of regularity on plastic-collapse strength of 3D Voronoi foams for different relative densities.

Plateau strength results are also presented in Fig. 6.16 although results should be handled with caution since interaction between ligaments has not been simulated in 3D Voronoi foams simulations.

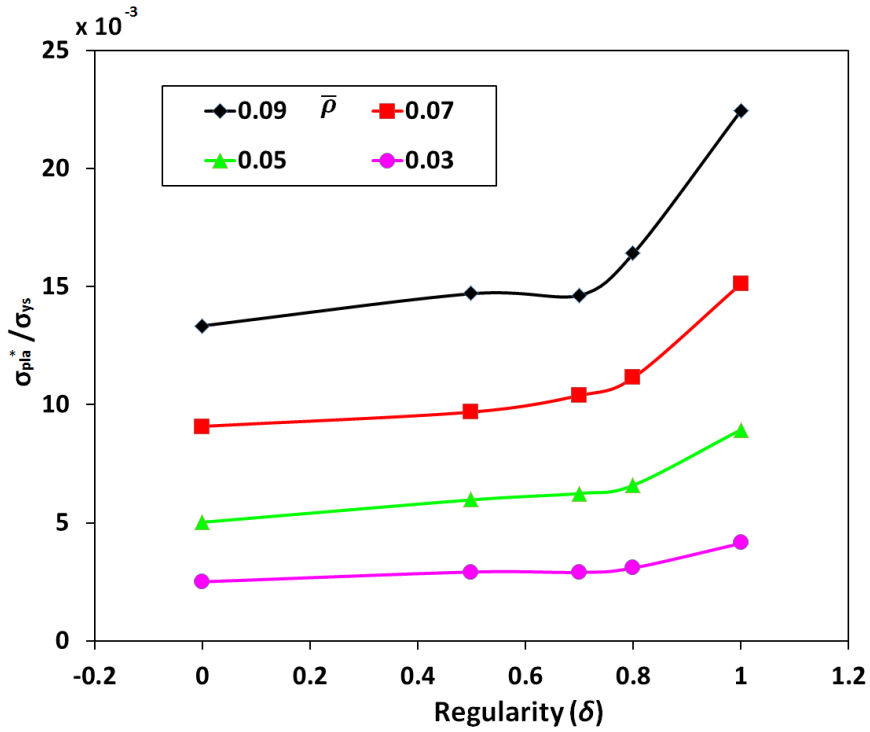


Figure 6.16: Influence of regularity parameter on plateau strength of 3D Voronoi foams of different relative densities.

6.5. Highly regular foams

Figures 6.15 and 6.16 suggest a need for additional analysis in the range of $\delta = \{0.8$ and $1\}$. However, generating geometries with a SSI process in the mentioned range is improbable and computationally expensive. Hence, highly regular configurations were generated with a perturbation process described in section 3.3(b). Three geometries with regularities $\delta = \{0.8, 0.95$ and $1\}$ were generated. The dry foams are shown in Fig. 3.11. Due to the fact that the pattern of points used to create the Voronoi foams of highly regular foams was based on a different process (perturbation process instead of SSI process), the results for highly regular foams are presented separately. Simulations were carried out by varying the diameter of the circular cross sections in order to represent foams of densities $\bar{\rho} = \{9\%$, 7% ,

5% and 3%}. The diameters of the struts for the different configurations are presented in Table 6.4.

Relative density ($\bar{\rho}$)	Regularity (δ)	Strut diameter (d_i [m])
9%	0.8	1.2778×10^{-4}
	0.95	1.2832×10^{-4}
	1	1.2945×10^{-4}
7%	0.8	1.1269×10^{-4}
	0.95	1.1316×10^{-4}
	1	1.1416×10^{-4}
5%	0.8	9.5242×10^{-5}
	0.95	9.5640×10^{-5}
	1	9.6485×10^{-5}
3%	0.8	7.3774×10^{-5}
	0.95	7.4008×10^{-5}
	1	7.4737×10^{-5}

Table 6.4: Struts properties for different configurations of Voronoi honeycombs.

The stress-strain response of the geometries with $\delta = \{0.8, 0.95 \text{ and } 1\}$ in the density range $\bar{\rho} = \{9\%, 7\%, 5\% \text{ and } 3\%\}$ is shown in Fig. 6.17 to 6.20. The general trend observed in section 6.4 is observed for highly regular foams also. Additionally, it can be inferred from Fig. 6.17 to 6.20 that a small perturbation ($\delta = 0.95$) in a tetrakaidecahedron configuration has a desirable effect because the mechanical response is more controlled with comparable mechanical properties. That is, the abrupt collapse observed in regular foams is significantly mitigated by the small perturbation introduced with tolerable effects in elastic modulus and plastic-collapse strength, as shown in Fig. 6.17 to 6.20.

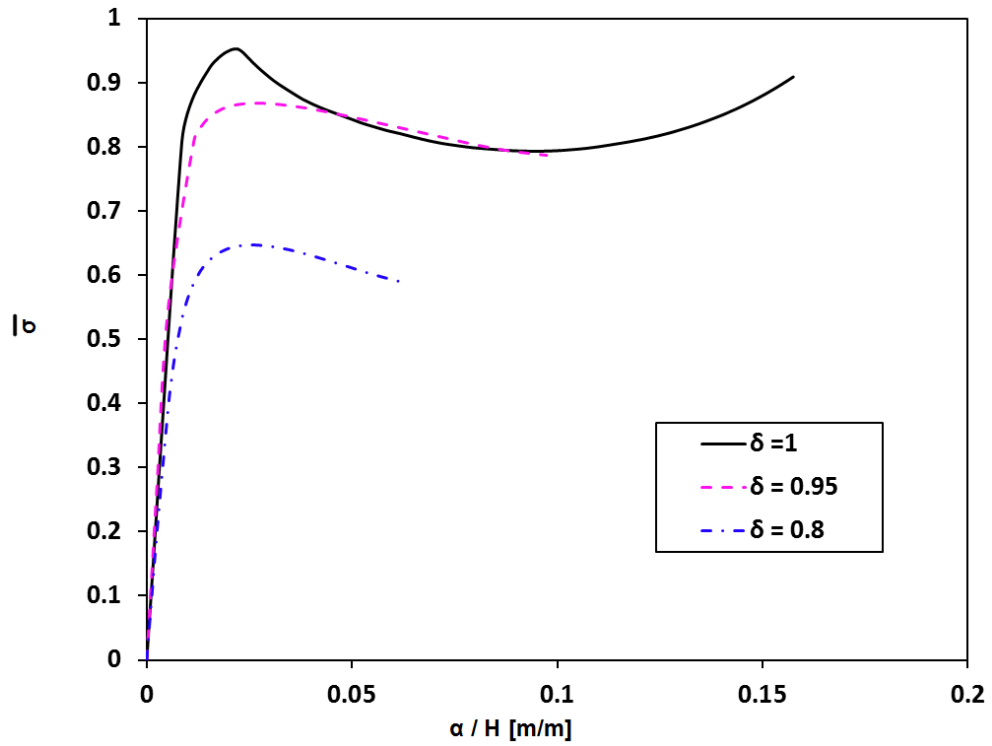


Figure 6.17: 3D Al Voronoi foams with a $\bar{\rho} = 9\%$ for different regularities.

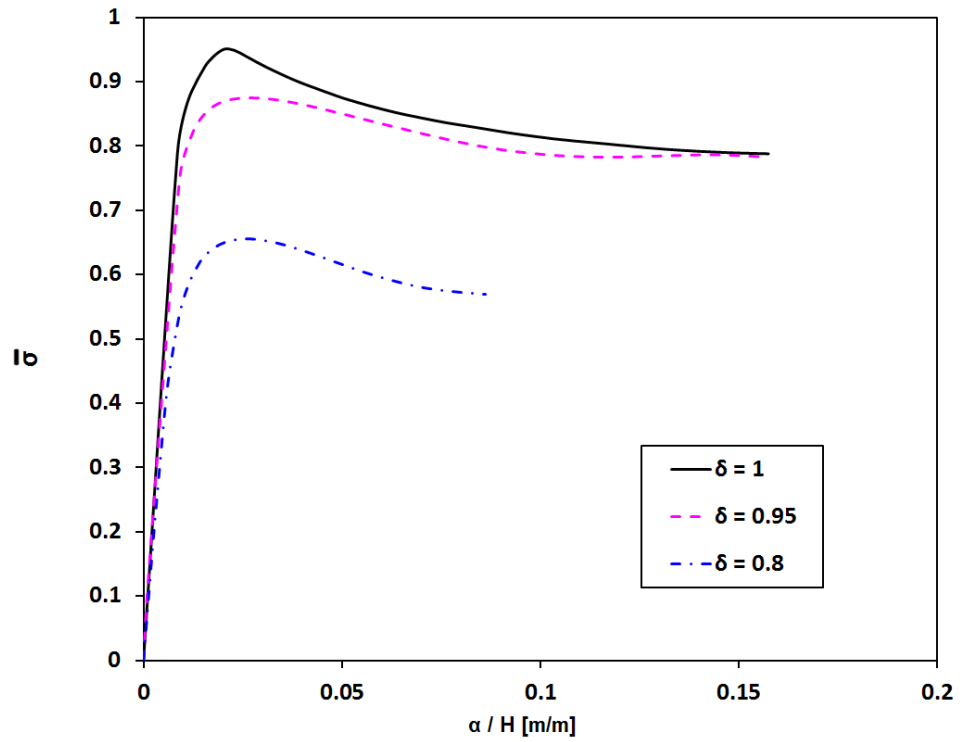


Figure 6.18: 3D Al Voronoi foams with a $\bar{\rho} = 7\%$ for different regularities.

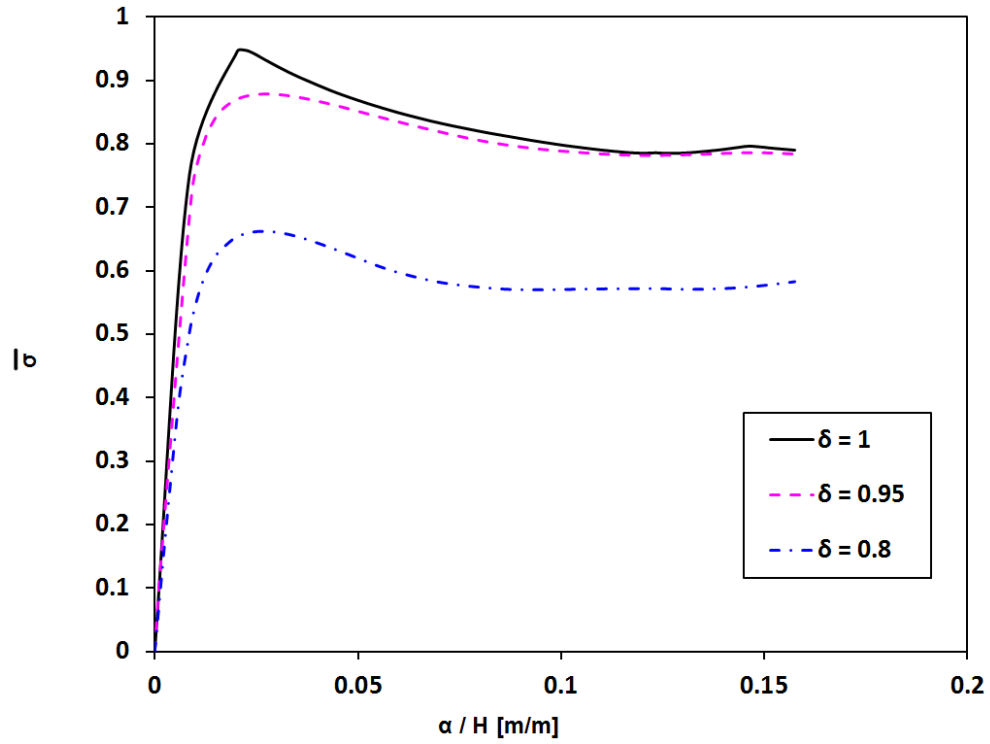


Figure 6.19: 3D Al Voronoi foams with a $\bar{\rho} = 5\%$ for different regularities.

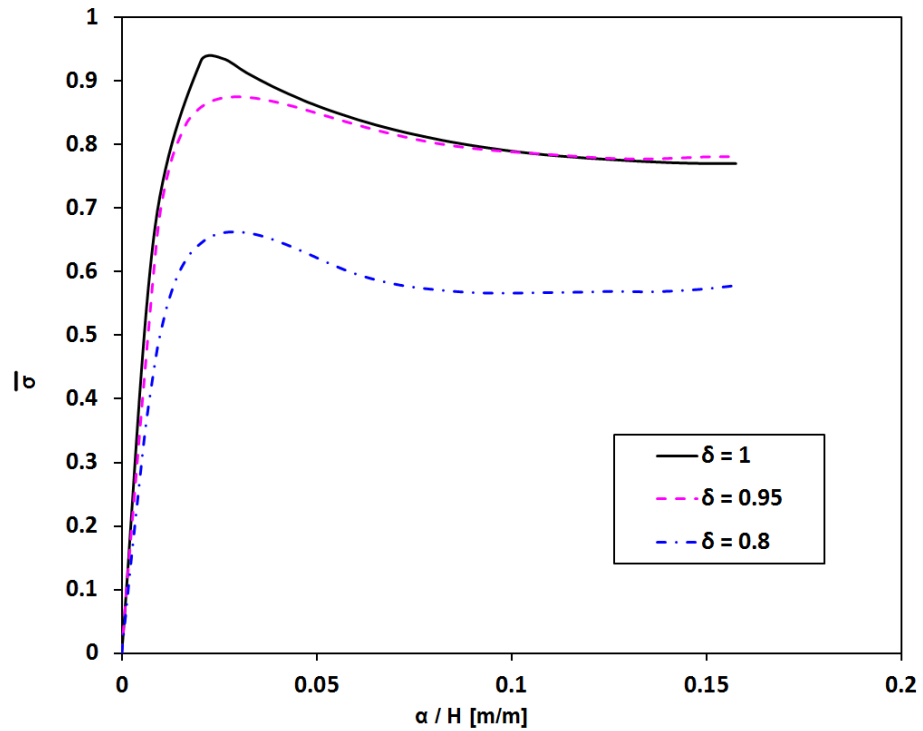


Figure 6.20: 3D Al Voronoi foams with a $\bar{\rho} = 3\%$ for different regularities.

CHAPTER 7

CONCLUSIONS AND FUTURE WORK

7.1. Conclusions

In this thesis, a procedure for creating virtual 2D and 3D foams has been presented. The geometries were generated by applying the Voronoi tessellation concept generalized to different Euclidean spaces. The process of generating dry and wet Voronoi structures through the stochastic generation of nuclei in a control space based on Poisson probability distribution in 2D and 3D actually capture the majority of characteristics observed in real foams except the effects of surface tension. A Simple Sequential Inhibition (SSI) process has been established in order to control the regularity of fully random foams. A suitable index for characterizing the regularity of specific foam structures quantitatively both in two and three dimensions has been identified. A regularity of '1' represents a completely regular foam whereas '0' corresponds to a fully irregular foam. The low probability of generating highly regular configurations has led to the development of a perturbation process to reach regularity parameters beyond 0.8. The described procedures in conjunction with solid modeling methods give designers tools for controlling the regularity, cross sectional shape of ligaments, relative density, number of cells and macroscopic shape of the Voronoi honeycombs (2D) and foams (3D). These characteristics are difficult to control in the current foam production methods employed. The possibility of creating real foams by exploiting Additive Manufacturing processes has also been demonstrated. A Voronoi honeycomb (2D) with $\bar{\rho} = 9\%$ and $\delta = 0.95$ has been created in a 3D printer that uses a Polyjet Technology. Additionally, a Voronoi foam (3D) has been created using Acrylonitrile-Butadiene-Styrene (ABS) based material in a 3D printer with a Fused Deposition Modeling (FDM) technique.

A modeling procedure for simulating compression response of Voronoi honeycombs has been developed. The stress-strain response shows an initial linear elastic behavior followed by a plateau region with a nearly constant stress response consistent with that of cellular solids. Additionally, an isotropic behavior was identified for all the configurations with only a limited directional dependency in case of regular honeycombs of higher densities. The linear elastic and plastic response of regular honeycombs which can be defined as a particular case of Voronoi honeycombs present good agreement with analytical formulae for elastic modulus and plastic-collapse strength. Due to the fact that these formulae have been extensively corroborated by experiments in the past, validity of results of this work for the rest of the regularity parameters was inferred. The influence of cell morphology, characterized by the regularity parameter, has also been studied in the full range from $\delta = 0$ to 1. It was found that an indirect relation exists between the cell regularity and elastic modulus, in agreement with the works of Silva et al., [15] and Zhu et al., [17]. However, in contrast to the former's conclusions, elastic modulus of fully irregular Voronoi honeycombs was found to be appreciably stiffer than their regular counterparts. This could be due to the fact that Silva and Gibson compared their results for geometries $\delta \approx 0.7$ and $\delta = 1$. While Silva and Gibson [15] found a difference of $\sim 6\%$ between the mentioned configurations, the present work shows a difference of $\sim 8\%$. However, a wider comparison between geometries of $\delta = 0$ and $\delta = 1$ suggests a difference of $\sim 66\%$. In contrast to the elastic behavior, the plastic-collapse strength on the other hand, shows a direct relationship with cell regularity. Hence, plastic-collapse strength of regular ($\delta = 1$) honeycombs is {28%, 31%, 35% and 50%} higher than a fully irregular ($\delta = 0$) honeycomb for relative densities of $\bar{\rho} = \{9\%, 7\%, 5\%, 3\%\}$, respectively. Additionally, it was found that the variation in the cell morphology has a small influence on the stress-strain response of Voronoi honeycombs when the regularity parameter is kept constant and geometries are generated in different trials.

Regarding the dependency on relative density, the data suggests that elastic modulus of Voronoi honeycombs scale with $\bar{\rho}^3$ while the plastic-collapse strength and plateau strength scale with $\bar{\rho}^2$.

Finite element models have also been developed to simulate the compression response of syntactic foam-filled Voronoi honeycombs as a two dimensional version of an Interpenetrating Phase Composite (IPC) foam. The directional and regularity dependence were analyzed by making use of wet Voronoi configurations with different regularity parameters, $\delta = \{0, 0.5, 0.7, 0.8 \text{ and } 1\}$. With the exception of regular configurations, the stress-strain curves present an isotropic response. Further, the regular configurations exhibited 44%, 22% and 11% higher elastic modulus, plastic-collapse strength and plateau strength, respectively, when compressed in the x_2 direction. Simulations suggest an inverse monotonic relation between all the mechanical properties considered in the present work and the regularity parameter for the geometries generated using the SSI process. A Voronoi foam-filled honeycomb with $\delta = 0$ was found $\sim 26\%$ stiffer than a $\delta = 0.8$ configuration while the plastic-collapse strength of $\delta = 0$ case was $\sim 10\%$ higher than that for $\delta = 0.8$. The elastic response of all the Voronoi foam-filled honeycombs generated using the SSI process was bounded between those for the regular configurations compressed in two orthogonal directions. On the other hand, the abrupt collapse observed in regular Voronoi foam filled-honeycombs made the plateau strength for $\delta = 0$, $\sim 22\%$ and $\sim 26\%$ higher than in the regular ($\delta = 1$) geometries compressed in the x_2 and x_1 directions, respectively.

The modeling procedure developed for Voronoi honeycombs has been extended to the 3D space to simulate open Voronoi foams. The elastic properties with different relative densities in the range of 3% to 9% have been compared with the corresponding analytical and empirical models available in the literature. The dependency of density of different Voronoi

foam configurations was shown to be bounded by the Gibson and Ashby [2] empirical model and Zhu et al., [64] analytical model although the latter under-predicted the FE results of this work. A favorable correlation between the results for the case of Voronoi foams of $\delta = 0.7$ and $\delta = 0.8$ with Warren et al., [67] model was also observed. Next, a more complex dependency of elastic modulus on the relative density than the one presented by Gibson and Ashby [2] was encountered for Voronoi foams. Nevertheless, the elastic modulus showed a variation describable by a second order polynomial suggesting bending as the primary mode of deformation. On the other hand, the numerical simulations showed that the plastic-collapse strength scaled with $\bar{\rho}^{1.5}$, in agreement with the theories for foams. Concerning the dependency on cell regularity, a comparable definition to the 2D case has been demonstrated for Voronoi foams. It was shown that the Voronoi diagram for a body centered arrangement of points produces regular tetrakaidecahedron foam. Additionally, a monotonic direct relationship between elastic modulus and plastic-collapse strength with regularity was identified in Voronoi foams. Thus, a tetrakaidecahedron foam representation was 41.3%, 43.7%, 46.5% and 49.5% stiffer than a fully irregular foam for $\bar{\rho} = \{9\%, 7\%, 5\% \text{ and } 3\%\}$, respectively. The increasing trend in the elastic modulus as the regularity parameter increases was also observed for the case of plastic-collapse strength. Surprisingly, plastic-collapse strength showed a relatively sharp rise in the regularity parameter range 0.8 to 1. A comparable response was also observed in the 2D geometries for the same regularity range. Finally, a desirable effect namely, avoiding an abrupt softening behavior by introducing a small perturbation ($\delta \approx 0.95$) has also been demonstrated.

7.2. Future work

To date, the effect of regularity on the compression response of Voronoi honeycombs and foams has been studied numerically and analytically but not experimentally. The primary reason might be that none of the current methods of foam production allows researchers the

possibility of controlling the regularity parameter in foams. However, with the method presented in chapter 3, real Voronoi honeycombs and Voronoi foams can be produced in order to experimentally correlate the results with the numerical counterparts presented in this work. Further, it should be interesting to study the response of a variety of functionally graded Voronoi honeycombs and Voronoi foams in the future. Hence, analyzing the variation of cell size, regularity of cells, cross sectional shape of ligaments and cross sectional dimensions from region to region should all be interesting as well.

In the present work, Voronoi foam was used as an idealization of real structural foams because it replicates majority of characteristics observed in real foams. However, once the restrictions inherent to foam production methods are resolved due to advances in the field of Advanced Manufacturing, others foam configurations can be studied. For instance, the Delaunay tessellation is complementary to Voronoi diagrams (see Fig. 2.11 for a 2D example). It would be interesting to examine the mechanical behavior of honeycombs and 3D foams based on Delaunay tessellation as this has not received equal attention as the Voronoi diagram in the context of structural foams since they do not replicate characteristics observed in real structures. For instance, in 3D, a Delaunay foam will be formed by tetrahedrons while in 2D it forms a network of triangles. Due to the fact that a 2D structure composed of triangles is a stretch-dominated structure as pointed out by Gibson et al., [68], it is predicted that Delaunay honeycombs and Delaunay foams will be stretch-dominated structures with superior structural efficiency.

REFERENCES

1. Yoseph B-C: **Biomimetics: biologically inspired technologies**: Taylor & Francis Group; 2006.
2. Gibson LJ, Ashby MF (eds.): **Cellular solids: structures & properties**, Second edn: Cambridge University Press; 1997.
3. Padma R, Simon HD: **Parallel processing for scientific computing**. In.: SIAM; 2006.
4. Naumann U, Schenk O (eds.): **Combinational scientific computing**: Chapman & Hall/CRC computational science; 2012.
5. Fleischer CA: **Mechanical and physical characterization of pumice/epoxy stochastic cellular solids**. University of Maryland; 2008.
6. Ashby MF, Evans A, Fleck NA, Gibson LJ, Hutchinson JW, Wadley HNG: **Metal Foams: A Design Guide**: Elsevier Science; 2000.
7. Shutov FA: **SYNTACTIC POLYMER FOAMS**. *Advances in Polymer Science* 1986:63-123.
8. Rahul J: **Compression Response and Modeling of Interpenetrating Phase Composites and Foam - Filled Honeycombs**. Auburn: Auburn University; 2009.
9. Clarke DR: **Interpenetrating Phase Composites**. *Journal of the American Ceramic Society* 1992, **75**(4):739-758.
10. Jhaver R, Tippur H: **Processing, compression response and finite element modeling of syntactic foam based interpenetrating phase composite (IPC)**. *Materials Science and Engineering: A* 2009, **499**(1-2):507-517.
11. San Marchi C, Kouzeli M, Rao R, Lewis JA, Dunand DC: **Alumina–aluminum interpenetrating-phase composites with three-dimensional periodic architecture**. *Scripta Materialia* 2003, **49**(9):861-866.
12. Papka SD, Kyriakides S: **Experiments and full-scale numerical simulations of in-plane crushing of a honeycomb**. *Acta Materialia* 1998, **46**(8):2765-2776.
13. Cricri G, Perrella M, Cali C: **Honeycomb failure processes under in-plane loading**. *Composites Part B: Engineering* 2013, **45**(1):1079-1090.
14. Silva MJ, Gibson LJ: **Effects of non-periodic microstructure and defects on the compressive strength of two-dimensional cellular solids**. *International Journal of Mechanical Sciences* 1997, **39**(5):549-563.
15. Silva MJ, Hayes WC, Gibson LJ: **The effects of non-periodic microstructure on the elastic properties of two-dimensional cellular solids**. *International Journal of Mechanical Sciences* 1995, **37**(11):1161-1177.
16. Tekoglu C, Gibson LJ, Pardoen T, Onck PR: **Size effects in foams: Experiments and modeling**. *Progress in Materials Science* 2011, **56**(2):109-138.
17. Zhu HX, Thorpe SM, Windle AH: **The effect of cell irregularity on the high strain compression of 2D Voronoi honeycombs**. *International Journal of Solids and Structures* 2006, **43**(5):1061-1078.
18. Borovinec M, Ren Z: **Computational modelling of irregular open-cell foam behaviour under impact loading**. *Materialwissenschaft und Werkstofftechnik* 2008, **39**(2):114-120.
19. Jhaver R, Tippur H: **Characterization and modeling of compression behavior of syntactic foam-filled honeycombs**. *Journal of Reinforced Plastics and Composites* 2010, **29**(21):3185-3196.
20. Jang W-Y, Kraynik AM, Kyriakides S: **On the microstructure of open-cell foams and its effect on elastic properties**. *International Journal of Solids and Structures* 2008, **45**(7-8):1845-1875.

21. Periasamy C, Tippur HV: **Experimental measurements and numerical modeling of dynamic compression response of an interpenetrating phase composite foam.** *Mechanics Research Communications* 2012, **43**:57-65.
22. Gong L, Kyriakides S, Triantafyllidis N: **On the stability of Kelvin cell foams under compressive loads.** *Journal of the Mechanics and Physics of Solids* 2005, **53**(4):771-794.
23. Raj SV: **Microstructural characterization of metal foams: An examination of the applicability of the theoretical models for modeling foams.** *Materials Science and Engineering A* 2011, **528**(15):5289-5295.
24. Dillard T, N'Guyen F, Maire E, Salvo L, Forest S, Bienvenu Y, Bartout JD, Croset M, Dendievel R, Cloetens P: **3D quantitative image analysis of open-cell nickel foams under tension and compression loading using X-ray microtomography.** *Philosophical Magazine* 2005, **85**(19):2147-2175.
25. Monnereau C, Prunet-Foch B, Vignes-Adler M: **Topology of slightly polydisperse real foams.** *Physical Review E - Statistical, Nonlinear, and Soft Matter Physics* 2001, **63**(6 D):061402/061401-061402/061410.
26. Montminy MD, Tannenbaum AR, Macosko CW: **The 3D structure of real polymer foams.** *Journal of Colloid and Interface Science* 2004, **280**(1):202-211.
27. Zhu HX, Hobdell JR, Windle AH: **Effects of cell irregularity on the elastic properties of open-cell foams.** *Acta Materialia* 2000, **48**(20):4893-4900.
28. Huang JS, Gibson LJ: **Creep of open-cell Voronoi foams.** *Materials Science and Engineering A* 2003, **339**(1-2):220-226.
29. [<http://www.rug.nl/natuurkunde/onderzoek/groepen/mimec/research/metallifoams?lang=en>]
30. Harders H, Hupfer K, Rosler J: **Influence of cell wall shape and density on the mechanical behaviour of 2D foam structures.** *Acta Materialia* 2005, **53**(5):1335-1345.
31. Liu YD, Yu JL, Zheng ZJ, Li JR: **A numerical study on the rate sensitivity of cellular metals.** *International Journal of Solids and Structures* 2009, **46**(22-23):3988-3998.
32. Strano M: **A new FEM approach for simulation of metal foam filled tubes.** *Journal of Manufacturing Science and Engineering, Transactions of the ASME* 2011, **133**(6).
33. Gonatas CP, Leigh JS, Yodh AG, Glazier JA, Prause B: **Magnetic Resonance Images of Coarsening Inside a Foam.** *Physical Review Letters* 1995, **75**(3):573-576.
34. Lipson H, Kurman M: **Fabricated: The New World of 3D Printing.** Indianapolis: John Wiley & Sons, Inc.; 2013.
35. Okabe A, Boots B, Sugihara K, Chiu SN (eds.): **Spatial tessellations: Concepts and Applications of Voronoi Diagrams**, Second edn: John Wiley & Sons Ltd.; 1945.
36. Rockafellar RT: **Convex Analysis**; 1996.
37. Martinez WL, Martinez AR: **Computational Statistics Handbook with MATLAB**: Chapman & Hall / CRC; 2002.
38. Guenter Wc: **Concepts of probability**: McGraw-Hill; 1968.
39. Klein R: **Concrete and Abstract Voronoi Diagrams**: Springer-Verlag; 1989.
40. Moller J: **Lectures on random Voronoi tessellations**: Springer-Verlag; 1994.
41. Tiyapan KN: **Voronoi Traslated**: Kittix Publishing; 2001.
42. Boots BN: **The arrangement of cells in "random" networks.** *Metallography* 1982, **15**(1):53-62.
43. [<http://innersoft.itspanish.org/en/>]
44. Weaire D, Hutzler S: **The physics of foams.** New York: Oxford University Press Inc. ; 1999.
45. Andrews EW, Gioux G, Onck P, Gibson LJ: **Size effects in ductile cellular solids. Part II: experimental results.** *International Journal of Mechanical Sciences* 2001, **43**(3):701-713.
46. Ripley BD: **Spatial Statistics.** New Jersey: John Wiley & Sons, INC.; 1981.
47. Diggle PJ (ed.): **Statistical analysis of spatial point patterns**, 2nd. edn. New York: Oxford University Press INC.; 2003.

48. Barber CB, Dobkin DP, Huhdanpaa HT: **The Quickhull Algorithm for Convex Hulls**. *ACM Transactions on Mathematical Software* 1996, **22**:469-483.
49. **The Quickhull algorithm** [<http://www.qhull.org/download/>]
50. Gibson LJ, Ashby MF: **Cellular solids; structure & properties**, second. edn: Cambridge University Press; 1997.
51. Gibson I, Ronsen DW, Stucker B: **Additive Manufacturing Technologies: Rapid Prototyping to Direct Digital Manufacturing**. New York: Springer; 2010.
52. Rekštytė S, Žukauskas A, Purlys V, Gordienko Y, Malinauskas M: **Direct laser writing of 3D polymer micro/nanostructures on metallic surfaces**. *Applied Surface Science* 2013, **270**(0):382-387.
53. Ajdari A, Canavan P, Nayeb-Hashemi H, Warner G: **Mechanical properties of functionally graded 2-D cellular structures: A finite element simulation**. *Materials Science and Engineering: A* 2009, **499**(1–2):434-439.
54. Mangipudi KR, Onck PR: **Multiscale modelling of damage and failure in two-dimensional metallic foams**. *Journal of the Mechanics and Physics of Solids* 2011, **59**(7):1437-1461.
55. Gan YX, Chen C, Shen YP: **Three-dimensional modeling of the mechanical property of linearly elastic open cell foams**. *International Journal of Solids and Structures* 2005, **42**(26):6628-6642.
56. Periasamy C, Jhaver R, Tippur HV: **Quasi-static and dynamic compression response of a lightweight interpenetrating phase composite foam**. *Materials Science and Engineering A* 2010, **527**(12):2845-2856.
57. **ABAQUS™ User's Manual (version 6.3)**; 2002.
58. Tekoglu C: **Size effects in cellular solids**. Groningen: University of Groningen; 2007.
59. Evans AG, Hutchinson JW, Ashby MF: **Cellular metals**. *Current Opinion in Solid State and Materials Science* 1998, **3**(3):288-303.
60. Said MR, Tan C-F: **Aluminium Honeycomb Under Quasi-Static Compressive Loading: An Experimental Investigation**. *Suranaree J Sci Technol* 2008, **16**(1):1-8.
61. Chen C, Lu TJ, Fleck NA: **Effect of imperfections on the yielding of two-dimensional foams**. *Journal of the Mechanics and Physics of Solids* 1999, **47**(11):2235-2272.
62. Guo XE, Gibson LJ: **Behavior of intact and damaged honeycombs: a finite element study**. *International Journal of Mechanical Sciences* 1999, **41**(1):85-105.
63. Warren WE, Neilsen MK, Kraynik AM: **Torsional rigidity of a plateau border**. *Mechanics Research Communications* 1997, **24**(6):667-672.
64. Zhu HX, Knott JF, Mills NJ: **Analysis of the elastic properties of open-cell foams with tetrakaidecahedral cells**. *Journal of the Mechanics and Physics of Solids* 1997, **45**(3):319-343.
65. Roberts AP, Garboczi EJ: **Elastic properties of model random three-dimensional open-cell solids**. *Journal of the Mechanics and Physics of Solids* 2002, **50**(1):33-55.
66. Shulmeister V, Van der Burg MWD, Van der Giessen E, Marissen R: **A numerical study of large deformations of low-density elastomeric open-cell foams**. *Mechanics of Materials* 1998, **30**(2):125-140.
67. Warren WE, Kraynik AM: **LINEAR ELASTIC PROPERTIES OF OPEN-CELL FOAMS**. *Journal of Applied Mechanics, Transactions ASME* 1988, **55**(2):341-346.
68. Gibson LJ, Ashby MF, Harley BA: **Cellular material in nature and medicine**. New York: Cambridge University Press; 2010.
69. Evans AG, Hutchinson JW, Fleck NA, Ashby MF, Wadley HNG: **Topological design of multifunctional cellular metals**. *Progress in Materials Science* 2001, **46**(3-4):309-327.
70. Deshpande VS, Fleck NA, Ashby MF: **Effective properties of the octet-truss lattice material**. *Journal of the Mechanics and Physics of Solids* 2001, **49**(8):1747-1769.

APPENDIX A
ALUMINUM DATA

Aluminum 6101-T6

Categories: [Metal](#); [Nonferrous Metal](#); [Aluminum Alloy](#); [6000 Series Aluminum Alloy](#)




Material Notes: Data points with the AA note have been provided by the Aluminum Association, Inc. and are NOT FOR DESIGN.


Composition Notes:

Composition information provided by the Aluminum Association and is not for design.

Key Words: UNS A96101; ISO E-ALMgSi; Aluminium 6101-T6; AA6101-T6

Vendors: No vendors are listed for this material. Please [click here](#) if you are a supplier and would like information on how to add your listing to this material.

Physical Properties	Metric	English	Comments
Density	2.70 g/cc	0.0975 lb/in ³	AA; Typical
Mechanical Properties			
	Metric	English	Comments
Hardness, Brinell	71	71	AA; Typical; 500 g load; 10 mm ball
Hardness, Knoop	94	94	Converted from Brinell Hardness Value
Hardness, Vickers	81	81	Converted from Brinell Hardness Value
Tensile Strength, Ultimate	221 MPa	32000 psi	AA; Typical
	17.0 MPa	2470 psi	
	@Temperature 371 °C	@Temperature 700 °F	
	24.0 MPa	3480 psi	
	@Temperature 316 °C	@Temperature 601 °F	
	33.0 MPa	4790 psi	
	@Temperature 260 °C	@Temperature 500 °F	
	69.0 MPa	10000 psi	
	@Temperature 204 °C	@Temperature 399 °F	
	145 MPa	21000 psi	
	@Temperature 149 °C	@Temperature 300 °F	
	193 MPa	28000 psi	
	@Temperature 100 °C	@Temperature 212 °F	
	221 MPa	32100 psi	
	@Temperature 24.0 °C	@Temperature 75.2 °F	
	234 MPa	33900 psi	
	@Temperature -28.0 °C	@Temperature -18.4 °F	
	248 MPa	36000 psi	
	@Temperature -80.0 °C	@Temperature -112 °F	
	296 MPa	42900 psi	
	@Temperature -196 °C	@Temperature -321 °F	
Tensile Strength, Yield	193 MPa	28000 psi	AA; Typical
	12.0 MPa	1740 psi	
	@Strain 0.200 %, Temperature 371 °C	@Strain 0.200 %, Temperature 700 °F	
	16.0 MPa	2320 psi	
	@Strain 0.200 %, Temperature 316 °C	@Strain 0.200 %, Temperature 601 °F	
	23.0 MPa	3340 psi	
	@Strain 0.200 %, Temperature 260 °C	@Strain 0.200 %, Temperature 500 °F	
	48.0 MPa	6960 psi	
	@Strain 0.200 %, Temperature 204 °C	@Strain 0.200 %, Temperature 399 °F	
	131 MPa	19000 psi	
	@Strain 0.200 %, Temperature 149 °C	@Strain 0.200 %, Temperature 300 °F	
	172 MPa	24900 psi	
	@Strain 0.200 %, Temperature 100 °C	@Strain 0.200 %, Temperature 212 °F	
	193 MPa	28000 psi	
	@Strain 0.200 %, Temperature 24.0 °C	@Strain 0.200 %, Temperature 75.2 °F	
	200 MPa	29000 psi	
	@Strain 0.200 %, Temperature -28.0 °C	@Strain 0.200 %, Temperature -18.4 °F	
	207 MPa	30000 psi	
	@Strain 0.200 %, Temperature -80.0 °C	@Strain 0.200 %, Temperature -112 °F	
	228 MPa	33100 psi	
	@Strain 0.200 %, Temperature -196 °C	@Strain 0.200 %, Temperature -321 °F	
Elongation at Break 	19.0 %	19.0 %	
	@Temperature -28.0 °C	@Temperature -18.4 °F	

	19.0 % @Temperature 24.0 °C	19.0 % @Temperature 75.2 °F	
	20.0 % @Temperature -80.0 °C	20.0 % @Temperature -112 °F	
	20.0 % @Temperature 100 °C	20.0 % @Temperature 212 °F	
	20.0 % @Temperature 149 °C	20.0 % @Temperature 300 °F	
	24.0 % @Temperature -196 °C	24.0 % @Temperature -321 °F	
	40.0 % @Temperature 204 °C	40.0 % @Temperature 399 °F	
	80.0 % @Temperature 260 °C	80.0 % @Temperature 500 °F	
	100 % @Temperature 316 °C	100 % @Temperature 601 °F	
	105 % @Temperature 371 °C	105 % @Temperature 700 °F	
	15.0 % @Thickness 1.59 mm	15.0 % @Thickness 0.0625 in	AA; Typical
Modulus of Elasticity	68.9 GPa	10000 ksi	AA; Typical; Average of tension and compression. Compression modulus is about 2% greater than tensile modulus.
Poissons Ratio	0.330	0.330	Estimated from trends in similar Al alloys.
Machinability	50 %	50 %	0-100 Scale of Aluminum Alloys
Shear Modulus	26.0 GPa	3770 ksi	Estimated from similar Al alloys.
Shear Strength	138 MPa	20000 psi	AA; Typical
Electrical Properties	Metric	English	Comments
Electrical Resistivity	0.00000299 ohm-cm @Temperature 20.0 °C	0.00000299 ohm-cm @Temperature 68.0 °F	AA; Typical
Thermal Properties	Metric	English	Comments
CTE, linear 	21.7 µm/m-°C @Temperature -50.0 - 20.0 °C	12.1 µin/in-°F @Temperature -58.0 - 68.0 °F	
	23.4 µm/m-°C @Temperature 20.0 - 100 °C	13.0 µin/in-°F @Temperature 68.0 - 212 °F	AA; Typical; average over range
	23.5 µm/m-°C @Temperature 20.0 - 100 °C	13.1 µin/in-°F @Temperature 68.0 - 212 °F	
	24.4 µm/m-°C @Temperature 20.0 - 200 °C	13.6 µin/in-°F @Temperature 68.0 - 392 °F	
	25.4 µm/m-°C @Temperature 20.0 - 300 °C	14.1 µin/in-°F @Temperature 68.0 - 572 °F	
	25.4 µm/m-°C @Temperature 20.0 - 300 °C	14.1 µin/in-°F @Temperature 68.0 - 572 °F	average
Specific Heat Capacity	0.895 J/g-°C	0.214 BTU/lb-°F	
Thermal Conductivity	218 W/m-K	1510 BTU-in/hr-ft ² -°F	AA; Typical at 77°F
Melting Point	621 - 654 °C	1150 - 1210 °F	AA; Typical range based on typical composition for wrought products 1/4 inch thickness or greater
Solidus	621 °C	1150 °F	AA; Typical
Liquidus	654 °C	1210 °F	AA; Typical
Processing Properties	Metric	English	Comments
Solution Temperature	510 °C	950 °F	hold at temperature for 1 hr
Aging Temperature	177 °C	350 °F	hold at temperature for 6 to 8 hr
Hot-Working Temperature	260 - 510 °C	500 - 950 °F	
Component Elements Properties	Metric	English	Comments
Aluminum, Al	<= 97.6 %	<= 97.6 %	As remainder
Boron, B	<= 0.060 %	<= 0.060 %	
Chromium, Cr	<= 0.030 %	<= 0.030 %	
Copper, Cu	<= 0.10 %	<= 0.10 %	
Iron, Fe	<= 0.50 %	<= 0.50 %	
Magnesium, Mg	0.35 - 0.80 %	0.35 - 0.80 %	
Manganese, Mn	<= 0.030 %	<= 0.030 %	
Other, each	<= 0.030 %	<= 0.030 %	
Other, total	<= 0.10 %	<= 0.10 %	
Silicon, Si	0.30 - 0.70 %	0.30 - 0.70 %	
Zinc, Zn	<= 0.10 %	<= 0.10 %	

[References](#) for this datasheet.

Some of the values displayed above may have been converted from their original units and/or rounded in order to display the information in a consistent format. Users requiring more precise data for scientific or engineering calculations can click on the property value to see the original value as well as raw conversions to equivalent units. We advise that you only use the original value or one of its raw conversions in your calculations to minimize rounding error. We also ask that you refer to MatWeb's [terms of use](#) regarding this information. [Click here](#) to view all the property values for this datasheet as they were originally entered into MatWeb.

APPENDIX B

MATLAB CODES

1. Code used to create a simple sequential inhibition process in 3D, from [37] but extended to the 3D space. (for the 2D version refer to [37])

```
%%generate the simple inhibition process for a 3D
delta = 0.1;
% Get the vertices for the regions.
rx=[0; 1; 1; 0; 0; 1; 1; 0; 0];
ry=[0; 0; 1; 1; 0; 0; 1; 1; 0];
rz=[0; 0; 0; 0; 1; 1; 1; 1; 0];
n = 500;
D = zeros(n,3);
% Generate the first event.
D(1,:) = csbinproc3d(rx,ry,rz,1);
i = 1;
% Generate the other events.
while i<n
    [sx,sy,sz] = csbinproc3d(rx, ry, rz, 1);
    xt = [sx sy sz ; D(1:i,:)];
    % Find the distance between the events
    dist = pdist(xt);
    % Find the distance between the candidate event
    % and the others that have been generated already.
    ind = find(dist(1:i) <= delta);
    if isempty(ind)
        % Then we keep the event.
        i = i+1;
        D(i,:) = [sx, sy, sz];
    end
end
xx=D(:,1);
yy=D(:,2);
zz=D(:,3);
scatter3(xx,yy,zz, '.');
%%-----
function [x,y,z] = csbinproc3d(xp, yp, zp, n)
    x = zeros(n,1);
    y = zeros(n,1);
    z = zeros(n,1);
    i = 1;
    minx = min(xp);
    maxx = max(xp);
    miny = min(yp);
    maxy = max(yp);
    minz = min(zp);
```

```

maxz = max(zp);
cx = maxx-minx;
cy = maxy - miny;
cz = maxz - minz;
while i <= n
    xt = rand(1)*cx + minx;
    yt = rand(1)*cy + miny;
    zt = rand(1)*cz + minz;
    k = inhull([xt,yt,zt],[xp,yp,zp]);
    if k == 1
        x(i) = xt;
        y(i) = yt;
        z(i) = zt;
        i = i+1;
    end
end
end
%%-----
function in = inhull(testpts,xyz,tess,tol)
p = size(xyz,2);
[n,c] = size(testpts);
if p ~= c
    error 'testpts and xyz must have the same number of columns'
end
if p < 2
    error 'Points must lie in at least a 2-d space.'
end

if (nargin<3) || isempty(tess)
    tess = convhulln(xyz);
end
[nt,c] = size(tess);
if c ~= p
    error 'tess array is incompatible with a dimension p space'
end

if (nargin<4) || isempty(tol)
    tol = 0;
end

switch p
case 2
    nrmls = (xyz(tess(:,1),:) - xyz(tess(:,2),:)) * [0 1;-1 0];

    del = sqrt(sum(nrmls.^2,2));
    degenflag = (del<(max(del)*10*eps));
    if sum(degenflag)>0
        warning('inhull:degeneracy',[num2str(sum(degenflag)), ...
            ' degenerate edges identified in the convex hull'])

        nrmls(degenflag,:) = [];
        nt = size(nrmls,1);
    end
case 3
    ab = xyz(tess(:,1),:) - xyz(tess(:,2),:);
    ac = xyz(tess(:,1),:) - xyz(tess(:,3),:);

```

```

        nrmls = cross(ab,ac,2);
        degenflag = repmat(false,nt,1);
    otherwise
        nrmls = zeros(nt,p);
        degenflag = repmat(false,nt,1);
        for i = 1:nt
            nullsp = null(xyz(tess(i,2:end),:) -
repmat(xyz(tess(i,1),:),p-1,1))';
            if size(nullsp,1)>1
                degenflag(i) = true;
                nrmls(i,:) = NaN;
            else
                nrmls(i,:) = nullsp;
            end
        end
        if sum(degenflag)>0
            warning('inhull:degeneracy',[num2str(sum(degenflag)), ...
                ' degenerate simplexes identified in the convex hull'])

            nrmls(degenflag,:) = [];
            nt = size(nrmls,1);
        end
    end

nrmlen = sqrt(sum(nrmls.^2,2));
nrmls = nrmls.*repmat(1./nrmlen,1,p);

center = mean(xyz,1);

a = xyz(tess(~degenflag,1),:);

dp = sum((repmat(center,nt,1) - a).*nrmls,2);
k = dp<0;
nrmls(k,:) = -nrmls(k,:);

aN = sum(nrmls.*a,2);

in = repmat(false,n,1);

memblock = 1e6;
blocks = max(1,floor(n/(memblock/nt)));
aNr = repmat(aN,1,length(1:blocks:n));
for i = 1:blocks
    j = i:blocks:n;
    if size(aNr,2) ~= length(j),
        aNr = repmat(aN,1,length(j));
    end
    in(j) = all((nrmls*testpts(j,:))' - aNr) >= -tol,1)';
end

```

2. Code used to create the Voronoi diagram and output for one cell.

```
% Create D.
[c,v] = voronoin(D);
% Create a matrix with the information of each cell
for i =1:length(v);
    nx{i}=c(v{i},:);
end
%%-----

xlswrite('optimusdata.xls',nx{1},'sheet1','A1')
```

3. Code used to generate a regular arrangement of points inside a cube.

```
function [D] = kelvinpermute(l,r)

%kelvin permute
%let us calculate the locations of nuclei points inside a cube
%where, l is the number of cells along one length of the cube
%r is the distance among kelvin cells
%%-----

A=(0:r:l*r);
B=(r/2:r:l*r);
X=npermutek(A,3);
Y=npermutek(B,3);
D=[X;Y];
xx=D(:,1);
yy=D(:,2);
zz=D(:,3);
scatter3(xx,yy,zz, '.')
end

%%-----
% npermutek available at mathworks.com
```

4. Code used to generate a perturbation of points in a 3D regular arrangement.

```
function [DD] = perturbatekelvin(l,r,h)
%generate a matrix of regular arrangement of points perturbed
% a h magnitude.

A=(0:r:l*r);
B=(r/2:r:l*r);
n=(l+1)^3+l^3;
X=npermutek(A,3);
Y=npermutek(B,3);
D=[X;Y];
for i=1:n
```

```

        P(i)=h*(2*rand-1);
    end
    xx=D(:,1);
    xxx=xx+P';
    for i=1:n
        PP(i)=h*(2*rand-1);
    end
    yy=D(:,2);
    yyy=yy+PP';
    for i=1:n
        PPP(i)=h*(2*rand-1);
    end
    zz=D(:,3);
    zzz=zz+PPP';
    DD=[xxx,yyy,zzz];
    scatter3(xxx,yyy,zzz,'.');
end

```

APPENDIX C

DERIVATION OF FORMULAS

1. Derivation of the formula for calculating the Elastic Modulus of a hexagonal honeycomb following Gibson and Ashby approach [2], but for circular cross sections. (The graphs and notation are from Gibson and Ashby book [2] and differ from the notation used in this thesis. Notation is only change when the formula is transfer from the Appendix to the body of the thesis in the final step)

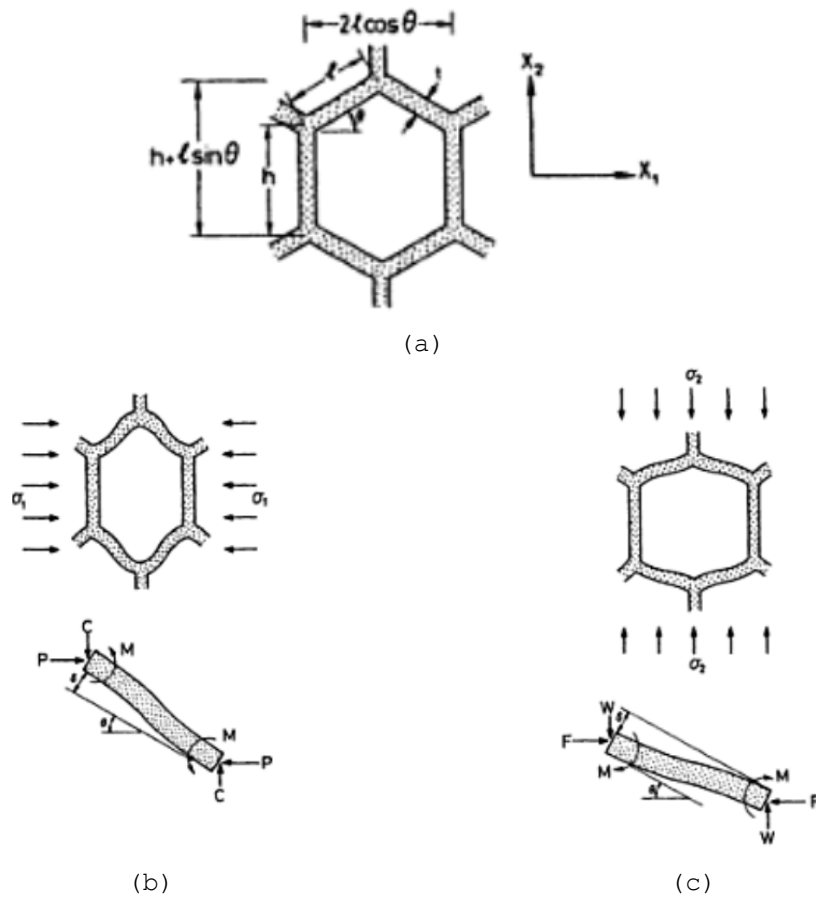


Figure C1: Cell deformation by cell wall bending: (a) the undeformed honeycomb, (b) and (c) the bending caused by loads in the x_1 and x_2 directions. From [2]

Notation presented in the figure

M	Moment tending to bend the cell
l	Length of the ligament
b	Depth
E_s	Young's Modulus of the solid material
r	Radius of the cross section
d	Diameter of the cross section
P	Force

The Moment M tending to bend the cell is

$$M = \frac{P * l * \sin \theta}{2}$$

Where

$$P = \sigma_1(h + l * \sin \theta)b$$

From standard beam theory the wall deflects by:

$$\delta = \frac{P * l^3 * \sin \theta}{12 E_s * I}$$

Where I is the second moment of inertia for the cell wall

$$I = 1/4(\pi * r^4)$$

Giving a strain in the x_1 direction equal to

$$\epsilon_1 = \frac{\sigma_1(h + l * \sin \theta)b * l^2 * \sin^2 \theta}{12 E_s * I * \cos \theta}$$

If

$$b = 2r$$

and

$$E_1^* = \sigma_1 / \epsilon_1$$

The Young's modulus parallel to x_1 is

$$\frac{E_1^*}{E_s} = \frac{3\pi \left(\frac{r}{l}\right)^3 \cos \theta}{\left(\frac{h}{l} + \sin \theta\right) \sin^2 \theta}$$

For a regular hexagon $h = l$ $\theta = 30^\circ$

With $d = 2r$

$$\frac{E_1^*}{E_s} = \frac{\sqrt{3}\pi \left(\frac{d}{l}\right)^3}{4}$$

2. Derivation of the formula for calculating the Plastic-collapse strength of a hexagonal honeycomb following Gibson and Ashby approach [2], but for circular cross sections. (The graphs and notation are from Gibson and Ashby book [2] and differ from the notation used in this thesis. Notation is only change when the formula is transfer from the Appendix to the body of the thesis in the final step)

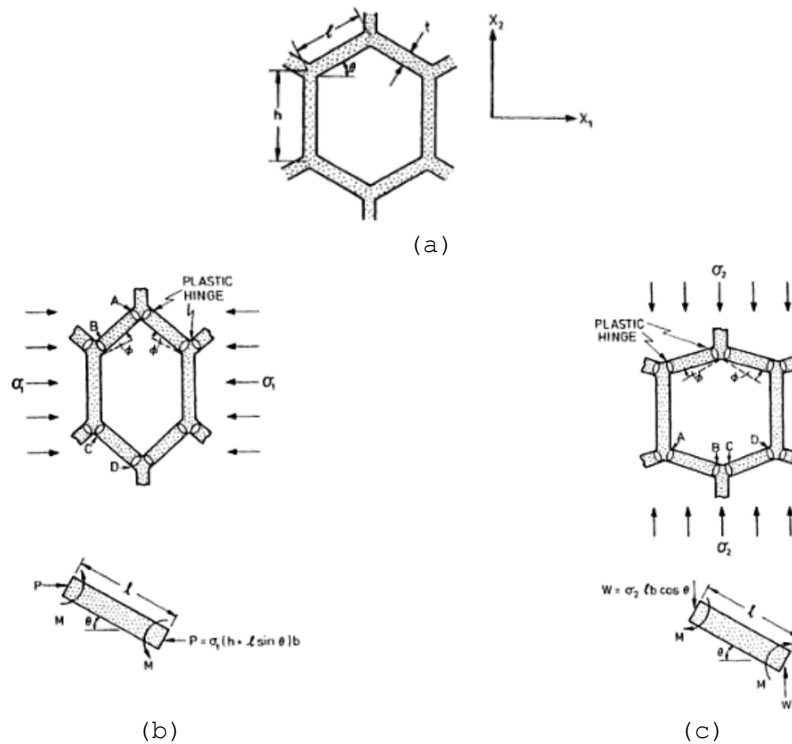


Figure C2: Cell deformation by plastic collapse: (a) the undeformed honeycomb, (b) and (c) the rotations, moments and forces for loading in the x_1 and x_2 directions. From [2]

Notation presented in the figure

M	Moment
l	Length of the ligament
b	Depth
σ_{ys}	Yield stress of the cell-wall material
r	Radius of the cross section
d	Diameter of the cross section
P	Force

Equating the work done by the force

$$P = \sigma_1(h + l \sin \theta)b$$

During a plastic rotation ϕ of the four plastic hinges A, B, C, and D to the plastic work done at the hinges giving:

$$4 M_p \phi \geq 2\sigma_1 b(h + l \sin \theta)\phi l \sin \theta$$

Where M_p is the fully plastic moment of the cell wall in bending:

$$M_p = \frac{4}{3} \sigma_{ys} r^3$$

If $b=2r$

It follows that

$$\frac{\sigma_1}{\sigma_{ys}} = \frac{4}{3} \left(\frac{r}{l}\right)^2 \frac{1}{\left(\frac{h}{l} + \sin \theta\right) \sin \theta}$$

For a regular hexagon $h = l$ and $\theta = 30^\circ$

With $d = 2r$

$$\frac{\sigma_{p1}^*}{\sigma_{ys}} = \frac{4}{9} \left(\frac{d}{l}\right)^2$$